Technische Universität München

Max-Planck-Institut für Physik

(Werner-Heisenberg-Institut)

Techniques to distinguish between electron and photon induced events using segmented germanium detectors

Kevin Kröninger

Vollständiger Abdruck der von der Fakultät für Physik der Technischen Universität München zur Erlangung des akademischen Grades eines Doktors der Naturwissenschaften (Dr. rer. nat.) genehmigten Dissertation.

Vorsitzender: Univ.-Prof. Michael Ratz

Prüfer der Dissertation:

1. Hon.-Prof. Allen C. Caldwell, Ph.D
2. Univ.-Prof. Lothar Oberauer

Die Dissertation wurde am 26.04.2007 bei der Technischen Universität München eingereicht und durch die Fakultät für Physik am 05.06.2007 angenommen.

Abstract

Two techniques to distinguish between electron and photon induced events in germanium detectors were studied: (1) anti-coincidence requirements between the segments of segmented germanium detectors and (2) the analysis of the time structure of the detector response.

An 18-fold segmented germanium prototype detector for the GERDA neutrinoless double beta-decay experiment was characterized. The rejection of photon induced events was measured for the strongest lines in ^{60}Co, ^{152}Eu and ^{228}Th. An accompanying Monte Carlo simulation was performed and the results were compared to data. An overall agreement with deviations of the order of 5-10% was obtained. The expected background index of the GERDA experiment was estimated.

The sensitivity of the GERDA experiment was determined. Special statistical tools were developed to correctly treat the small number of events expected.

The GERDA experiment uses a cryogenic liquid as the operational medium for the germanium detectors. It was shown that germanium detectors can be reliably operated through several cooling cycles.

Zusammenfassung

Es wurden zwei Techniken zur Unterscheidung von Elektron- und Photon-induzierten Ereignissen in Germanium-Detektoren untersucht: (1) Anti-Koinzidenzen zwischen den Segmenten segmentierter Germanium-Detektoren und (2) die Analyse der Zeitstruktur der Detektor-Antwortfunktion.

Ein 18-fach segmentierter Prototyp-Detektor für das GERDA Experiment zu neutrinolosem Doppelbeta-Zerfall wurde untersucht und charakterisiert. Insbesondere wurde die Unterdrückung Photon-induzierter Ereignisse für die stärksten Linien von ^{60}Co, ^{152}Eu und ^{228}Th gemessen. Die Ergebnisse wurden mit den Resultaten einer begleitenden Monte Carlo Studie verglichen. Die Simulationen beschreiben die Daten mit Abweichungen von etwa 5-10%. Der erwartete Untergrund des GERDA Experiments wurde abgeschätzt.

Spezielle statistische Verfahren, welche die kleine Anzahl von erwarteten Ereignissen berücksichtigen, wurden entwickelt um die Sensitivität des Experiments auf neutrinolosen Doppelbeta-Zerfall abzuschätzen.

Das GERDA Experiment wird Germanium Detektoren direkt in einer Kryoflüssigkeit betreiben. Es konnte gezeigt werden, dass Detektoren ohne eine Beeinträchtigung der Leistung über mehrere Kalt-Warm-Zyklen betrieben werden können.

Contents

Chapter 1

Introduction

Since its postulation by Pauli in 1931 the neutrino was assumed to be a very light (massless in the Standard Model) and chargeless Dirac particle. Early on it was recognized that the neutrino could also be a Majorana particle, i.e., its own anti-particle. The observation of neutrino oscillations, rewarded with the Nobel Prize in 2002, gave evidence for finite masses of the neutrinos. Because only mass differences can be inferred from these observations, the absolute neutrino mass scale is still unknown. The question whether the neutrino is a Dirac or Majorana particle is also still open.

Nowadays, three classes of experiments aim to measure the neutrino mass scale. The exact determination of the end point energy of the spectrum of tritium beta-decays can be used to calculate the mass of the electron neutrino; structure formation in the universe can be used to set limits on the sum of the neutrino masses; finally, the observation of neutrinoless double beta-decay could give information about a possible mass of the neutrino. The latter would also prove that the neutrino is a Majorana particle. So far, all three approaches could only set upper limits on the neutrino mass of the order of 1-2 eV.

Searches for neutrinoless double beta-decay reach back to the 1950ies. The most stringent limits come from experiments built to search for neutrinoless double beta-decay of the germanium isotope ^{76}Ge. Germanium is a semiconductor and can therefore be used as source and detector simultaneously. The sensitivity of previous experiments was limited not only by the exposure but also by background which was dominated by external γ-radiation [1, 2].

The GERmanium Detector Array, GERDA [3], is a new experiment which is built to search for neutrinoless double beta-decay of ^{76}Ge. It is currently being installed in the Hall A of the INFN Gran Sasso National Laboratory (LNGS), Italy. The background index aimed at is two orders of magnitude below that of recent experiments. With 100 kg·years exposure this will result in a sensitivity to the effective Majorana neutrino mass of about 200 meV. The background reduction is accomplished by a reduced amount of background producing material close to the detectors, a large passive shielding and, for the second phase of the experiment, the usage of segmented germanium detectors.

The main goal of this thesis is to evaluate the potential of segmented germanium detectors to distinguish electron induced events from events induced by multiply scattered photons. The second goal is to study the operation of germanium detectors submerged in a cryogenic liquid.

Four aspects are investigated in particular with respect to the distinction between electrons and photons:

1. An estimate of the sensitivity of GERDA to neutrinoless double beta-decay for different background scenarios. Special statistical analysis tools were developed for the treatment of the small number of expected events.

2. The evaluation of the potential of segmented germanium detectors to distinguish electron induced events from events induced by multiply scattered photons using segment coincidences. The impact on the background reduction in the GERDA experiment was estimated using Monte Carlo techniques.

3. The characterization of a segmented prototype detector. A test stand for a segmented prototype detector for the second phase of the GERDA experiment was built. Data were taken with this detector and analyzed with respect to the distinction between electrons and photons using segment coincidences. The results were compared to the predictions from a Monte Carlo simulation.

4. The evaluation of the potential of segmented germanium detectors to distinguish electron induced events from events induced by multiply scattered photons analyzing the time structure of the detector response. Data were taken with the prototype detector and the detector response was analyzed. Three different analysis methods were developed and the results compared.

The studies are performed in the context of the second phase of the GERDA experiment. Chapter 2 summarizes today's picture of neutrinos in the Standard Model and the double beta-decay processes. The concept and the technical realization of the GERDA experiment are described in Chapter 3. A spectral analysis technique developed to estimate the sensitivity of the experiment is introduced in Chapter 4. The operation principle and the development of the electrical signals of germanium detectors is discussed in Chapter 5. The main background sources for GERDA are summarized in Chapter 6 where the signatures of the signal and background processes are discussed. Monte Carlo simulations of the introduced processes are presented in Section 7.1.

Photons in the MeV-energy region typically scatter multiple times inside germanium and deposit their energy over a range of several centimeters. In contrast, electrons in the same energy region deposit their energy on a millimeter scale. Electrons and photons can thus be distinguished by determining the spatial distribution over which energy is deposited. This can be done by using segmented detectors (Chapter 7), or by analyzing the time structure of the detector response (Chapter 8).

The experimental setup of the prototype detector and the data sets are described in the second part of Chapter 9 and in Chapter 10. The simulation of the test stand is also described Chapter 9. The data taken with the prototype detector were compared to Monte Carlo data in order to verify the Monte Carlo simulation. The results are presented in Chapter 11.

A second, unsegmented germanium detector was operated while being submerged in liquid nitrogen or argon. The setup and the results are described in Chapter 9. It is shown that this mode of operation is feasible.

In Chapter 12 the developed background reduction techniques are applied to Monte Carlo data in order to estimate the background index of the GERDA experiment. Conclusions and a summary are given in the last chapter.

Chapter 2

Neutrinoless double beta-decay in the framework of the Standard Model

2.1 Electro-weak interaction and neutrinos

The neutrino was postulated by Pauli in 1931 as a very light and chargeless particle which would restore energy conservation in nuclear beta-decay. Fermi's description of the interaction of neutrinos, the weak interaction, was developed in the 1930ies and could explain many phenomena observed in nature. These range from the spectra in the mentioned nuclear beta-decay to the decay kinematics of muon and tau leptons. Although part of a successful theory it was not before 1953 that (anti-)neutrinos were first observed by Cowen and Reines in a reactor experiment [4].

Since then, many observations and modifications of the existing theory have led to a unified description of electro-magnetism and the weak interaction. The *Standard Model of Particle Physics* (SM) is based on the *electro-weak* and *strong* forces. It was developed by Glashow, Salam and Weinberg [5–7] and so far gives a valid description of the interactions of its constituents, including neutrinos. A variety of measurements, partially motivated by theoretical predictions, confirm the validity of the model. The measurements include the observation of parity violation by Wu in 1957 [8] and the first direct observation of massive intermediate gauge bosons at CERN in 1983 [9, 10].

2.1.1 From weak to electro-weak interaction

Fermi's ansatz for the description of neutrino interactions was inspired by quantum electrodynamics (QED) assuming a point-like vector-vector Lorentz-invariant amplitude. Although successful in many respects, Fermi's model of the weak interaction is an effective, low-energy theory. The theory violates unitarity at high energies and fails to explain the experimental observation of parity violation. Two major modifications of the theory

solved these problems: the introduction of intermediate vector bosons by Yukawa (1938) and Schwinger (1957), and the assumption of a V–A current. In this framework only the left-handed component of the neutrino field participates in the weak interaction. Parity is maximally violated.

A unification of electro-magnetism and the weak interaction was necessary in order to accommodate these two modifications and explain the experimental data. The electro-weak interaction reflects a $SU(2)_L \times U(1)_Y$ symmetry, where the subscript L refers to the *weak isospin* current which only couples to left-handed fermions. The subscript Y refers to the *weak hypercharge* current which couples to left- and right-handed fermions. Three massive gauge bosons, the charged $W^{\pm}$ and the neutral Z^0, and one massless photon, γ, mediate the force. The former two only couple to the left-handed components of the lepton fields, whereas the Z^0 and the photon couple to left- and right-handed fields. The observable $W^{\pm}$ bosons are combinations of the two charged fields from the $SU(2)_L$ symmetry, whereas the Z^0 and the photon are mixtures of the two neutral fields emerging from the $SU(2)_L$ and $U(1)_Y$ symmetries. The latter mixing is described by the Weinberg angle.

2.1.2 Leptons and the Standard Model

Three types, or flavors, of charged leptons are known: electron (e), muon (μ) and tau (τ). The number of flavors is not predicted by the Standard Model. From the measurement of the width of the Z^0 boson at the SLC and LEP colliders [11] it was inferred that only three types of light neutrinos exist. Each charged lepton is assigned a neutrino partner. The pair is referred to as a generation and interpreted as a left-handed doublet (under a $SU(2)$ transformation), $\left(\nu_L^l,\, l_L\right)$, with $l = e,\, \mu,\, \tau$. A right-handed singlet l_R of the charged lepton accompanies the doublet. Leptons from different generations couple with the same strength, but differ in mass. Although not required by the Standard Model, the lepton number, L, is found to be conserved family-wise[1], i.e., the number of leptons of a certain flavor, L_l, is the same in the initial and final state of an interaction ($\Delta L_l = 0$). No evidence for total lepton number violation has been found so far (see review article in [12]).

2.2 Neutrino oscillations

The picture of neutrinos was revised after the observation of neutrino oscillations. If neutrinos are massive particles and their flavor (or weak interaction) eigenstates do not coincide with their mass eigenstates, neutrinos can change their flavor. The first evidence that the physics of neutrinos deviates from SM assumptions came from the measurement of the solar neutrino flux and was known as the *solar neutrino problem* [13]. Later, the *atmospheric neutrino anomaly*, a measured deficit of muon neutrinos from the atmosphere, could also not be explained in the context of the SM.

[1] Not taking into account the neutrino oscillations discussed later.

In the following a mathematical description of neutrino oscillations is introduced. An overview of the solar neutrino problem and its interpretation are presented as an example for the compelling experimental evidence for neutrino oscillations. A summary of recent experimental results is given at the end of this section. A detailed overview of neutrino mixing is given in e.g., [14].

2.2.1 Neutrino oscillation parameterization

If neutrinos are massive and the neutrino flavor eigenstates, ν_α ($\alpha = e,\ \mu,\ \tau,\ \ldots$ [2]), do not coincide with the neutrino mass eigenstates, ν_j (j=1, 2, 3, ...), neutrinos of a specific flavor α can be described as a combination of mass eigenstates:

$$|\nu_\alpha\rangle = \sum_j U^*_{\alpha j} |\nu_j\rangle \ , \tag{2.1}$$

where U is a unitary matrix referred to as the Pontecorvo-Maki-Nakagawa-Sakata (PMNS) matrix.

Using Schrödinger's equation the time evolution of the neutrino can be calculated. A neutrino produced with the flavor α which has traveled a distance L can be described as

$$|\nu_\alpha(L)\rangle \approx \sum_j U^*_{\alpha j} e^{-i(m_j^2/2E)L} |\nu_j\rangle \ , \tag{2.2}$$

where m_j is the mass of the jth mass eigenstate and E is the average energy of all mass eigenstates. Inverting Equation (2.1) and re-inserting it into Equation (2.2) results in

$$|\nu_\alpha(L)\rangle \approx \sum_\beta \left[\sum_j U^*_{\alpha j} e^{-i(m_j^2/2E)L} U_{\beta j} \right] |\nu_\beta\rangle \ . \tag{2.3}$$

The probability to find the neutrino in a flavor state $|\nu_\beta\rangle$ after it traveled a distance L is $|\langle\nu_\beta|\nu_\alpha(L)\rangle|^2$. The observation of such a transition implies that the lepton number is not conserved family-wise. The probability for a change of neutrino flavor can easily be calculated for the case of two neutrino flavors. Solar neutrino oscillations are given as an example later.

Two neutrino case: Assuming only two flavors (ν_α, ν_β) and two mass eigenstates (ν_1, ν_2), the unitary matrix U in Equation (2.1) is a two-dimensional rotation matrix

$$U = \begin{bmatrix} \cos\theta & \sin\theta \\ -\sin\theta & \cos\theta \end{bmatrix} \ , \tag{2.4}$$

[2] Allowing for more than three flavors, e.g., for sterile or very heavy neutrinos.

where θ is the (one) mixing angle. For $\theta = 0°$ the flavor eigenstates do not mix, i.e., flavor and mass eigenstates are identical. For finite θ the probability for the neutrino to change flavor, $p(\nu_\alpha \to \nu_\beta)$, is

$$\begin{aligned} p(\nu_\alpha \to \nu_\beta) &= \sin^2 2\theta \sin^2 \left(\Delta m^2_{12} \frac{L}{4E} \right) \\ &= \sin^2 2\theta \sin^2 \left(1.27 \Delta m^2_{12}[\mathrm{eV}^2] \frac{L\ [\mathrm{km}]}{E\ [\mathrm{GeV}]} \right) , \end{aligned} \tag{2.5}$$

with $\Delta m^2_{12} = m^2_1 - m^2_2$. The first line is in natural, the second line is in real units. The probability to change flavor depends on the mass squared difference of the mass eigenstates, the average neutrino energy and the distance the neutrino travels. The neutrino flavor changes periodically with the distance L, hence the name neutrino oscillations. Note that for neutrino oscillations to be possible, the mixing angle θ has to be different from zero and at least one of the two mass terms has to be greater than zero.

Three neutrino case: Assuming three neutrino flavors (ν_e, ν_μ, ν_τ) the unitary matrix U becomes a 3×3 matrix. A common parameterization is

$$U = \begin{bmatrix} 1 & 0 & 0 \\ 0 & c_{23} & s_{23} \\ 0 & -s_{23} & c_{23} \end{bmatrix} \times \begin{bmatrix} c_{13} & 0 & s_{13}e^{-i\delta} \\ 0 & 1 & 0 \\ -s_{13}e^{i\delta} & 0 & c_{13} \end{bmatrix} \times \begin{bmatrix} c_{12} & s_{12} & 0 \\ -s_{12} & c_{12} & 0 \\ 0 & 0 & 1 \end{bmatrix} \times \begin{bmatrix} e^{i\alpha_1/2} & 0 & 0 \\ 0 & e^{i\alpha_2/2} & 0 \\ 0 & 0 & 1 \end{bmatrix} , \tag{2.6}$$

where $s_{ij} = \sin\theta_{ij}$ and $c_{ij} = \cos\theta_{ij}$ represent the sines and cosines of the three mixing angles. δ, α_1 and α_2 are CP-violating phases. The latter two are only of importance if the neutrino is its own anti-particle (see next section). In total there are six (eight) free parameters to describe neutrino oscillations: three mixing angles, two mass differences (the third one is constrained) and one (three) CP-phase(s). The observed neutrino oscillations can be described as two flavor oscillations (see Section 2.2.3) in most cases.

The calculations presented previously are applicable for oscillations in the absence of matter and referred to as vacuum oscillations. The probability for changing flavor is altered in matter due to scattering processes via $W^\pm$- (only ν_e) and Z^0-exchange (all ν's) [15, 16]. This is referred to as the Mikheyev-Smirnov-Wolfenstein (MSW) effect. It accounts e.g., for the large reduction in the solar neutrino flux.

2.2.2 Solar neutrinos

The sun produces large fluxes of electron neutrinos in a chain of processes. The energy dependent flux of neutrinos produced in the participating reactions are shown in Figure 2.1 as predicted by the *Standard Solar Model* (SSM) [17]. The proton-proton fusion (*pp* chain), $p + p \to D + e^+ + \nu_e$, produces the largest flux of neutrinos with energies of up to about 0.42 MeV. The ^{7}Be-process, $^7\mathrm{Be} + e^- \to {}^7\mathrm{Li} + \nu_e$, produces mono-energetic neutrinos of 0.86 MeV. Neutrinos with energies of up to 14.06 MeV are emitted in the decay of ^{8}B, $^8\mathrm{B} \to {}^8\mathrm{Be} + e^+ + \nu_e$.

In 1968, Ray Davis Jr. and collaborators were the first to measure the solar neutrino flux at the Homestake gold mine [18]. A tank filled with 100 000 gallons of C_2Cl_4 served as a detector. Solar neutrinos were captured by the reaction $^{37}\mathrm{Cl}+\nu_e \rightarrow {}^{37}\mathrm{Ar}+e^-$. The threshold for this process is a neutrino energy of 0.81 MeV. Approximately 78% of the captured neutrinos originate from the ^{8}B-process, about 15% from the ^{7}Be-process. The radioactive ^{37}Ar was extracted and the number of ^{37}Ar atoms counted using a low-background detector setup. The measured capture rate was $(2.56 \pm 0.16 \pm 0.16)$ SNU[3] [19]. This rate corresponds to about one-third of the rate predicted by the SSM of (8.1 ± 1.3) SNU [17].

Other radiochemical experiments later confirmed the results from the Homestake experiment. The GALLEX [20], GNO [21] (both Gran Sasso, Italy) and SAGE [22] (Baksan, Russia) experiments used gallium to capture solar neutrinos in the reaction $^{71}\mathrm{Ga} + \nu_e \rightarrow {}^{71}\mathrm{Ge} + e^-$ which has a large cross-section for the capture of *pp*-neutrinos. The threshold for this process is a neutrino energy of 0.23 MeV. The radioactive ^{71}Ge atoms were extracted and counted. The measured flux was less than that predicted by the SSM [23–25].

In the beginning of the 1980ies, the Kamiokande experiment, originally built to search for proton-decay based on a large water Cherenkov detector, was also used as neutrino observatory [26]. Neutrinos traversing the water volume scatter off electrons elastically. The electrons produce Cherenkov light. This light was measured using photomultiplier tubes yielding not only the energy but also an approximation of the angle of the incident neutrino. With the directional information first direct evidence was given that neutrinos emerge from the sun [27]. Due to the threshold of several MeV the experiment was only sensitive to ^{8}B-neutrinos. The measured flux of $(2.80 \pm 0.19 \pm 0.33)$ SNU [28] was again less than the predicted SSM flux. The successor of Kamiokande, the Super-Kamiokande experiment, yielded compatible results with a precision improved by more than one order of magnitude [29].

The Sudbury Neutrino Observatory, SNO, used heavy water (D_2O) as target medium. Only electron neutrinos from the ^{8}B-process interact via the charged-current (CC) reaction $\nu_e + D \rightarrow p + p + e^-$ while all neutrino flavors interact via the neutral-current (NC) reactions $\nu_x + D \rightarrow \nu_x + p + n$ and elastic neutrino-electron scattering (ES) $\nu_x + e^- \rightarrow \nu_x + e^-$. The NC reaction has the same cross-section for all three neutrino flavors while the ES reaction has a smaller cross-section for muon and tau neutrinos compared to electron neutrinos. The flux measured in NC reactions is consistent with the SSM prediction [30, 31]. The charged current and ES measurements indicate a low ν_e flux. All three measurements are only consistent with each other if, in addition to the ν_e flux, a finite $\nu_{\mu+\tau}$ flux is assumed.

[3] The Solar Neutrino Unit, SNU, is defined as 10^{-36} captures/(atom·s). The first and second errors are statistical and systematic error, respectively.

Modifications of the SSM cannot explain all experimental results. Today's interpretation is that electron neutrinos are converted into muon and tau neutrinos via oscillations. With the combined measurement of the electron and the total solar neutrino flux the hypothesis of neutrino oscillations was, for the first time, proved.

The disappearance of electron (anti-)neutrinos was also observed by the KamLAND experiment, a kilo-ton liquid scintillator experiment. Electron anti-neutrinos from surrounding power plants (with an average distance of 180 km) interact with protons via the CC reaction $\overline{\nu_e} + p \rightarrow e^+ + n$. The observed number of neutrinos is consistent with the solar neutrino experiments and the oscillation hypothesis [32].

A global analysis of the solar neutrino data and the KamLAND results, assuming a two-neutrino oscillation, was presented in [31]. The difference of the mass squared of the two neutrino flavors is labeled $\Delta m^2_\odot$, the mixing angle is $\theta_\odot$. Figure 2.2 shows the allowed region in the $\Delta m^2_\odot$-$\tan^2\theta_\odot$-space. The best fit results in $\Delta m^2_\odot = (8.0^{+0.6}_{-0.4}) \cdot 10^{-5}$ eV^2 and $\tan^2\theta_\odot = 0.45^{+0.09}_{-0.07}$. A three-neutrino oscillation analysis yields consistent results (see next section).

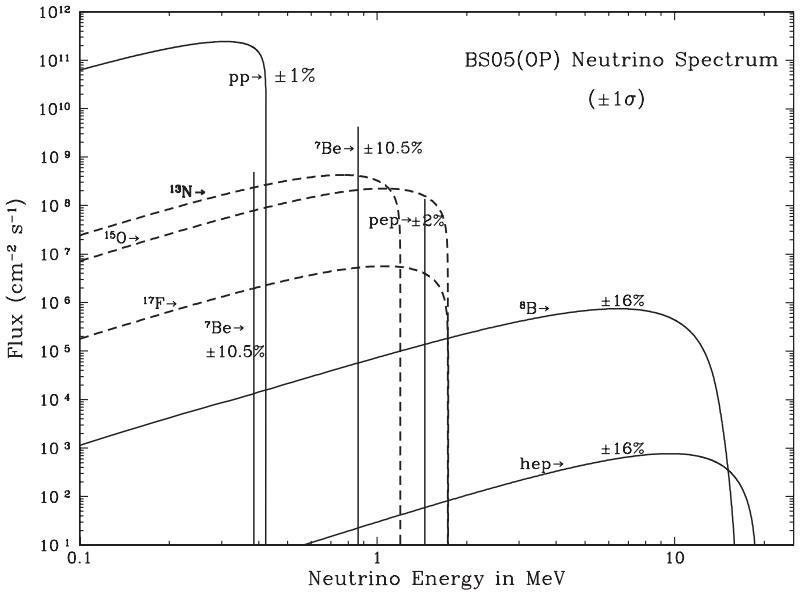

Figure 2.1: Energy dependent flux of solar neutrinos predicted by the solar model BS05(OP) [17].

2.2.3 Summary of experimental results

Evidence for neutrino oscillations has been established by experiments with solar, atmospheric, reactor and accelerator neutrinos. From the four (six) free parameters in the PMNS matrix (Equation (2.6)) all three angles have either been measured or constrained. The CP-violating phase δ and the two Majorana phases α_1 and α_2 are not within exper-

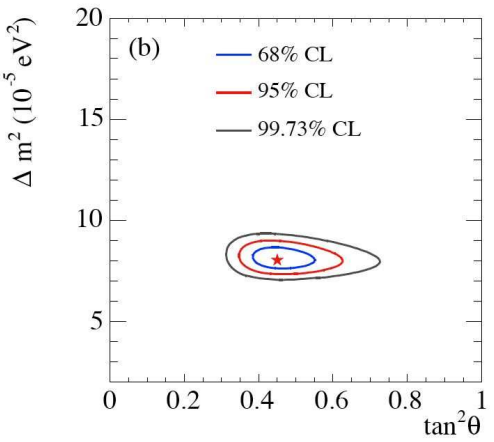

Figure 2.2: Global solar two-neutrino oscillation analysis using solar neutrino and KamLAND data. The star corresponds to the best fit parameters [31].

imental reach yet. Table 2.1 summarizes the neutrino oscillation parameters obtained by a three-flavor analysis of the experimental data.

Table 2.1: Summary of the neutrino oscillation parameters obtained by a three-flavor analysis of the experimental data. All values are taken from the references in [12]. The angles $\theta_\odot$ and θ_{atm} are the solar and atmospheric mixing angles in the corresponding two-flavor analysis.

Parameter	Measured value
$\sin^2 2\theta_{12} \approx \sin^2 2\theta_\odot$	$0.86^{+0.03}_{-0.04}$ [31]
$\sin^2 2\theta_{23} \approx \sin^2 2\theta_{\text{atm}}$	> 0.92 (90% C.L.) [33]
$\sin^2 2\theta_{13}$	< 0.19 (90% C.L.) [34]
Δm^2_{21}	$(8.0^{+0.4}_{-0.3}) \cdot 10^{-5}$ eV^2 [31]
$\lvert\Delta m^2_{32}\rvert$	$(1.9 - 3.0) \cdot 10^{-3}$ eV^2 [35]
	best fit: $2.4 \cdot 10^{-3}$ eV^2
δ, α_{12}, α_2	-

The value of θ_{13} is bound to $\sin^2 2\theta_{13} \lesssim 0.19$ (90% C.L.) from reactor experiments. This implies that the mass eigenstate ν_3 has a very small component of the flavor eigenstate ν_e. As no oscillations $\nu_\mu \to \nu_e$ have been observed, the atmospheric oscillations are interpreted as two-neutrino oscillations $\nu_\mu \to \nu_\tau$. Hence, the angle θ_{23} approximately corresponds to the atmospheric angle θ_{atm}, i.e., $\theta_{23} \approx \theta_{\text{atm}}$. Similarly, the solar neutrino oscillations are interpreted as two-neutrino oscillations with $\theta_{12} \approx \theta_\odot$. The sign of the mass difference Δm^2_{32} is not known whereas the sign of Δm^2_{21} is known. The latter is determined in the framework of the MSW effect.

As the CP-violating phase δ never appears as an isolated term but always in conjunction with all mixing angles, a small angle θ_{13} also implies that any CP-violation effect is small, independent of the value of δ.

It is possible to decompose the mass eigenstates into flavor eigenstates by inverting Equation (2.1). As the sign of Δm^2_{32} cannot be measured in oscillation experiments, it is unknown which of the two pairs, the solar or the atmospheric, is the heavier one. Two possible *hierarchies* are distinguished: the *normal* hierarchy with $\Delta m^2_{32} > 0$ and the *inverted* hierarchy with $\Delta m^2_{32} < 0$. Both are depicted in Figure 2.3. If the mass of the lightest neutrino is much larger than the mass differences, the hierarchy is referred to as *quasi-degenerate*.

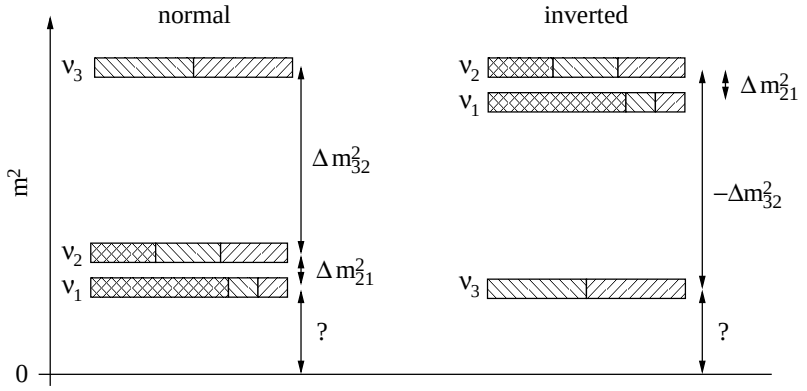

Figure 2.3: Normal and inverted hierarchy. The cross-, right- and left-hatched areas give the contributions of the electron, muon and tau neutrino flavor eigenstates to the neutrino mass eigenstates.

2.3 Neutrino mass terms and measurements

The observation of neutrino oscillations implies that neutrinos are massive particles. The SM was extended accordingly. As neutrino oscillations only depend on mass differences the absolute scale of neutrino masses cannot be inferred from oscillation experiments. Only a lower limit of $m \gtrsim 40$ meV on the heaviest neutrino mass can be set from the maximal mass difference. Other direct and indirect measurements were so far only able to set upper limits of about 1–2 eV on the neutrino mass scale.

2.3.1 Neutrino mass terms

Within the framework of the SM neutrinos were originally assumed to be massless. In order to accommodate finite neutrino masses additional mass terms were added to the SM Lagrangian. Until then, the SM only described interactions of left-handed neutrino fields, denoted ν_L; right-handed components, ν_R, did not participate in the SM interactions. For

massive leptons left- and right-handed fields exist. The mass term couples left- and right-handed fields. Right-handed neutrino fields are thus included in order to accommodate such a Lagrangian for neutrinos:

$$\mathcal{L}_{\mathrm{D}} = -m_{\mathrm{D}}\overline{\nu_L}\nu_R + h.c.\ , \tag{2.7}$$

where m_{D} is the mass of the neutrino. The subscript D refers to the *Dirac*-nature of the neutrino. Similar to charged leptons, the Lagrangian $\mathcal{L}_{\mathrm{D}}$ conserves the lepton number for neutrinos. A neutrino, ν, and its anti-particle, $\overline{\nu}$, are two distinct particles. In this case neutrinos are referred to as *Dirac* neutrinos.

As the neutrino does not carry electrical charge or color, it could be its own anti-particle, i.e., $\nu = \overline{\nu}$. The lepton number would not be conserved. In this case neutrinos are referred to as *Majorana* neutrinos. In addition to $\mathcal{L}_{\mathrm{D}}$, a second mass term becomes possible, connecting the neutrino and its charge conjugate

$$\mathcal{L}_{\mathrm{M}} = -m_{\mathrm{M}}\overline{\nu_{\mathrm{R}}^{c}}\nu_{\mathrm{R}} + h.c.\ , \tag{2.8}$$

where m_{M} is referred to as the Majorana mass. Lepton number conservation is not required by the SM and hence a mass term such as $\mathcal{L}_{\mathrm{M}}$ can be accommodated in the framework.

The see-saw mechanism [36, 37] is a theoretical approach to explain the smallness of the neutrino masses compared to the masses of charged leptons and quarks. It includes both Dirac and Majorana mass terms, implying that the neutrino is its own anti-particle. Neutrinoless double beta-decay is so far the only experimental probe of the nature of the neutrino. It will be discussed in Section 2.4.

2.3.2 Neutrino mass measurements

Neutrino masses are experimentally determined both directly and indirectly.

An indirect determination of the absolute neutrino mass scale comes from cosmology. The most model independent limit comes from the closure density of the universe. The best limit comes from the density of large scale structures. As neutrinos have small masses, structures on small scales are washed out. Depending on the data sets used and the models assumed, the limits are of the order of $\sum_{i=1}^{3} m_i < \mathcal{O}(1)$ eV. For an overview see e.g., [38].

Decays of unstable particles or nuclei where one of the daughter particles is a neutrino allow direct mass measurements. The mass of the neutrino is estimated from the kinematics of the visible daughter particles. If the neutrino is a Majorana particle, the rate of neutrinoless double beta-decay, discussed in Section 2.4, can also be used to obtain information about the neutrino mass. It should be mentioned that the measured mass parameter is not the same in different experiments due to the mismatch of mass and flavor eigenstates.

Measurements of the effective electron, muon and tau neutrino masses: The effective neutrino mass for a flavor α is the weighted average of the masses of the mass eigenstates:

$$\langle m_{\nu_\alpha} \rangle = \sqrt{\sum_i |U_{\alpha i}|^2 \, m_i^2} \; , \tag{2.9}$$

where the sum runs over all mass eigenstates and $U_{\alpha i}$ are the matrix elements of the PMNS matrix. Note that cancellations due to CP-phases cannot occur, as only the absolute value of the terms $U_{\alpha i}$ occur. Note also that the Dirac or Majorana nature of the neutrino cannot be inferred from these mass parameters.

The effective electron neutrino mass can be deduced from beta-decay experiments in which the shape of the electron energy spectrum around the endpoint energy is measured. In this region, the shape of the spectrum depends on the mass of the electron neutrino. The most prominent example is the measurement of the endpoint energy in tritium-decays as performed by the recent Mainz [39] and Troitsk [40] experiments. Today's best limit is $\langle m_{\nu_e} \rangle < 2.3$ eV (95% C.L.) [41]. Future experiments, such as the KATRIN experiment in Karlsruhe, will probe the effective electron neutrino mass down to a level of about 200 meV [42].

A limit on the effective muon neutrino mass can be set from the decays of positively charged pions at rest via $\pi^+ \to \mu^+ \nu_\mu$. Knowing the masses of the pion, m_π, and the muon, m_μ, and measuring the muon momentum, p_μ, the muon neutrino mass can be written as

$$\left\langle m_{\nu_\mu} \right\rangle^2 = m_\pi^2 + m_\mu^2 - 2 m_\pi \sqrt{p_\mu^2 + m_\mu^2} \; . \tag{2.10}$$

The current best limit is $\left\langle m_{\nu_\mu} \right\rangle < 170$ keV (90% C.L.) [43]. New experiments like NuMass aim at a sensitivity of about 8 keV in the effective muon neutrino mass [44].

Similarly, the measurement of the final state of tau-decays in e^+e^--colliders is used to set limits on the effective tau neutrino mass. The current best limit is $\langle m_{\nu_\tau} \rangle < 18.2$ MeV (95% C.L.) [45].

2.4 Double beta-decay

Double beta-decay is a rare, second order weak process. A nucleus of charge Z and atomic number A decays into a nucleus of charge $Z \pm 2$ while leaving A unchanged. The sign depends on the type of beta-decay. In the following, β^--decay is assumed. This nuclear transition has two modes, the *neutrino accompanied double beta-decay* ($2\nu\beta\beta$) and the *neutrinoless double beta-decay* ($0\nu\beta\beta$). Both are depicted in Figure 2.4 (left) and can be written as

$$2\nu\beta\beta: \quad (Z, A) \;\; \to \;\; (Z+2, A) + 2e^- + 2\overline{\nu_e} \; , \tag{2.11}$$

$$0\nu\beta\beta: \quad (Z, A) \;\; \to \;\; (Z+2, A) + 2e^- \; . \tag{2.12}$$

The $2\nu\beta\beta$-decay process was first discussed in 1935 [46]. Two electrons and two electron anti-neutrinos are emitted during the nuclear transition. The total kinetic energy, the Q-value of the decay, is shared between the four leptons (neglecting the recoil energy of the daughter nucleus). The spectrum of the sum of the kinetic energies of both electrons is continuous and ranges up to the Q-value with a maximum at around $Q/3$. It is depicted in Figure 2.4 (right) where the energy is normalized to the Q-value. The $2\nu\beta\beta$-decay process conserves the total lepton number as the number of leptons in the initial and final state is the same (and equal to zero). It has been observed in several nuclei.

In the $0\nu\beta\beta$-decay process, first discussed in 1937 [47, 48], only two electrons are emitted; the two neutrinos annihilate. The neutrino has to be its own anti-particle, i.e., of a Majorana nature, to make this possible. The total kinetic energy in the $0\nu\beta\beta$-decay process is therefore shared between the two emitted electrons only (again neglecting the recoil energy of the daughter nucleus). Figure 2.4 (right) shows that the sum spectrum of the kinetic energies of the electrons is a sharp peak at the Q-value. The $0\nu\beta\beta$-decay process does not conserve the total lepton number as the number of leptons in the initial state is zero and the electron lepton number in the final state is +2. It should be noted that $0\nu\beta\beta$-decay could not only be mediated by Majorana neutrinos but also by other (non-SM) particles (see, e.g., [49, 50]). However, it can be shown that if $0\nu\beta\beta$-decay is observed the neutrino is of Majorana nature [51].

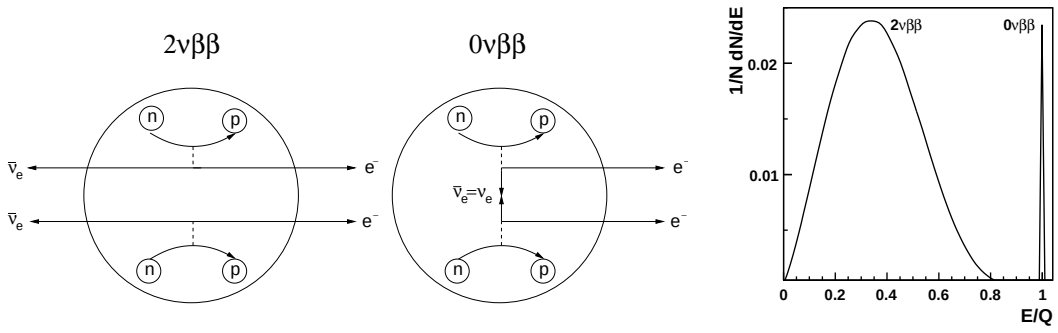

Figure 2.4: Left: The two channels of double beta-decay. In the $2\nu\beta\beta$-decay process two electrons and two electron anti-neutrinos are emitted. Lepton number is therefore conserved. In the $0\nu\beta\beta$-decay process only two electrons are emitted while the (Majorana) neutrinos annihilate. Lepton number is violated. Right: Sum spectra of the electron kinetic energies for $2\nu\beta\beta$- and $0\nu\beta\beta$-decay as described in the text. The former is continuous up to the Q-value while the latter is a sharp peak at the Q-value.

Double beta-decay is only observable for nuclei for which the daughter product of a single beta-decay is heavier than the initial nucleus. Single beta-transitions are thus forbidden. This is only possible in even-even nuclei due to the strong binding energy. Otherwise, any competitive (single) beta-decay will make it nearly impossible to observe

double beta-decay. About 35 nuclei are known which fulfill this requirement. As an example, Figure 2.5 shows the isobars for $A = 76$ [52]. The mass of ^{76}Ge is less than that of ^{76}As and larger than that of ^{76}Se. Double beta-decay is thus possible for the germanium isotope ^{76}Ge.

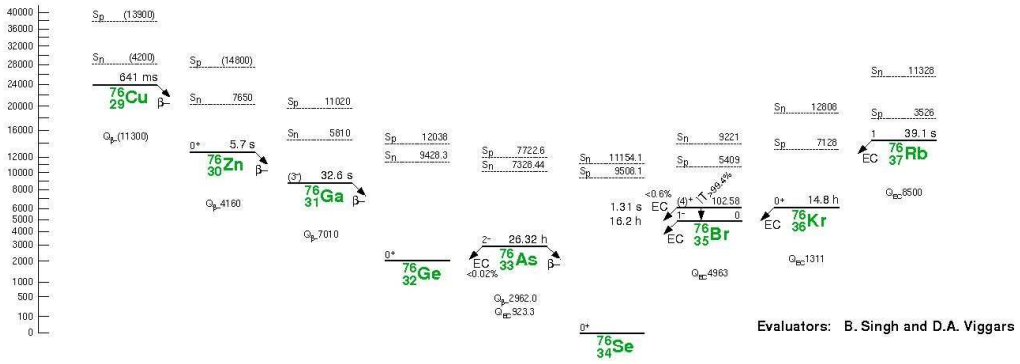

Figure 2.5: Isobars for $A = 76$ [52]. The mass of ^{76}Ge is less than that of ^{76}As, but larger than that of ^{76}Se.

The decay rate of any double beta-decay process can be calculated using Fermi's golden rule:

$$1/T_{1/2}^{2\nu\beta\beta} = \Gamma_{2\nu\beta\beta} = G_{2\nu}(Q, Z) \cdot |\mathcal{M}_{2\nu}|^2 \ , \tag{2.13}$$

$$1/T_{1/2}^{0\nu\beta\beta} = \Gamma_{0\nu\beta\beta} = G_{0\nu}(Q, Z) \cdot |\mathcal{M}_{0\nu}|^2 \cdot \langle m_\nu \rangle^2 \ , \tag{2.14}$$

where the phase space factors $G_{2\nu}(Q, Z)$ and $G_{0\nu}(Q, Z)$ depend on the Q-value and the nuclear charge Z. The rates of the $2\nu\beta\beta$- and $0\nu\beta\beta$-processes scale with Q^{11} and Q^5, respectively. $\mathcal{M}_{2\nu}$ and $\mathcal{M}_{0\nu}$ denote the nuclear matrix elements which describe the hadronic part of the decay. The factor $\langle m_\nu \rangle$ is referred to as the effective Majorana neutrino mass. The neutrinos are created in the electron flavor eigenstate. They can be decomposed into mass eigenstates using the PMNS matrix. The effective Majorana neutrino mass is therefore the coherent sum over the neutrino mass eigenstates,

$$\langle m_\nu \rangle = \left| \sum_i m_i U_{ei}^2 \right| = \left| m_1 \cdot |U_{e1}|^2 + m_2 \cdot |U_{e2}|^2 \cdot e^{i(\alpha_2 - \alpha_1)} + m_3 \cdot |U_{e3}|^2 \cdot e^{i(-\alpha_1 - 2\cdot\delta)} \right| \ . \tag{2.15}$$

Note that cancellations of terms might occur due to the CP-violating phases. Note also that this effective mass does not correspond to the effective mass observed in tritium experiments in which cancellations cannot occur.

In summary: the neutrino has to be a Majorana particle with a finite mass in order to make $0\nu\beta\beta$-decay possible.

2.4.1 Extraction of mass parameters

The observable quantity in double beta-decay experiments is the half-life, $T_{1/2}^{0\nu\beta\beta}$, of the process. It is connected with the effective Majorana neutrino mass via Equation (2.14). In order to relate the half-life of the $0\nu\beta\beta$-process to the effective Majorana neutrino mass, the two additional terms on the right hand side of the equation have to be known. The phase space factor $G_{0\nu}(Q, Z)$ is calculable to sufficient precision while the calculation of the nuclear matrix element $\mathcal{M}_{0\nu}$ shows rather large uncertainties.

In case of an observation of $0\nu\beta\beta$-decay the effective Majorana neutrino mass can be related to the lightest neutrino mass, depending on the neutrino mass hierarchy. Figure 2.6 shows the effective Majorana neutrino mass as a function of the lightest neutrino mass. The two outer bands represent the best fit and 3 σ-uncertainties of the oscillation parameters used for the two possible hierarchies. The light band represents the inverted and the dark band the normal hierarchy [53, 54]. As noted previously, cancellations due to CP-violating phases can result in small effective masses for the normal hierarchy.

Nuclear matrix elements The nuclear matrix elements in Equations (2.13) and (2.14) are calculable in at least two different approaches: the Nuclear Shell Model (see e.g., [55, 56]) and the Quasi Random Phase Approximation (QRPA) (see e.g., [57, 58]). The calculations of the $\mathcal{M}_{0\nu}$ elements are calibrated using the measured $2\nu\beta\beta$-rates. In the QRPA approach nuclear model parameters, in particular the particle-particle strength parameter, g_{pp}, can be fixed with this additional information. Calculations are available for several isotopes. For a single isotope the spread between different calculations is of the order of 30%. The $\mathcal{M}_{0\nu}$ matrix elements calculated in the QRPA approach are listed in Table 2.2 in the next section.

2.4.2 Experimental considerations

As $0\nu\beta\beta$-decay is predicted to be an extremely rare process, it is limited in sensitivity by signal statistics and by the amount of observed background. The following considerations enter into the design of a double beta-decay experiment:

- A good energy resolution to distinguish $2\nu\beta\beta$-decays from $0\nu\beta\beta$-decays kinematically.
- The rate of $0\nu\beta\beta$-decay scales with Q^5. An isotope with a high Q-value is therefore expected to have a shorter half-life (Note that the rate of $2\nu\beta\beta$-decay scales with Q^{11}). Most double beta-decay experiments use isotopes with a Q-value larger than 2 MeV.
- The amount of background in the region of interest around the Q-value has to be sufficiently low. A large Q-value is advantageous due to the decreasing number of possible background contributions from radioactive decays as Q increases.

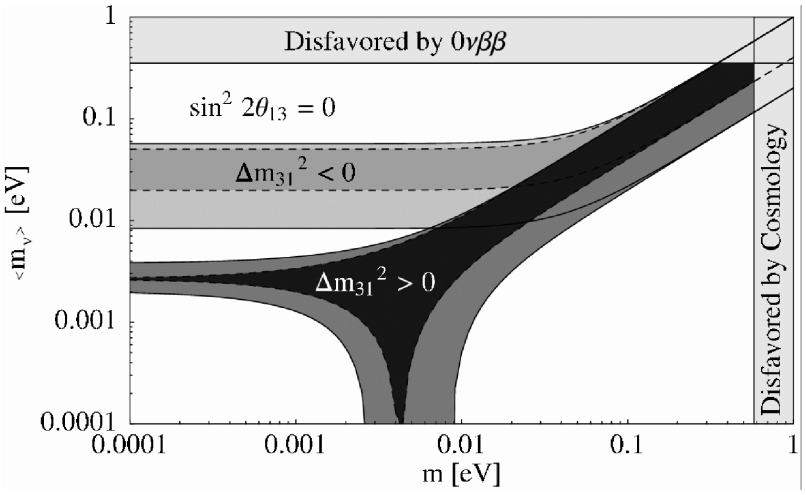

Figure 2.6: Effective Majorana neutrino mass, $\langle m_\nu \rangle$, as a function of the lightest neutrino mass, m. The light band corresponds to the inverted mass hierarchy, the dark band to the normal mass hierarchy. The mixing angle θ_{13} is assumed to be zero [53, 54]. The inner (outer) bands correspond to calculations without (with) the 3 σ-uncertainties on the oscillation parameters.

- A large target mass increases the number of possible decays. The background typically scales with the total mass (integrated over all isotopes), whereas the signal scales only with the double beta-isotope under consideration. A high natural abundance or isotopic enrichment will therefore lead to a better signal-to-background ratio.
- The signal efficiency has to be as high as possible.
- The background has to be as low as possible.

In the following, the background index is defined as the number of observed background events per kg (of total mass), per keV of the spectrum in the region of interest, per year and denoted counts/(kg·keV·y). An estimate of the sensitivity of double beta-decay experiments and the influence of the background are discussed in Chapter 4.

The number of observed $0\nu\beta\beta$-events, N, is related to the half-life of the process, $T_{1/2}^{0\nu\beta\beta}$. For a measuring time $t \ll T_{1/2}^{0\nu\beta\beta}$ the half-life can be expressed as

$$T_{1/2}^{0\nu\beta\beta} \approx \ln 2 \cdot \kappa \cdot M \cdot \epsilon_{\mathrm{sig}} \cdot \frac{N_{\mathrm{A}}}{M_{\mathrm{A}}} \cdot \frac{t}{N} \ , \tag{2.16}$$

where κ is the mass fraction of the isotope under study, M is the total mass and ϵ_{sig} is the signal efficiency. N_{A} is Advogadro's number and M_{A} is the atomic mass of the isotope.

Experiments are carried out to search for double beta-decay of different isotopes. Table 2.2 presents a selection of isotopes for which the experimentally important Q-value and natural abundances together with today's best limit on $0\nu\beta\beta$-decay are summarized. Also shown are the measured half-lives for the $2\nu\beta\beta$-decay. The claim of a discovery of $0\nu\beta\beta$-decay of ^{76}Ge is discussed in the next section.

Table 2.2: Q-value and natural abundance of possible candidates for $0\nu\beta\beta$-decay. Also summarized are the current measurements of the $2\nu\beta\beta$-decay (average values taken from [59]) and the current best limits on $0\nu\beta\beta$-decay. The nuclear matrix elements are taken from [57]. In the case of ^{76}Ge enriched material was used.

Isotope	Q-value [keV]	$\mathcal{M}_{0\nu}$	Nat. ab. κ [%]	$T^{2\nu\beta\beta}_{1/2}$ [y]	$T^{0\nu\beta\beta}_{1/2}$ [y] (90% C.L.)
^{76}Ge	2 039	2.40 ± 0.07	7.8	$(1.5 \pm 0.1) \cdot 10^{21}$	$> 1.9 \cdot 10^{25}$ [60]
^{82}Se	2 995	2.12 ± 0.10	9.2	$(1.0 \pm 0.1) \cdot 10^{20}$	$> 1.0 \cdot 10^{23}$ [61]
^{100}Mo	3 034	1.16 ± 0.11	9.6	$(7.1 \pm 0.4) \cdot 10^{18}$	$> 4.6 \cdot 10^{23}$ [61]
^{116}Cd	2 809	1.43 ± 0.08	7.5	$(3.0 \pm 0.2) \cdot 10^{19}$	$> 1.7 \cdot 10^{23}$ [62]
^{130}Te	2 530	1.47 ± 0.15	34.5	$(0.9 \pm 0.1) \cdot 10^{21}$	$> 1.8 \cdot 10^{24}$ [63]

2.4.3 Search for neutrinoless double beta-decay of ^{76}Ge

The germanium isotope ^{76}Ge is a possible candidate for $0\nu\beta\beta$-decay. It cannot decay into ^{76}As through a single beta-decay but into ^{76}Se via double beta-decay (see Figure 2.5). Its Q-value, denoted $Q_{\beta\beta}$ in the following, is 2 039 keV [64]. Germanium has two advantages compared to other isotopes: (1) it is the purest producible material in crystalline form and therefore has a very low content of intrinsic background sources, and (2) germanium crystals are semiconductors. This allows to use germanium as source and detector simultaneously. Very high signal efficiencies of above 90% are achievable for large cylindrical detectors. However, isotopic enrichment in ^{76}Ge is considered necessary for germanium double beta-decay experiments, because the natural abundance is only 7.8%.

The two most sensitive germanium double beta-decay experiments were the IGEX [1] (Canfranc, Spain) and Heidelberg-Moscow [2] (Gran Sasso, Italy) experiments. Both experiments used isotopically enriched germanium detectors.

The IGEX experiment ran from 1991 to 2000 with a total exposure of 8.8 kg·years (117 mole·years). The background index encountered was 0.17 counts/(kg·keV·y). A lower limit on the half-life of $0\nu\beta\beta$-decay of $T^{0\nu\beta\beta}_{1/2} > 1.6 \cdot 10^{25}$ y was deduced from the spectrum in the region of interest, depicted in Figure 2.7 (left).

The Heidelberg-Moscow (HdM) experiment ran from 1990 to 2003 with a total exposure of 71.1 kg·years and a background index of 0.11 counts/(kg·keV·y). The final energy

spectrum is shown in Figure 2.7 (right). Parts of the HdM collaboration interpret the peak at $Q_{\beta\beta}$ as a result of the decay under study and claim a discovery with 4.2 σ significance and a half-life of $T_{1/2}^{0\nu\beta\beta} = 1.2^{+0.4}_{-0.2}$ y [2]. An earlier publication presented a lower limit of $T_{1/2}^{0\nu\beta\beta} > 1.9 \cdot 10^{25}$ y [60].

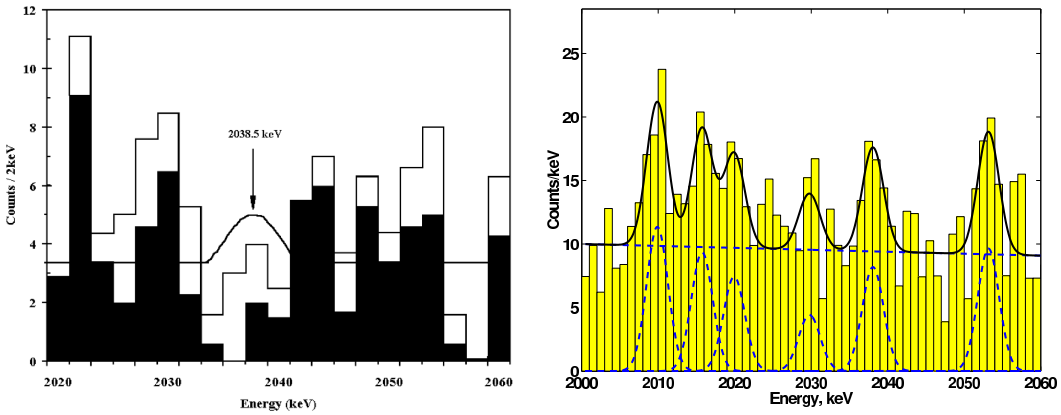

Figure 2.7: Left: Energy spectrum measured in the IGEX experiment for a total exposure of 8.8 kg·years (117 mole·years) [1]. The open and black histograms correspond to the energy spectrum without and with the application of pulse shape analysis, respectively. The black curve represents the 90% C.L. upper limit on the number of $0\nu\beta\beta$-events. Right: Energy spectrum measured in the HdM experiment for a total exposure of 71.1 kg·years [2]. The dashed line represents the estimated background level. The black curves represent fits to γ-lines in the vicinity of the $Q_{\beta\beta}$-value.

Two experiments to search for $0\nu\beta\beta$-decay of ^{76}Ge are planned. The MAJORANA experiment [65, 66] in the U.S. will operate about 200 kg enriched germanium detectors in conventional cryostats and shielding. A massive effort is being devoted to produce ultra-pure materials for the crystal environment. The GERmanium Detector Array, GERDA [3], is currently under construction in the Gran Sasso underground laboratory, Italy. It is described in more detail in Chapter 3.

Chapter 3

The GERDA experiment

The GERmanium Detector Array, GERDA [3], is a new experiment to search for $0\nu\beta\beta$-decay of ^{76}Ge. It is currently being installed in the Hall A of the INFN Gran Sasso National Laboratory (LNGS), L'Aquila, Italy. Its main design feature is to operate bare germanium detectors directly in a cryogenic liquid and minimize the amount of high-Z material in their vicinity.

The first objective of the experiment is to verify or reject the recent claim of discovery of $0\nu\beta\beta$-decay [2]. In case the discovery is verified, the statistical significance of the observation is expected to be improved. If the claim is rejected, an improved lower limit on the half-life of the $0\nu\beta\beta$-process can be set. Emphasis is placed on the reduction of background. The design goal is to reach a background index of less than 10^{-3} counts/(kg·keV·y) in the region of interest. This is two orders of magnitude below the background level reached in previous experiments. A lower limit on the half-life of $T_{1/2}^{0\nu\beta\beta} > 13.5 \cdot 10^{25}$ y can be set with the envisioned total exposure of 100 kg·years [1].

The concept of the experiment is based on ideas presented in [67]. The location and technical realization of the project are discussed in the following. This chapter closes with the status of the GERDA experiment as of Winter 2006/07. Separate chapters on germanium detectors (Chapter 5) and background reduction techniques (Chapter 6) follow and complete the description of the main features of the experiment.

3.1 Concept

Based on the experiences from recent double beta-decay experiments strategies were developed to reduce the background in new experiments. Sources of background are cosmogenically produced radioactive isotopes in the detectors, muon induced neutrons and electromagnetic showers, and radioactive isotopes in the surrounding of the detectors. The strategies incorporated in the concept of GERDA are summarized here:

[1] For a calculation of the sensitivity of GERDA see Chapter 4.

- Choice of location: cosmic radiation makes low background experiments at sea level impossible due to hadron and muon induced background and cosmogenic activation. In order to attenuate the flux of cosmic muons and to shield the hadronic component of the cosmic radiation the experiment is located underground.

- Choice of materials: as most of the radioactive background comes from natural decay chains, materials are chosen which have minimal radio-impurities (often levels of the order of μBq/kg are aimed at). Screening experiments are carried out and intercomparisons between different measuring techniques are needed to verify such levels.

- Reduction of material: even with radio-pure materials it is important to reduce the amount of high-Z material close to the detectors. The operation of germanium detectors in an ultra-pure cryogenic liquid allows to remove the conventional cryostats. Instead, especially designed detector suspensions are developed which use a minimum of material to support the germanium crystals.

- Shielding: the GERDA design foresees a multi-layer shielding to reduce external radiation. Water as the outermost shell acts as neutron absorber and moderator. A steel cryostat with copper lining shields external γ-radiation. The cryogenic liquid which surrounds the detector array further suppresses external γ-radiation as well as radiation from the cryostat itself.

- Waiting: the half-lives of the cosmogenically produced isotopes ^{60}Co and ^{68}Ge are 5.3 y and 271 d, respectively. Storing the detectors underground and simply waiting will reduce the number of radioactive nuclei.

GERDA will use enriched high-purity germanium detectors as source and detector simultaneously. In contrast to previous experiments the detectors are not cooled by a copper cooling finger but are directly inserted into the center of a multi-meter cryogenic buffer. The baseline design foresees liquid argon as buffer. Liquid argon can be produced with a much greater purity than lead or even copper traditionally used for shielding. The cryogenic liquid will be contained in a copper-lined steel vessel and surrounded by a buffer of ultra-pure water. The 10 m diameter water tank will be instrumented with photo multipliers in order to collect Cherenkov light from traversing cosmic muons. The super-structure is mechanically independent of the water tank. A clean room on top of the super-structure houses a lock through which the detectors are inserted into the cryogenic buffer. Plastic scintillator plates on top of the clean room complete the muon veto. Figure 3.1 shows the Hall A of the LNGS before the construction of the GERDA infrastructure (left) and an engineer's view of the experiment (right).

Detectors enriched in the isotope ^{76}Ge to a level of about 86% will be deployed as well as reference detectors made out of natural germanium. A phased approached is chosen for the experiment.

Figure 3.1: Left: Hall A of the LNGS before the construction of the GERDA infrastructure. Right: Engineer's view of the experiment.

In the first phase (Phase I) detectors which were previously operated by the IGEX [1] and HdM [2] collaborations will be re-deployed. The enriched detectors have a mass of approximately 18 kg in total. For Phase I the envisioned background index is 10^{-2} counts/(kg·keV·y). The estimated 90% probability lower limit on the half-life of $0\nu\beta\beta$-decay, assuming an exposure of about 15 kg·years, is $T_{1/2}^{0\nu\beta\beta} > 2 \cdot 10^{25}$ y.

The detectors for the second phase (Phase II) are still under construction. Approximately 20 kg of enriched germanium will be used in addition. The background index aimed at is 10^{-3} counts/(kg·keV·y). An exposure of 100 kg·years is expected resulting in an expected lower limit on the half-life of $T_{1/2}^{0\nu\beta\beta} > 13.5 \cdot 10^{25}$ y. A 1 000 kg-scale experiment is under discussion in cooperation with the MAJORANA collaboration in a later phase (Phase III).

Novel approaches for the identification and reduction of background events are developed for and discussed in the context of GERDA. These range from the use of segmented germanium detectors in Phase II [68, 69] to the instrumentation of liquid argon as an active veto against photons [70–72]. An overview of the background reduction techniques developed is given in Section 6.4 after the main sources of background are discussed.

3.2 Location of the experiment - LNGS

The GERDA experiment will be located in the Hall A of the INFN Gran Sasso National Laboratory (LNGS), L'Aquila, Italy. It is the worlds largest underground facility for low-background experiments with three halls (each about 100 m times 20 m times 18 m in size). The halls are accessed from a 10 km long freeway tunnel under the Gran Sasso mountains. A large variety of experiments is hosted in the LNGS, most of them focussed on dark matter or neutrino physics.

The overburden of 1 400 m of rock (corresponding to 3 400 meter of water equivalent, m.w.e.) reduces the external muon flux induced by cosmic rays by a factor of one million compared to the surface. The neutron flux is reduced by a factor of one thousand compared to the surface. The content of uranium and thorium in the rock is low. The flux of muons and the activity of radioactive isotopes in the walls of the tunnel are well known.

The location of GERDA is indicated in Figure 3.2 which shows a floor plan of the LNGS laboratory. It is juxtaposed by the Large Volume Detector (LVD) experiment from the north and restricted by a service tunnel from the south. Parts of the cryogenic system, such as tanks for the cryogenic liquid, will be located in the service tunnel towards the east.

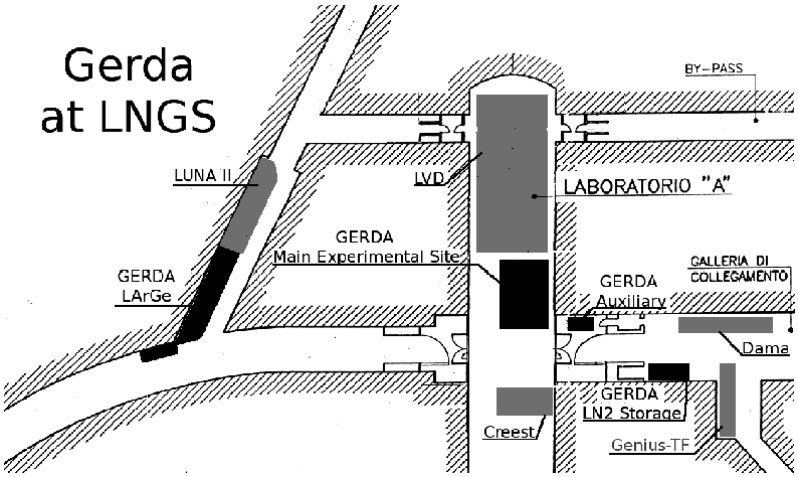

Figure 3.2: Floor plan of the LNGS. The GERDA experiment will be located in Hall A situated between the LVD experiment and a service tunnel.

3.3 Technical realization

The baseline design for the GERDA experiment as of Winter 2006/07 is presented in the following. Since the experiment is still under construction, parts of the design or construction might undergo a revision. Technical details can be found in [73].

3.3.1 Active detector components

The detector has two active sub-systems, the array of germanium detectors and the muon veto system.

Germanium detectors: The detector array consists of hexagonally packed detectors with up to 5 layers. Up to 19 detectors can be placed per layer. The horizontal distance between the centers of two detectors is 9 cm. The vertical clearance between two detectors

is 5 cm. The array is divided into strings of vertically aligned detectors. Figure 3.3 (left) shows a seven string array of germanium detectors as designed for the Phase II of the GERDA experiment. The same figure (right) shows a top view of the full array indicating the possible positions for the Phase I and Phase II detector strings as well as for the calibration sources.

The Phase I detectors are p-type diodes with a cylindrical closed-ended coaxial geometry. The detectors are enriched in ^{76}Ge to a level of about 86% and have masses between 0.9 kg and 2.9 kg.

The detectors for Phase II will be cylindrical true coaxial n-type diodes. The precise size of the detectors will depend on manufacturing details. The most likely dimensions are a height of 70 mm and a diameter of 75 mm. The detectors will be segmented. The segmentation scheme under consideration is a 6-fold segmentation in the azimuthal angle ϕ and a 3-fold segmentation in the height z. Light-weight holders were designed for the Phase II detectors together with a novel contacting scheme. The holders are made out of approximately 30 g of copper. Figure 3.4 (left) shows a Phase II prototype detector mock-up with its cabling and holder structure.

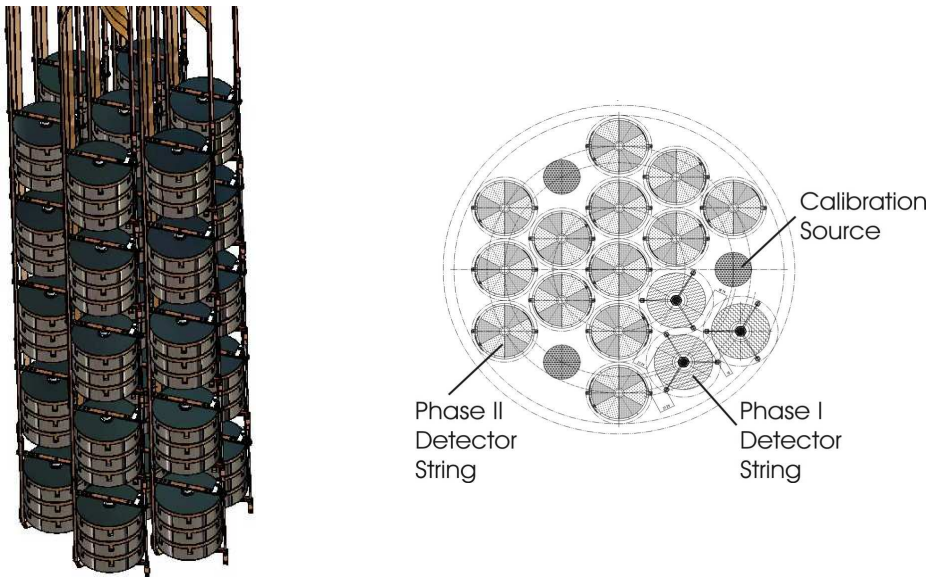

Figure 3.3: Left: An array of 7×5 germanium detectors as described in the text. Right: Top view of the full array indicating the possible positions for the Phase I and Phase II detector strings as well as for the calibration sources.

Figure 3.4: Left: A Phase II detector mock-up with its cabling scheme and holder structure. Right: Unloading of the GeO_2 from the transport container in Munich.

Muon veto: The muon veto consists of two parts: the instrumented water tank operated as a Cherenkov detector and the plastic scintillator plates on top of the clean room.

66 photomultiplier tubes (PMTs) will be installed on the walls of the water tank. Six PMTs will be positioned in an optically screened *pillbox* below the cryostat. Monte Carlo studies were performed to find the most efficient positioning of the PMTs. Cosmic muons traversing the water buffer will cause Cherenkov radiation which will be collected by the PMTs. The efficiency to detect such muons is about 95% depending on the incident angle. The PMTs will be encapsulated in a stainless steel housing with a polyethylene window. The design is close to that used in the BOREXINO experiment [74].

The plastic scintillator will be triggered by traversing muons. It is designed to detect those muons which enter the detector almost vertically. It completes the muon veto and compensates for the missing water volume around the neck of the cryostat. The combined detection efficiency of muons is expected to be about 99%.

3.3.2 Water tank and cryogenic vessel

The water tank will be made out of stainless steel. It will have an outer diameter of 10 m and a height of about 8 m resulting in a water volume of approximately 630 m^3. The tank will be filled with ultra-pure water.

The cryostat will be placed inside the water tank and made out of stainless steel with an internal copper shield. The vessel height will be 5.6 m (8.9 m with the neck) while the outer diameter is foreseen to be 4.2 m. A total of approximately 98 t of liquid argon

will be stored inside the cryostat. The thickness of the copper shield will depend on the radio-purity of the steel and has yet to be determined. The required upper limit on the contamination of the ultra-pure argon is of the order of several 10^{-16} g/g for ^{232}Th and ^{238}U.

3.3.3 Super-structure and clean room

The super-structure is composed of a platform and three levels of laboratory cabins on the back of the water tank. A class 10 000 clean room with radon-reduced air will be built on top of the platform. It will house a lock through which detector strings are inserted into and removed from the cryogenic volume. Detector handling will be performed in flow-boxes and a detector mounting station which will reach class 100. The lock consists of a rail system which allows to move detector strings into their correct position and lower them into the cryostat. In addition, the clean room will be used to temporarily store germanium detectors under a controlled atmosphere of gaseous argon. Final preparations and testing of the germanium detectors will also be done here.

3.3.4 Electronics and data acquisition system

Several designs for the pre-amplifiers for the germanium detectors and the data acquisition system are studied. For details on the development of the electronics see [75, 76]. Tests of the electronics with a string of germanium detectors are planned for the near future.

3.4 Status of the experiment

The construction of the GERDA infrastructure is expected to start in 2007. The commissioning of the detector and the first data taking are planned to start within two years after the beginning of the construction work.

The Phase I detectors were taken out of their cryostats and will be refurbished. The contacting will be changed and the diodes will be mounted onto new holders in order to fit into the detector strings. First tests of the refurbishing and mounting procedures yielded promising results. The detectors are currently at the manufacturer's site. They will be tested in the Gerda Detector Lab at the LNGS.

A total of 37.5 kg of enriched germanium was produced via ultra-centrifugation of gaseous GeF_4. The centrifugation and the subsequent chemical transformation of the material into GeO_2 were performed in Zelenogorsk, Russia. The chemical purity was measured to be $> 99.9\%$. The isotopic enrichment in ^{76}Ge was measured to be 86-88%. A special transport container was designed and built in cooperation with the Institute of Nuclear Research in Moscow to reduce the activation of the germanium due to cosmic radiation. The GeO_2 was sent to Munich where it was weighed and then transferred to the HADES underground facility [77]. It is currently stored at a depth of about 500 m.w.e.

In a next step the material will be purified to 6N (99.9999%) which is referred to as *electronic grade*. Once the purification is done the material will be further purified to >9N by zone refinement and to 11N–12N by crystal growing via the Czochralksi method. The final processing step is the production of detectors from the germanium crystals. Several options for the production of the Phase II detectors are being investigated at the moment. Figure 3.4 (right) shows the unloading of the GeO_2 from the transport container in Munich.

Chapter 4

Sensitivity of the GERDA experiment

The sensitivity of low background experiments is determined by the number of observed signal and background events. Common approximations, valid only for large numbers, fail for the small number of events encountered. A Bayesian analysis of the probability of a signal in the presence of background is developed [78], and criteria are proposed for claiming evidence for, or the discovery of a signal. The analysis is independent of the physics case and can be applied to a variety of situations.

Model comparisons from a Bayesian perspective have been discussed extensively in the literature [79]. These analyses typically calculate the *odds* for one model to be correct relative to the other(s) [80]. Here, a somewhat different approach was taken in that a procedure for claiming a discovery is proposed - i.e., for claiming that known processes alone are not enough to describe the observation.

Predictions about possible outcomes of an experiment are based on calculated distributions of observables. As an approximation, ensembles, sets of Monte Carlo data which mimic the expected distribution, are generated and analyzed. The frequency distributions of output parameters of the Bayesian analysis are interpreted as probability densities and are used to evaluate the sensitivity of the experiment to the process under study. As an example, the analysis method is used to estimate the sensitivity of the GERDA experiment to neutrinoless double beta-decay.

First, the analysis strategy is introduced in Section 4.1. The generation of ensembles and the application of the method is discussed in Section 4.2. In Section 4.3 the sensitivity of the GERDA experiment is evaluated.

4.1 Spectral analysis

A common situation in the analysis of data is that two types of processes (referred to as signal and background in the following) potentially contribute to a measured spectrum. The basic questions are: *What is the contribution of the signal process to the observed spectrum? What is the probability that the spectrum is due to background only? Given models for the signal and the background, what is the (most probable) number of signal events in the spectrum? In case that no signal is observed, what is the limit that can be set on the signal contribution?* The analysis method introduced here is based on Bayes' Theorem and developed to answer these questions. It is particularly suitable for spectra with a small number of events.

The assumptions for the analysis are

- The spectrum is confined to a certain region of interest.
- The spectral shape of a possible signal is known.
- The spectral shape of the background is known[1].
- The spectrum is binned and the number of events in each bin follows a Poisson distribution.

The analysis consists of two steps. First, the probability that the observed spectrum is due to background only is calculated. If this probability is less than an *a priori* defined value, the discovery (or evidence) criterion, the signal process is assumed to contribute to the spectrum and a discovery (or evidence) is claimed. If the process is known to exist, this step is skipped. If discovery is claimed the signal contribution is estimated in a second step. Otherwise an upper limit for the signal contribution is calculated.

4.1.1 Hypothesis test

In the following H_1 denotes the hypothesis that the observed spectrum is due to background[2] only; the negation, interpreted here as the hypothesis that the signal process contributes to the spectrum, is labeled H_2. The conditional probabilities for the hypotheses H_1 and H_2 to be true given the measured spectrum are labeled $p(H_1|\text{data}, I)$ and $p(H_2|\text{data}, I)$, respectively. The I represents all additional information used to propose the hypotheses. The conditional probabilities obey the following relation:

$$p(H_1|\text{data}, I) + p(H_2|\text{data}, I) = 1\,. \tag{4.1}$$

[1] This assumption and the previous can be removed in a straightforward way with the introduction of additional prior densities.

[2] In this analysis the shape of the background spectrum is assumed to be known. Only the overall level of background is allowed to vary. The case of unknown background sources contributing to the measured spectrum could be incorporated, but is ignored here.

The conditional probabilities for H_1 and H_2 are calculated using Bayes' Theorem:

$$p(H_1|\text{data}, I) = \frac{p(\text{data}|H_1, I) \cdot p_0(H_1|I)}{p(\text{data}|I)} \tag{4.2}$$

and

$$p(H_2|\text{data}, I) = \frac{p(\text{data}|H_2, I) \cdot p_0(H_2|I)}{p(\text{data}|I)}\,, \tag{4.3}$$

where $p(\text{data}|H_1, I)$ and $p(\text{data}|H_2, I)$ are the conditional probabilities to find the observed spectrum given that the hypothesis H_1 is true or not true, respectively, and $p_0(H_1|I)$ and $p_0(H_2|I)$ are the prior probabilities for H_1 and H_2 [3]. The values of $p_0(H_1|I)$ and $p_0(H_2|I)$ are chosen depending on the additional information, I, such as existing knowledge from previous experiments and model predictions. In the following, the symbol I is dropped for simplicity. The probability $p(\text{data})$ is written as

$$\begin{aligned} p(\text{data}) &= p(\text{data}|H_1) \cdot p_0(H_1) + \\ &\quad\; p(\text{data}|H_2) \cdot p_0(H_2)\,. \end{aligned} \tag{4.4}$$

The probabilities $p(\text{data}|H_1)$ and $p(\text{data}|H_2)$ can be decomposed in terms of the expected number of signal events, S, and the expected number of background events, B:

$$\begin{aligned} p(\text{data}|H_1) &= \int p(\text{data}|B) \cdot p_0(B)\; dB\,, \\ p(\text{data}|H_2) &= \int p(\text{data}|S, B) \cdot p_0(S) \cdot p_0(B)\; dS\; dB\,, \end{aligned} \tag{4.5}$$

where $p(\text{data}|B)$ and $p(\text{data}|S, B)$ are the conditional probabilities to obtain the measured spectrum. Further, $p_0(S)$ and $p_0(B)$ are the prior probabilities for the number of signal and background events, respectively. They are assumed to be uncorrelated.

The *observed* number of events in the ith bin of the spectrum is denoted n_i. The fluctuations in the bins of the spectrum are assumed to be uncorrelated. Then the probability to observe the measured spectrum is simply derived by multiplying the probabilities for each bin. The *expected* number of events in the ith bin, λ_i, can be expressed in terms of S and B:

$$\begin{aligned} \lambda_i &= \lambda_i(S, B) \\ &= S \cdot \int_{\Delta E_i} f_{\text{S}}(E)\; dE + B \cdot \int_{\Delta E_i} f_{\text{B}}(E)\; dE\,, \end{aligned} \tag{4.6}$$

where $f_{\text{S}}(E)$ and $f_{\text{B}}(E)$ are the normalized shapes of the known signal and background spectra, respectively, and ΔE_i is the width of the ith bin. The letter E suggests an energy

[3] Prior probabilities summarize what is *a priori* known about a variable or hypothesis before the measurement.

bin but the binning can be performed for any distribution. The number of events in each bin can fluctuate around λ_i according to a Poisson distribution. This yields

$$p(\text{data}|B) = \prod_{i=1}^{N} \frac{\lambda_i(0,\ B)^{n_i}}{n_i!} e^{-\lambda_i(0,\ B)} =: \Lambda_B \ , \tag{4.7}$$

$$p(\text{data}|S,B) = \prod_{i=1}^{N} \frac{\lambda_i(S,B)^{n_i}}{n_i!} e^{-\lambda_i(S,B)} =: \Lambda_{S,B} \ . \tag{4.8}$$

In summary, the probability for H_1 to be true, given the measured spectrum, is:

$$p(H_1|\text{data}) = \frac{\left[\int \Lambda_B \cdot p_0(B)\ dB\right]_{S=0} \cdot p_0(H_1)}{\left[\int \Lambda_B \cdot p_0(B)\ dB\right]_{S=0} \cdot p_0(H_1) + \left[\int \Lambda_{S,B} \cdot p_0(B) \cdot p_0(S)\ dB\ dS\right] \cdot p_0(H_2)} \ , \tag{4.9}$$

with Λ calculated based on Equations (4.6, 4.7 and 4.8). The decision about a signal discovery is based on the value of $p(H_1|\text{data})$. It should be emphasized that the discovery criterion should be agreed to by consensus before the experiment starts. A value of $p(H_1|\text{data}) \leq 0.0001$ is proposed for the *discovery* criterion, whereas a value of $p(H_1|\text{data}) \leq 0.01$ can be considered to give *evidence* for H_2.

The analysis can easily be extended to include systematic uncertainties of the measurement. For example, if the spectrum is plotted as a function of energy and the energy scale has an uncertainty, the right hand sides of Equations (4.7,4.8) can be rewritten as

$$\int \left[\prod_{i=1}^{N} \frac{\lambda_i(0,\ B|k)^{n_i}}{n_i!} e^{-\lambda_i(0,\ B|k)} \right] p_0(k) dk \ , \tag{4.10}$$

$$\int \left[\prod_{i=1}^{N} \frac{\lambda_i(S,B|k)^{n_i}}{n_i!} e^{-\lambda_i(S,B|k)} \right] p_0(k) dk \ . \tag{4.11}$$

where $\lambda_i(S,B|k)$ is the expected number of events for a given energy scale factor k and $p_0(k)$ is the probability density for k (e.g., a Gaussian distribution centered on $k = 1$).

4.1.2 Signal parameter estimate

In case the spectrum fulfills the requirement of evidence or discovery, the number of signal events is estimated from the data. The probability that the observed spectrum can be explained by the set of parameters S and B, making again use of Bayes' Theorem, is:

$$p(S,\ B|\text{data}) = \frac{p(\text{data}|S,B) \cdot p_0(S) \cdot p_0(B)}{\int p(\text{data}|S,B) \cdot p_0(S) \cdot p_0(B)\ dS\ dB} \ . \tag{4.12}$$

In order to estimate the signal contribution the probability $p(S, B|\text{data})$ is marginalized with respect to B:

$$p(S|\text{data}) = \int p(S, B|\text{data})\ dB\ . \tag{4.13}$$

The mode of this distribution, S^*, i.e., the value of S which maximizes $p(S|\text{data})$, is used as an estimate for the signal contribution. The standard uncertainty of S can be evaluated from

$$\begin{aligned} \int_0^{S_{16}} p(S|\text{data})\ dS &= 0.16\ , \\ \int_0^{S_{84}} p(S|\text{data})\ dS &= 0.84\ , \end{aligned}$$

such that the result can be quoted as

$$S^{*\,+(S_{84}-S^*)}_{\ -(S^*-S_{16})}\ . \tag{4.14}$$

4.1.3 Setting limits on the signal parameter

In case the requirement for a discovery of or evidence for the signal process is not fulfilled an upper limit on the number of signal events is calculated. For example, a 90% probability limit is calculated by integrating Equation (4.13) to 90% probability:

$$\int_0^{S_{90}} p(S|\text{data})\ dS = 0.90\ . \tag{4.15}$$

S_{90} is the 90% probability upper limit on the number of signal events. It should be noted that in this case it is assumed that H_2 is true but the signal process is too weak to significantly contribute to the spectrum.

4.2 Ensemble tests

The possible outcomes of an experiment can be evaluated by calculating the expected distributions of the observables. This is useful for comparing the sensitivities of different experiments under consideration. A given experimental setup is repeatedly simulated from the same conditions (such as the prior probabilities) and distributions of possible outcomes are determined. The sensitivity of an experiment is then assessed by determining how often a discovery can be claimed. The calculation is done numerically by generating possible spectra and subsequently analyzing them. The spectra are typically generated from Monte Carlo simulations of signal and background events. Events are grouped into ensembles. For a given ensemble the expected number of signal and background events, S_0 and B_0, are

fixed and a random number of events are collected according to Poisson distributions. A spectrum is extracted for each ensemble and subsequently analyzed. The computational flow chart is shown in Figure 4.1. As an example, the probability $p(H_1|\text{data})$ for each spectrum is depicted here as the outcome of the analysis. This approach is referred to as *ensemble tests*.

Systematic uncertainties, such as the influence of the energy resolution, a possible miscalibration, or signal and background efficiencies, can be estimated by analyzing ensembles which are generated under different assumptions.

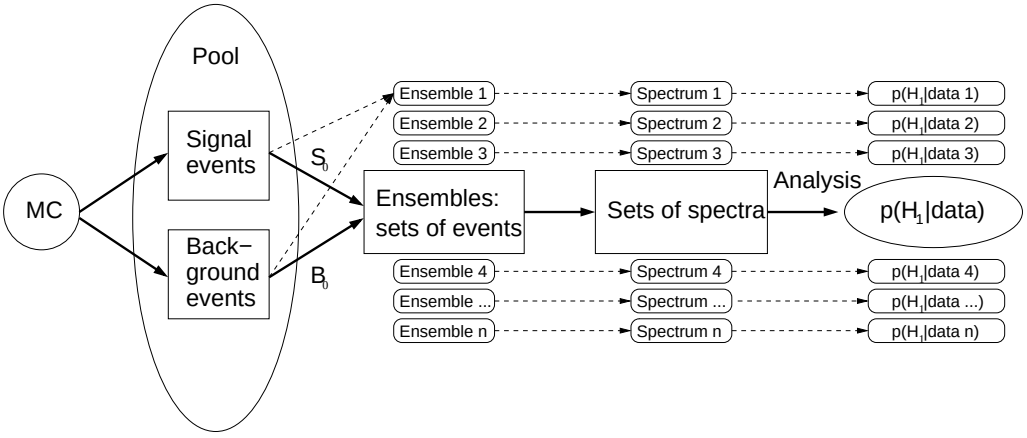

Figure 4.1: Computational flow chart. The Monte Carlo generator (MC) generates a pool containing signal and background events. An ensemble is defined as a set of events representing a possible outcome of an experiment. The number of events in each ensemble is randomly chosen according to the parameters S_0 and B_0. A spectrum is extracted for each ensemble and subsequently analyzed. The probability $p(H_1|\text{data})$ for each spectrum is depicted here as the outcome of the analysis.

4.3 Result

In the following, the Bayesian analysis method developed in Section 4.1, is applied to Monte Carlo data. The sensitivity of GERDA is evaluated.

4.3.1 Expected spectral shapes and prior probabilities

The signature of neutrinoless double beta-decay, the signal process, is a sharp spectral line at the $Q_{\beta\beta}$-value which for the germanium isotope ^{76}Ge is at 2 039 keV. The shape of the signal contribution is assumed to be Gaussian with the mean at the $Q_{\beta\beta}$-value. The energy resolution of the germanium detectors in the GERDA setup is expected to be 5 keV (full width at half maximum, FWHM), corresponding to a width of the signal Gaussian of $\sigma \approx 2.1$ keV. In the following, the region of interest is defined as an energy window of

± 50 keV around the $Q_{\beta\beta}$-value. In GERDA, the energy spectrum in the region of interest is expected to be populated by events from various background processes. The shape of the background spectrum is assumed to be flat, i.e., $f_{\mathrm{B}}(E) = const.$ This assumption was validated by Monte Carlo simulations (see Section 7.1 and Chapter 12).

Ensembles are generated with varying (1) the exposure and (2) the half-life of the $0\nu\beta\beta$-process. The half-life and the exposure are translated into the number of expected signal events, S_0. Also varied is (3) the background index in the region of interest which is translated into the number of expected background events, B_0. The number of signal and background events in each ensemble fluctuate around their expectation values, S_0 and B_0, according to a Poisson distribution. The exposure ranges from 5 kg·y to 100 kg·y, the half-life of the $0\nu\beta\beta$-process ranges from $0.5 \cdot 10^{25}$ y to $20 \cdot 10^{25}$ y. Four different background scenarios were studied ranging from no background to a background index of 10^{-2} counts/(kg·keV·y). For each set of input parameters 1 000 ensembles are generated. An energy spectrum is extracted from each ensemble with a bin size of 1 keV.

In order to calculate the probability that a spectrum is due to background processes only, the prior probabilities for the hypothesis H_1 and H_2 have to be fixed, as well as those for the signal and background contributions. This is a key step in the Bayesian analysis. Given the lack of theoretical consensus on the Majorana nature of neutrinos and the cloudy experimental picture, the prior probabilities for H_1 and H_2 are chosen to be equal, i.e.,

$$p_0(H_1) = 0.5\,, \tag{4.16}$$

$$p_0(H_2) = 0.5\,. \tag{4.17}$$

The prior probability of the number of expected signal events, assuming H_2, is assumed to be flat up to a maximum value, S_{max}, consistent with existing limits [4]. It should be noted that the setting of the prior probability for H_1 is dependent on the maximum allowed signal rate. S_{max} was chosen in such a way that the probability for the hypothesis H_1 is reasonably assumed to be 50 %. The effect of choosing a different prior for the number of signal events is discussed below.

The background contribution, B, is assumed to be known within some uncertainty (recall that the shape of the background is fixed). The prior probability for B is chosen to

[4] S_{max} was calculated using Equation (2.16) assuming a half-life of $T_{1/2}^{0\nu\beta\beta} = 0.5 \cdot 10^{25}$ years.

be Gaussian with a mean value $\mu_{\mathrm{B}} = B_0$ and a width $\sigma_{\mathrm{B}} = B_0/2$. The prior probabilities for the expected signal and background contributions are

$$p_0(S) = \begin{cases} \frac{1}{S_{\max}} & (0 \leq S \leq S_{\max}) \\ 0 & (\text{otherwise}) \end{cases} \tag{4.18}$$

$$p_0(B) = \begin{cases} \frac{e^{-\frac{(B-\mu_{\mathrm{B}})^2}{2\sigma_{\mathrm{B}}^2}}}{\int_0^\infty e^{-\frac{(B-\mu_{\mathrm{B}})^2}{2\sigma_{\mathrm{B}}^2}} dB} & (B \geq 0) \\ 0 & (B < 0) \end{cases} \tag{4.19}$$

4.3.2 Ensembles

Figure 4.2 (top, left) shows the spectrum extracted from one Monte Carlo ensemble generated under the assumptions of a half-life of $2 \cdot 10^{25}$ years, a background index of 10^{-3} counts/(kg·keV·y) and an exposure of 100 kg·years. It corresponds to $S_0 = 20.5$ and $B_0 = 10.0$. The (20) signal and (8) background events are indicated by open and shaded histograms, respectively. Figure 4.2 (top, right) shows the marginalized probability density for S, $p(S|\text{data})$, for this spectrum. The mode of the distribution is $S^* = 19.8$, consistent with the number of signal events in the spectrum. Figure 4.2 (bottom, left) shows the distribution of S^* for 1 000 ensembles generated under the same assumptions. The average number of $S^* = 20.3$ is in agreement with the average number of generated signal events, 20.4. Figure 4.2 (bottom, right) shows the distribution of the $\log p(H_1|\text{data})$ for the 1 000 ensembles. More than 97% of the ensembles have a probability $p(H_1|\text{data})$ of less than 0.01%. I.e., a discovery would not be claimed for less than 3% of the ensembles under these conditions.

In order to simulate the case in which only a lower limit on the half-life of the $0\nu\beta\beta$-process is set, ensembles are generated without signal contribution, i.e., $S_0 = 0$. As an example, Figure 4.3 (top, left) shows a spectrum of Monte Carlo data generated under the assumptions of a background index of 10^{-3} counts/(kg·keV·y) and an exposure of 100 kg·years. No signal events are present in the spectrum. Figure 4.3 (top, right) shows $p(S|\text{data})$, for the same spectrum. The mode of S is 0 events. Figure 4.3 (bottom, left) shows the distribution of the limit (90% probability) of the signal contribution for 1 000 ensembles generated under the same assumptions. The average limit is 3.1 events. Figure 4.3 (bottom, right) shows the distribution of $p(H_1|\text{data})$ for ensembles generated under the same assumptions. For none of the ensembles would a discovery be claimed.

4.3.3 Sensitivity

For the ensembles generated without signal contribution the mean of the 90% probability lower limit on the half-life is shown in Figure 4.4 (left) as a function of the exposure for different background indices. If no background is present, the limit scales linearly

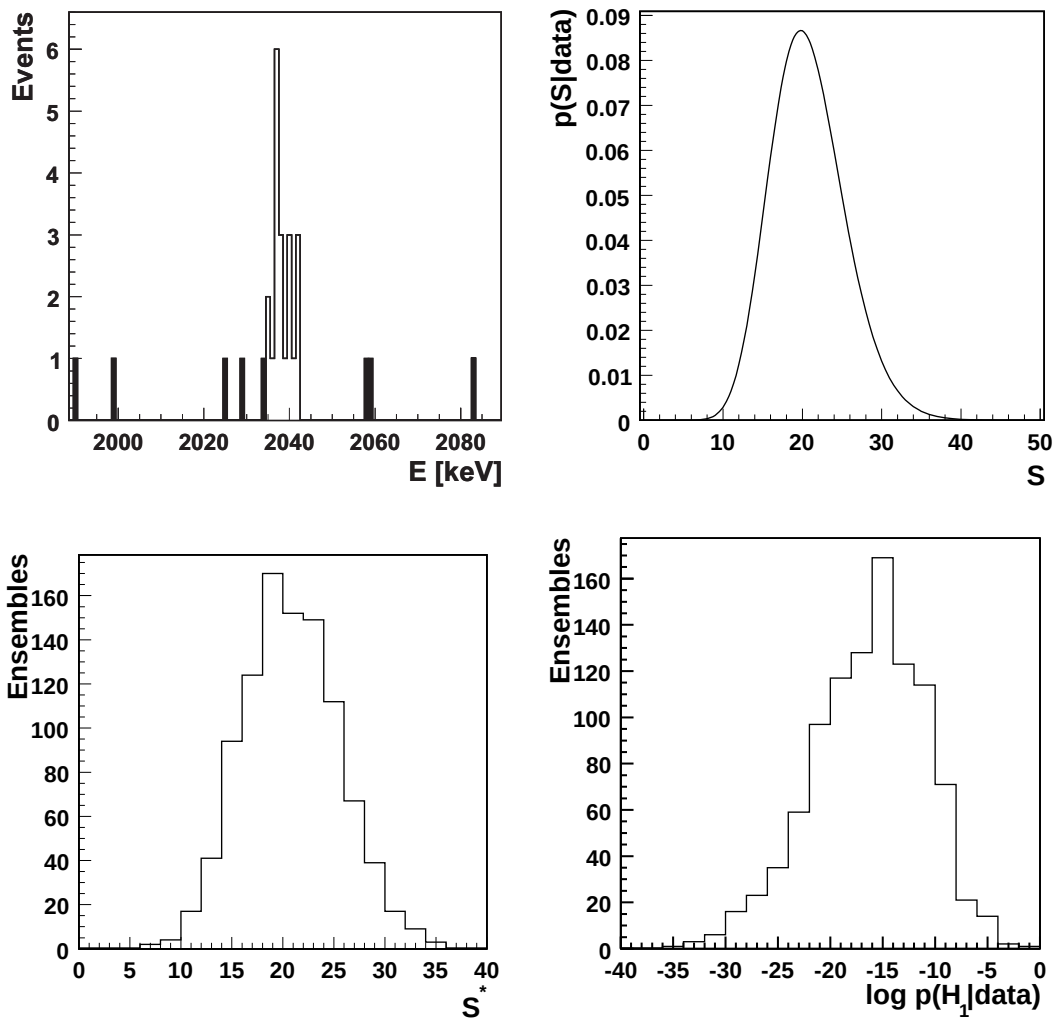

Figure 4.2: The spectrum (top, left) was generated as described in the text. The signal events are indicated by the open histogram, the background events by the shaded histogram. The probability density for S (top, right) from this spectrum is shown. The distribution of S^* (bottom, left) as well as the distribution of the $\log p(H_1|\text{data})$ (bottom, right) are calculated for 1 000 ensembles.

with the exposure. The limit on the half-life increases more slowly with increasing background contribution. An average lower limit of $T_{1/2}^{0\nu\beta\beta} > 13.5 \cdot 10^{25}$ years can be set for the envisioned background index of 10^{-3} counts/(kg·keV·y) and an expected exposure of 100 kg·years. For the same exposure, the average lower limit is $T_{1/2}^{0\nu\beta\beta} > 6.0 \cdot 10^{25}$ years and $T_{1/2}^{0\nu\beta\beta} > 18.5 \cdot 10^{25}$ years for background indices of 10^{-2} counts/(kg·keV·y) and 10^{-4} counts/(kg·keV·y), respectively.

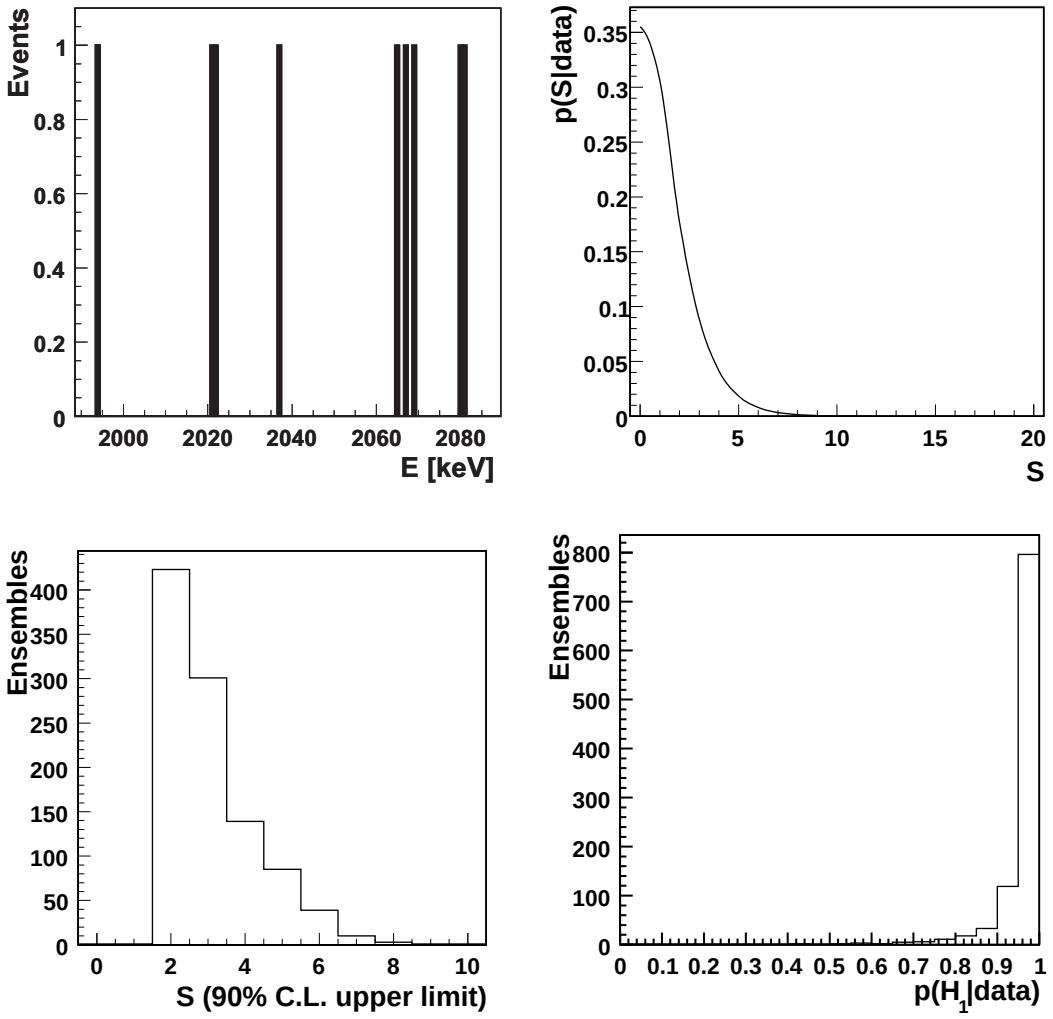

Figure 4.3: The spectrum (top, left) was generated as described in the text. No signal events are present in the spectrum. The probability density for S for this spectrum (top, right) is shown. The distribution of the limit (90% probability) of the signal contribution (bottom, left) as well as the distribution of the $p(H_1|\text{data})$ (bottom, right) are calculated for 1 000 ensembles.

A lower limit on the half-life of the $0\nu\beta\beta$-process can be translated into an upper limit on the effective Majorana neutrino mass, $\langle m_\nu \rangle$, using the nuclear matrix elements quoted in [81]:

$$\langle m_\nu \rangle = (T_{1/2}^{0\nu\beta\beta} \cdot G_{0\nu})^{-1/2} \cdot \frac{1}{|\mathcal{M}_{0\nu}|}\,, \tag{4.20}$$

where $G_{0\nu}$ is a phase space factor and $|\mathcal{M}_{0\nu}|$ is the nuclear matrix element. Figure 4.4 (right) also shows the expected 90% probability upper limit on the effective Majorana neutrino mass as a function of the exposure. With a background index of 10^{-3} counts/(kg·keV·y)

and an exposure of 100 kg·years, an upper limit of $\langle m_\nu \rangle < 200$ meV can be set assuming no $0\nu\beta\beta$-events are observed.

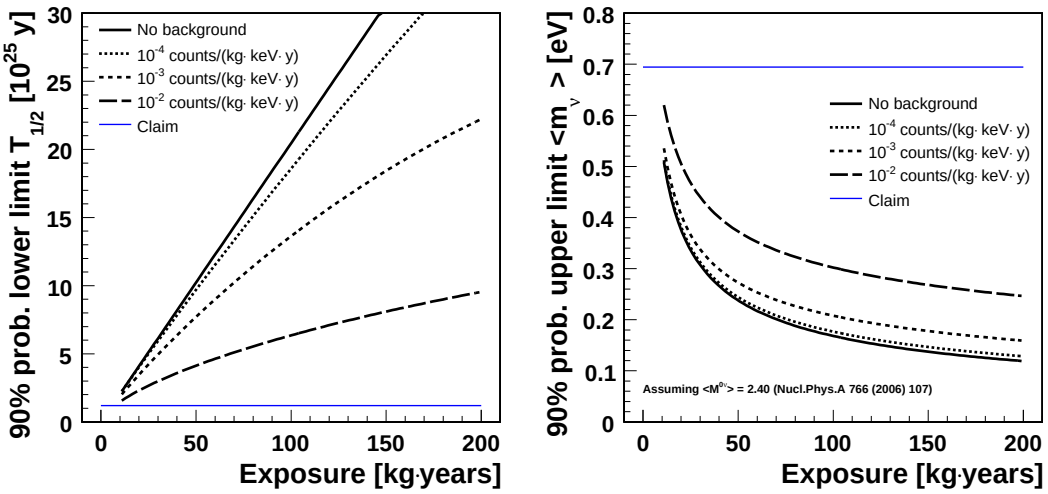

Figure 4.4: The left plot shows the expected 90% probability lower limit on the half-life for neutrinoless double beta-decay versus the exposure for different background conditions. Also shown is the half-life for the claimed observation [2]. The right plot shows the expected 90% probability upper limit on the effective Majorana neutrino mass versus the exposure. The effective Majorana neutrino mass for the claimed observation is also shown. The mass values were determined from the half-life using the matrix element reported in [81].

Figure 4.5 (right) shows the half-life for which 50% of the experiments would report a discovery of neutrinoless double beta-decay as a function of the exposure for different background indices. This half-life is $5 \cdot 10^{25}$ years for the envisioned background index of 10^{-3} counts/(kg·keV·y) and an expected exposure of 100 kg·years.

The half-life is transformed into an effective Majorana neutrino mass using the same matrix elements as before. The mass for which 50% of the experiments would report a discovery is shown in Figure 4.5 (right) as a function of the exposure and for different background conditions. For an exposure of 100 kg·years and a background index of 10^{-3} counts/(kg·keV·y) neutrinoless double beta-decay could be discovered for an effective Majorana neutrino mass of 350 meV (with a 50% probability).

The results of the sensitivity study are summarized in Table 4.1 (limits) and Table 4.2 (discovery potential).

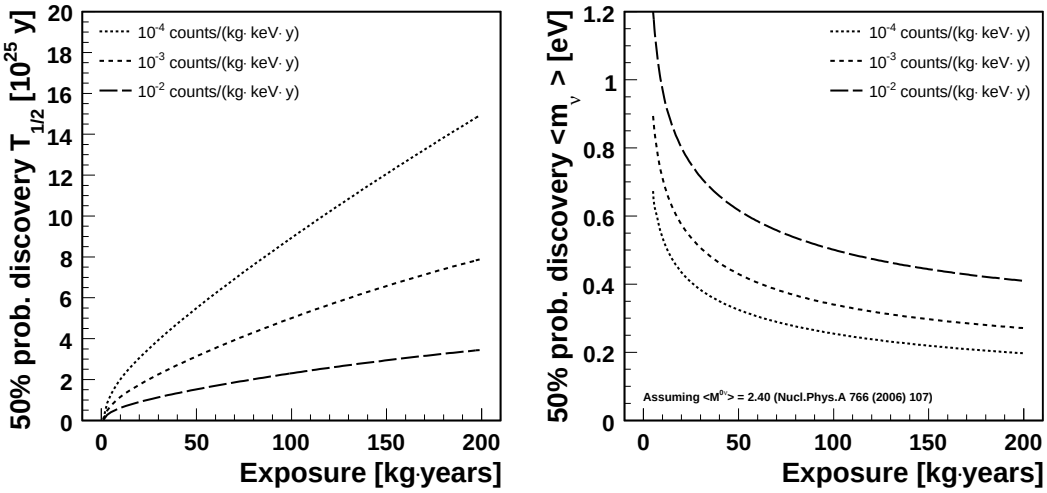

Figure 4.5: Left: the half-life for which 50% of the experiments would report a discovery is plotted versus the exposure for different background conditions. Right: the effective Majorana neutrino mass for which 50% of the experiments would report a discovery versus the exposure. The mass was determined from the half-life using the matrix element reported in [81].

Table 4.1: Expected lower limits of the half-life and upper limits for the effective Majorana neutrino mass for different background scenarios.

Exposure [kg·y]	Background index [counts/(kg·keV·y)]	$T_{1/2}^{0\nu\beta\beta}$ limit (90% prob.) [y]	$\langle m_\nu \rangle$ limit (90% prob.) [meV]
100	10^{-2}	$6.0 \cdot 10^{25}$	300
100	10^{-3}	$13.5 \cdot 10^{25}$	200
100	10^{-4}	$18.5 \cdot 10^{25}$	180

Table 4.2: Half-life and effective Majorana neutrino mass for different background scenarios for which a discovery would be claimed with a probability of 50%.

Exposure [kg·y]	Background index [counts/(kg·keV·y)]	$T_{1/2}^{0\nu\beta\beta}$ (50% prob.) [y]	$\langle m_\nu \rangle$ (50% prob.) [meV]
100	10^{-2}	$2.2 \cdot 10^{25}$	500
100	10^{-3}	$5.0 \cdot 10^{25}$	350
100	10^{-4}	$9.0 \cdot 10^{25}$	250

4.3.4 Influence of the prior probabilities

The influence of the prior probabilities on the outcome of the sensitivity calculation is studied by varying the prior probability of the number of expected signal events, $p_0(S)$. Three different prior probabilities are studied:

- a flat prior: $p_0(S) \propto const.$,
- a pessimistic prior: $p_0(S) \propto e^{-S/10}$,
- a peaking prior: $p_0(S) \propto e^{1-\tilde{S}/S}/S^2$,

where $\tilde{S}$ is the number of events corresponding to a half-life of $1.2 \cdot 10^{25}$ years. For all three prior probabilities $S < S_{\max}$ is required. For a background index of 10^{-3} counts/(kg·keV·y) and an exposure of 100 kg·years the limit strongly depends on the chosen prior. The limit on the half-life for the pessimistic prior probability is about 10% higher than for the flat prior probability. In comparison, the peaking prior gives a 50% lower limit compared to the flat prior. This study makes the role of priors clear. If an opinion is initially strongly held, then substantial data is needed to change it. In the scientific context, consensus priors should be strived for.

4.3.5 Studies on the stability of the method

The stability of the analysis method is studied and the results are listed here for completeness. The average probability $p(H_1|\text{data})$ is used to quantify the stability.

- Shape of the background spectrum: The generated background distribution was tilted so that the background changes by a factor of 2 over the region of interest. No significant difference in $\langle p(H_1|\text{data})\rangle$ was found.
- Additional peaks: An additional peak with an amplitude equal to the signal peak was placed 10 keV below the $Q_{\beta\beta}$-value. No significant difference in $\langle p(H_1|\text{data})\rangle$ was found.
- Energy resolution: The energy resolution was varied between 1 keV and 14 keV. The average probability $p(H_1|\text{data})$ decreases with improving resolution as expected.
- Miscalibration: The signal peak was shifted by up to 10 keV in the energy spectrum. The average probability $p(H_1|\text{data})$ was found to be sensitive to the variation. The accuracy of the calibration required to avoid a degradation of the sensitivity is of the order of a few percent of the energy resolution.

Chapter 5

Germanium detectors

The operating principle of germanium detectors is presented in the following sections. First, the interactions of electrons, positrons and photons in the relevant energy region up to several MeV are discussed. The general properties of germanium diodes and the signal development are introduced including the rather novel technique of segmentation. The chapter closes with a short summary of signal amplification and data acquisition. For a general overview of the properties of germanium detectors, see e.g., [82].

5.1 Interactions of electrons, positrons and photons with matter

5.1.1 Electrons and positrons

Electrons and positrons with sub-GeV-energies traversing matter lose their kinetic energy mainly by two different interaction processes, namely ionization and bremsstrahlung. Ionization has the larger cross-section for lower energies while bremsstrahlung is the dominant interaction process for higher energies. The critical energy, $E_{\text{crit.}}$, for which the average energy loss due to the two processes is equal depends on the material the particles traverse. For elements with $Z > 13$ the critical energy is [83]

$$E_{\text{crit.}} = \frac{550 \text{ MeV}}{Z} \,. \tag{5.1}$$

Unlike electrons, positrons at rest annihilate with electrons into two photons with energies of 511 keV each, corresponding to the rest mass of an electron.

Ionization: Incident electrons or positrons can scatter off electrons in the shell of an atom and cause those secondary electrons to leave the shell and thus ionize the atom. The average energy loss of electrons and positrons due to ionization is approximately [1] [86]

$$-\left\langle \frac{dE}{dx} \right\rangle = 4\pi N_{\mathrm{A}} r_{\mathrm{e}}^2 m_{\mathrm{e}} c^2 \frac{Z}{A} \cdot \frac{1}{\beta^2} \cdot \left[\ln\left(\frac{\gamma m_{\mathrm{e}} c^2}{2I} \right) - \beta^2 - \frac{\delta^*}{2} \right] , \tag{5.2}$$

where

N_{A}	:	Avogadro's constant,
r_{e}	:	classical electron radius,
m_{e}	:	mass of the electron,
Z, A	:	atomic charge and mass of the absorber,
β	:	velocity of the electron,
I	:	material specific constant of absorber ,
δ^*	:	parameter which describes the screening of the transverse electrical field of the electron by the charge density of the electrons in the absorber material (density effect).

Bremsstrahlung: In the electric field of a nucleus electrons and positrons can lose kinetic energy by the emission of *bremsstrahlung* photons. The average energy loss due to bremsstrahlung for an electron is [86]

$$-\left\langle \frac{dE}{dx} \right\rangle = 4\alpha N_{\mathrm{A}} \frac{Z^2}{A} r_{\mathrm{e}}^2 \cdot E \cdot \ln \frac{183}{Z^{1/3}} , \tag{5.3}$$

where α is the fine-structure constant and E is the energy of the electron or positron.

The range of an electron or positron depends on its energy and the material. For a 1 MeV electron the average range in germanium is approximately 1 mm [87].

5.1.2 Photons

Photons can interact with matter through three different processes. The cross-section depends on the atomic charge Z of the material and the photon energy, E_γ. For photon energies below about 200 keV the photo effect is the dominant process of energy loss in germanium. In the energy region from about 200 keV up to about 8 MeV photons mostly interact via Compton scattering. For higher energies photons can create electron-positron pairs in the electric field of a nucleus. In all three cases at least one electron is present in the final state. The electrons (and positron) will subsequently interact with matter via the discussed mechanisms.

[1] The average energy loss is calculated using the Bethe-Bloch formula [84, 85] for the mass and charge of an electron.

Photo effect: The photon energy can be absorbed completely by an atomic shell electron which is kicked out of the shell (photo effect). The kinetic energy of this secondary electron, E_e, is given by

$$E_e = E_\gamma - E_\mathrm{b}\,, \tag{5.4}$$

where E_b is the binding energy of the electron. If the photo effect occurs in the inner shell of an atom, outer shell electrons will fill the vacancy in the inner shell. Due to the difference in binding energies, either characteristic x-rays are emitted or, in case the x-ray photon is re-absorbed, secondary Auger-electrons are emitted. The photo effect cross-section, σ_photo, is inversely proportional to the photon energy.

Compton scattering: The elastic scattering of photons off electrons is referred to as Compton scattering and described by the Klein-Nishina relation. The photon will transfer energy to the scattered electron where the maximum energy transfer occurs at a scattering angle of 180°. The Compton scattering cross-section, σ_Compton, is proportional to $\ln E_\gamma / E_\gamma$.

Pair creation: If the photon energy exceeds twice the rest mass of an electron, the photon can create an electron-positron pair in the electric field of a nucleus. For low energies the pair production cross-section, σ_pair, is proportional to $\ln E_\gamma$ and it saturates for larger energies ($E_\gamma \gg \frac{1}{\alpha Z^{1/3}}$). The positron will scatter until it has lost all of its kinetic energy and will subsequently annihilate with an electron into two 511 keV photons.

Figure 5.1 shows the mass attenuation coefficient $\mu = \frac{N_\mathrm{A}}{A} \cdot (\sigma_\mathrm{photo} + \sigma_\mathrm{Compton} + \sigma_\mathrm{pair})$ for the interaction of photons with germanium as a function of the photon energy.

In germanium, a 1 MeV photon has a range of the order of centimeters.

5.2 Semiconductor (germanium) detectors

A variety of literature is available in which the working principle of semiconductor detectors is described. For an overview see e.g., [82] and references therein.

5.2.1 Working principle

Materials are classified as insulators, semiconductors and conductors according to the energy gap between the valence and the conduction band. For a semiconductor this *band gap* is of the order of 1 eV. The properties of a semiconductor are defined by their impurities, also called dopants: elements with three valence electrons (e.g., boron) act as acceptors whereas elements with five valence electrons (e.g., phosphorus or lithium) act as donors.

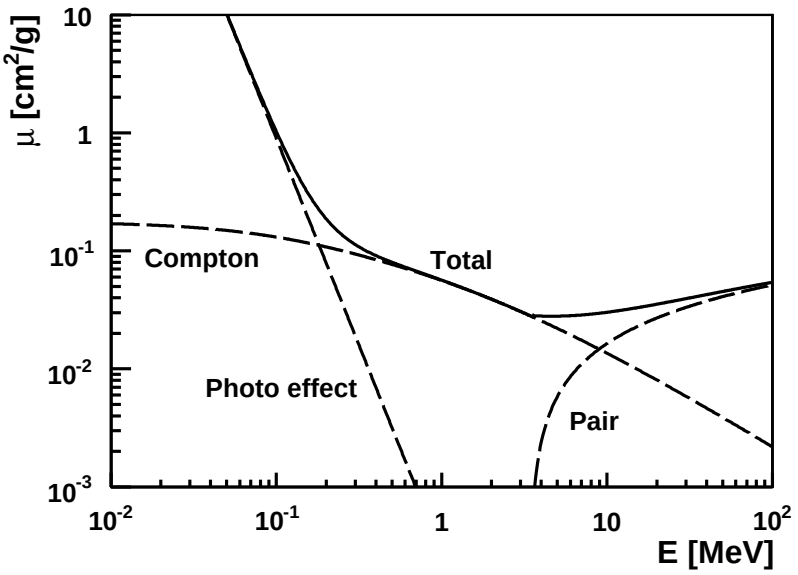

Figure 5.1: Mass attenuation coefficient μ in germanium as a function of the photon energy. For energies below 200 keV the photo effect dominates, while in the region from 200 keV to 8 MeV Compton scattering is the pre-dominant process of energy loss. For higher energies pair creation dominates.

The acceptor levels lie about 0.05 eV above the valence band, the donor levels lie about 0.05 eV below the lower edge of the conduction band. Only a very small amount of energy is needed to lift electrons from the valence band into the acceptor level and thus create a net positive charge in the valence band (p-type). Similarly, only a small amount of energy is needed to lift electrons from the donator level to the conduction band creating a net negative charge in the conduction band (n-type).

A semiconductor detector is composed of a p-n-junction. Close to the junction electrons from the n-type region will diffuse into the p-type region and recombine. The resulting *depletion zone* is non-conducting. The size of the depletion region is increased by applying an external potential to the contacts (or *electrodes*) of the p- and n-type regions. If the anode is connected to the n-side and the cathode connected to the p-side, electrons and holes diffuse away from the junction. This mode of operation is referred to as *reverse biasing*. For most detector applications the voltage is chosen larger than the voltage needed to fully deplete the detector (*depletion voltage*).

Semiconductor detectors are produced in two types, characterized by the remaining impurities in the bulk material after the crystal pulling process. If the impurities are acceptors, e.g., boron, the bulk material is called p-type. The material is called n-type, if donors, e.g., lithium, dominate the material.

The p-n-junction of p-type germanium detectors is traditionally produced by drifting lithium into the surface of one side. This creates a layer of highly n-doped material with a thickness of the order of several hundred micrometers. In n-type detectors the p-n-junction is generally produced by the implantation of boron. This creates a layer of highly p-doped material with a thickness of the order of tenth of a micrometer.

The active volume, to first order the volume between the inner and outer contacts, is decreased by the thicknesses of the contacts which form *dead layers*. The thicknesses of the dead layers define the sensitivity of the detector to soft γ-radiation as low energy photons are attenuated or even absorbed in the dead layers.

5.2.2 Germanium semiconductor detectors

Germanium can be purified to a high degree - the number of electrically active impurities achievable in germanium crystals is of the order of $10^{10}/\mathrm{cm}^3$. This allows the construction of large individual detectors. The depletion depth is proportional to the square root of the ratio of the applied voltage and the dopant concentration. As the applied voltage can only be increased up to several kilovolt (depending on the size and geometry of the detector), the depletion depth can extend to several centimeters. This allows the construction of large detectors.

The size of crystals is limited by the strict requirements on the electrical properties of the crystal. The largest detectors are based on a cylindrical geometry with diameter and height both in the several centimeter range. In the following only cylindrical detectors are discussed.

Two geometries are distinguished: the *true coaxial* and the *closed-ended coaxial*. In both cases the shape is cylindrical with an inner bore. For true coaxial detectors the core is completely removed, whereas for a closed-ended coaxial geometry the core is only partially removed leaving a *cap* on one side. The latter geometry is commonly used in nuclear experiments for the detection of photons in the MeV-energy region.

5.2.3 Electric fields

The electric field inside a detector determines the velocity and direction of the charge carriers. It can be calculated by solving Poisson's equation. This is done in cylindrical coordinates

$$\frac{d^2\phi}{dr^2} + \frac{1}{r}\frac{d\phi}{dr} = -\frac{\rho}{\epsilon}\,. \tag{5.5}$$

ϕ is the electric potential and ρ is the charge density defined by the effective number of impurities. ϵ is the dielectric constant.

Figure 5.2 shows the electric field inside a detector as a function of the radius for different applied bias voltages. The assumed impurity concentration is $0.5 \cdot 10^{10}$ atoms/cm^3. A true coaxial geometry is assumed. The inner and outer radii of the diode, r_{i} and r_{o}, are 5 mm and 40 mm, respectively. A bias voltage of 2.2 kV is needed to fully deplete the detector. In the example, the impurity density is assumed to be constant throughout the detector. In real detectors, the impurity density usually varies by up to a factor of two across and a factor of three from top to bottom. As a result the depletion voltage changes with the height and the azimuthal angle.

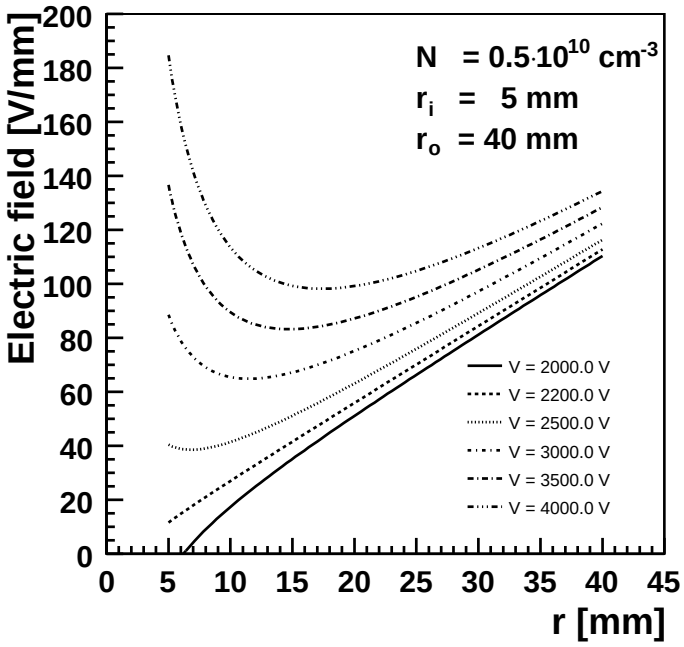

Figure 5.2: Electric field inside a detector as described in the text for different bias voltages. A minimum of about 2.2 kV is needed to fully deplete the detector. The junction is placed close to the outer surface of the crystal.

5.3 Signal development in (germanium) detectors

In the following, the signal development in germanium detectors is discussed. The influence of the crystal structure on the signal development is commented on.

Electrons, positrons and photons traversing a semiconductor detector deposit their energy via the interactions described in Section 5.1. The secondary electrons cause excitations of electrons from the valence band to the conduction band and thus create electron-hole pairs. A fraction of the deposited energy causes the excitation of phonons. Thus, the energy to create one electron-hole pair, E_{pair}, is composed of the band gap energy, E_{gap},

and the fraction of energy which causes phonon excitation. The band gap in germanium is $E_{\text{gap}} = 0.72$ eV whereas the pair energy is about four times larger with $E_{\text{pair}} = 2.95$ eV at 80 K. In comparison, the energy needed to create one electron-hole pair in silicon is about $E_{\text{pair}} = 3.72$ eV at 80 K. This energy does not depend on the type of incident particle or on its energy. The average number of electron-hole pairs, $\langle N \rangle$, for a given energy deposited, E_{dep}, is therefore

$$\langle N \rangle = E_{\text{dep}} / E_{\text{pair}} \ . \tag{5.6}$$

In reserve bias operation the electrons and holes drift towards the electrodes in opposite directions due to the applied electric field, $\mathcal{E}$. The drift velocities of the charge carriers is proportional to the electric field over a certain range

$$\begin{aligned} v_{e^-} &= \mu_{e^-} \cdot \mathcal{E} \quad , \ \mathcal{E} \leq \mathcal{E}_{\text{sat}} \\ &= v_{e^-}^{\text{sat}} \quad , \ \mathcal{E} > \mathcal{E}_{\text{sat}} \end{aligned} \tag{5.7}$$

$$\begin{aligned} v_h &= \mu_h \cdot \mathcal{E} \quad , \ \mathcal{E} \leq \mathcal{E}_{\text{sat}} \\ &= v_h^{\text{sat}} \quad , \ \mathcal{E} > \mathcal{E}_{\text{sat}} \end{aligned} \tag{5.8}$$

where v_{e^-} and v_h are the drift velocities of the electrons and holes, respectively. The proportionality factors μ_{e^-} and μ_h are referred to as mobilities and can be different by a factor of 2-3 for electrons and holes, depending on the semiconductor. The saturation field strength $\mathcal{E}_{\text{sat}}$ is of the order of 100 V/mm for germanium. The terminal velocity is about 10^8 mm/s. The drift direction is anti-parallel or parallel to the electric field lines for electrons and holes, respectively [2].

The moving charge carriers induce mirror charges in the electrodes of the detector. These can be amplified and read out. The functional form describing the integrated charge as a function of time is referred to as the *pulse shape*. For a cylindrical germanium detector with a diameter of 8 cm the typical time until the electrons and holes reach the electrodes, the risetime of the signal, is of the order of 400 ns. An example for the development of a signal is given in Section 5.5 where segmented detectors are discussed.

5.3.1 Crystal axes

The electrical conductivity of germanium is anisotropic in strong electric fields [88–91]. Hence, the drift direction of the charge carriers not only depends on the direction of the electric field but also on the orientation of the crystal axes. The angle between the drift direction and the electric field is known as the Sasaki angle [92] and in general differs from zero (Sasaki effect). Several phenomenological models exist which describe the transport properties of electrons (see [93] and references therein) in germanium. Models for the transport properties of holes have only recently being developed [94].

The deviation of the direction of charge carriers from the direction of the electric field can cause variations in the drift times. This effect is of the order of 5–20% and is observed experimentally (see Chapter 11).

[2] The crystal lattice can cause deviations in the drift direction. This will be discussed later.

5.4 Germanium detector properties

5.4.1 Operation temperature

The band gap in germanium of $E_{\text{gap}} = 0.72$ eV is small compared to those of other semiconductor materials like silicon with $E_{\text{gap}} = 1.1$ eV. At room temperature electrons in the valence band can be excited into the conduction band by thermal energy alone. In this example the difference between the band gap energies of germanium and silicon causes a difference of a factor 1 000 in the population of electrons in the conduction band at room temperature and thus a much higher conductivity for germanium. The electric field applied would induce a current which would make the operation as a detector impossible. Germanium detectors are usually cooled with liquid nitrogen to suppress the thermal excitations which results in typical operation temperatures of the order of 77 K [3].

5.4.2 Energy resolution

The total energy resolution, W_T, the full width at half maximum (FWHM) of the peak under study, is composed of three terms:

$$W_T^2 = W_D^2 + W_X^2 + W_E^2 \ . \tag{5.9}$$

W_D describes the statistical fluctuations of the creation of electron-hole pairs as

$$W_D^2 = 2.35^2 \cdot F \cdot \frac{E}{E_{\text{pair}}} \ , \tag{5.10}$$

where F is the Fano factor and of the order of 0.1. It accounts for the fact that the process of electron-hole pair creation is correlated with the excitation of phonons. The term W_X describes the effect of incomplete charge collection and scales linearly with the incident energy. The third term, W_E, is constant in energy and accounts for noise contributions from the amplifying electronics.

Germanium has a smaller E_{pair} than silicon. Thus, the relative statistical fluctuation of the number of electron-hole pairs created is smaller for germanium. Germanium detectors have a better energy resolution for small detector geometries in which the term W_D dominates. Typically, germanium detectors have an energy resolution of about 2 keV at 1.3 MeV, where the energy resolution of large detectors is dominated by the charge collection efficiency.

5.5 Segmented germanium detectors

A rather novel technique is the segmentation of cylindrical germanium detectors. Segmentation is done in the azimuthal angle ϕ and the height z. The technique used in the

[3] Germanium detectors are cooled via a cooling stick in most applications. Due to losses from imperfect heat conduction the temperature of the germanium crystal is slightly higher than that of the cooling medium.

fabrication of segmented detectors depends on the bulk-type. For p-type detectors the outer surface is milled. The fringe depths and thicknesses of the segments are of the order of a millimeter in order to penetrate the lithium-drifted n-layer. For n-type detectors photo-lithographic techniques are used to form the segments on the outer surface. Distortions in the electric field are expected for the former segmentation technique.

In segmented detectors core and segment electrodes are read out simultaneously. Ramo's Theorem [95] can be used to calculate the charge induced in each segment. If energy is deposited inside a segment (or rather in the volume spanned by $\Delta r \times \Delta\phi \times \Delta z$, where Δr is the difference of the outer and inner radius, $\Delta\phi$ and Δz are the segment sizes), the created charge carriers drift towards the core and segment electrodes. The charges induced on the electrodes are integrated by charge-sensitive pre-amplifiers. A neighboring segment inside which no energy was deposited also sees charges induced which will vanish once both types of charge carriers have reached the electrodes. Figure 5.3 (right) shows the pulse shape of two simulated events with different energy depositions: (1) energy is deposited inside the segment under study, (2) energy is deposited inside the neighboring segment. Details of the simulation are described in [96]. The underlying fields, so-called weighting fields, are used to calculate the induced charges. Figure 5.3 (left) show the weighting field for the segment under study. Simulations of the development of pulse shapes in germanium detectors have been performed previously for a variety of physics applications [93, 96, 97].

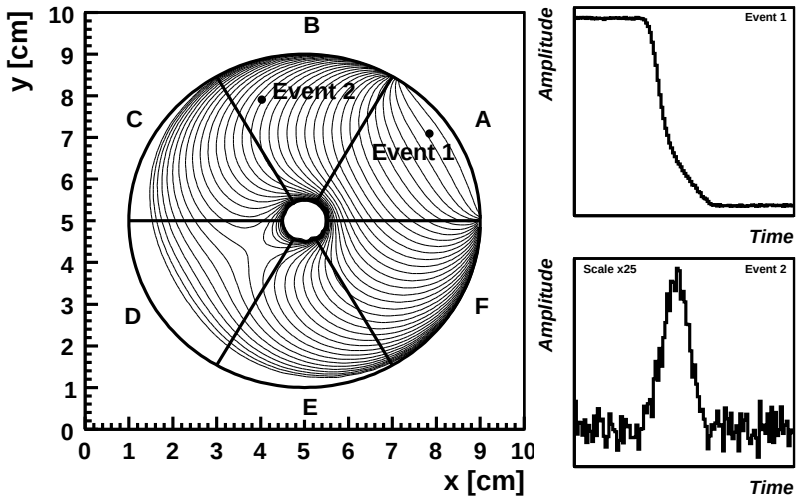

Figure 5.3: Left: Weighting field for segment A and position of the energy deposition for two events. Right: Pulse shape taken with segment A for the two events.

5.6 Signal amplification and read out

The induced charges on the electrodes of a germanium detector are usually too small to be handled by digitizing electronics. The corresponding pulse heights are of $\mathcal{O}(1\ \mu\text{V})$. Pulses are therefore pre-amplified to amplitudes of $\mathcal{O}(1\ \text{V})$. Charge-sensitive pre-amplifiers have an output pulse with an amplitude proportional to the integrated charge induced on the electrode, if the decay time of the generated pulse is much larger than the charge collection time. Typical decay times are of the order of 50-100 μs whereas collection times of the order of several hundred ns are typical for the germanium detectors discussed earlier. Ideally, the pre-amplifier does not contribute to the risetime of the pulse. A realistic pre-amplifier has a finite bandwidth. This results in a broadening of the pulses which can be modeled by a *transfer function*. It is typically described by a Gaussian with a width of the order of 20 ns. The pre-amplifier pulse is digitized with a frequency suitable to determine the structure of the rise of the pulse caused by the finite charge collection time.

Chapter 6

Signatures of physics processes and background rejection

As discussed in Chapter 4 the sensitivity of experiments built to search for $0\nu\beta\beta$-decay is strongly influenced by the amount of background observed. This chapter introduces the physics processes and sources of background encountered in germanium double beta decay-experiments. The signatures of signal and background events are discussed. Background rejection techniques developed for the GERDA experiment are summarized at the end of the chapter. A focus is placed on the distinction between electron and photon induced events.

6.1 Signal process and signature

The $0\nu\beta\beta$-decay process was introduced in detail in Chapter 2. The signature of the process is discussed here for the germanium isotope ^{76}Ge. The final state, in addition to the daughter nucleus, comprises of two electrons and has no neutrinos. The sum of the kinetic energies of the electrons is therefore approximately equal to $Q_{\beta\beta} = 2\,039$ keV (neglecting the recoil energy of the daughter nucleus). The range of electrons in the MeV-energy region is of the order of millimeters (see Section 5.1). Since the germanium detectors under consideration have a volume of the order of 400 cm^3, the energy of the electrons is most likely fully contained within a small volume of the crystal, if no hard bremsstrahlung occurs. The signature of $0\nu\beta\beta$-decay events is thus an energy deposit of about 2 039 keV in a small volume of one detector.

6.2 Background sources

Other processes can also cause an energy deposit of about 2 MeV inside a detector and can thus mimic the $0\nu\beta\beta$-decay process. These are referred to as background processes in the following.

Two types of background sources are distinguished. These are (1) the products of the decay of radioactive isotopes and (2) muon induced neutrons and electromagnetic cascades. The latter are discussed elsewhere [98], as is the overall neutron flux from radioactive elements in the surrounding bed-rock. The former one is the subject of this thesis.

All radioactive isotopes with Q-values larger than $Q_{\beta\beta}$ are potential sources of background. A fraction of the released energy can be deposited inside a detector by electrons, photons or α-particles such that the measured energy is around 2 MeV. Photons in the MeV-energy range are particularly dangerous. They predominantly deposit their energy via Compton scattering and have a range of the order of centimeters. Considering the size of the germanium crystals under study, processes with photons in the final state are likely to deposit only a fraction of their total energy inside a detector. Background contributions from the decay of radioactive isotopes are categorized according to their origin: internal background sources are those located inside the germanium, external background sources are radioactive isotopes in the vicinity of the detectors.

6.2.1 Internal background sources

Germanium detectors are exposed to cosmic radiation, if produced or stored above ground. Hadronic interactions can cause spallation of germanium nuclei and thus the production of radioactive isotopes inside the detector volume. This process is termed cosmogenic activation. Recent calculations and measurements of the rate of this activation show a reasonable agreement [99]. Two cosmogenically produced isotopes, ^{60}Co and ^{68}Ge, have Q-values above $Q_{\beta\beta}$ and are therefore potential sources of background.

^{60}Co decays via β^--decay into ^{60}Ni under the emission of a 318 keV electron and two photons with energies of 1 173.2 keV and 1 332.5 keV. The Q-value of the decay is $Q = 2\,823.9$ keV. The calculated production rate for ^{60}Co in enriched germanium detectors is 3.3 atoms/(kg·d) [100]; the half-life of the decay is $T_{1/2} = 5.3$ y.

^{68}Ge decays via β^+-decay into ^{68}Ga which subsequently decays under the emission of a positron and additional photons from the annihilation of the positron. The decay of ^{68}Ga has a Q-value of 2 921.1 keV. The calculated production rate in enriched germanium detectors is 5.6 atoms/(kg·d) [100]. The half-life of the decay of ^{68}Ge is 271 d.

6.2.2 External background sources

The natural decay chains of ^{232}Th and ^{238}U contain the decays of ^{208}Tl$\rightarrow^{208}$Pb and ^{214}Bi$\rightarrow^{214}$Po which have Q-values of 5 001.0 keV and 3 272.0 keV, respectively, and are thus potential sources of background. In particular, a single 2 615 keV photon is emitted with a high probability in the de-excitation of ^{208}Pb. As small amounts of ^{232}Th and ^{238}U are present in almost all high-Z materials used in the experimental setup, these background sources influence the design and shielding of the experiment considerably.

The ^{238}U daughter ^{210}Pb decays into ^{210}Bi which subsequently decays via α-decay. A contamination of the detector surface with ^{210}Pb introduces potential contributions to the background. If the detector has a non charge sensitive (dead) surface layer, only part of the energy lost by the α-particle is detected. Depending on the thickness of the dead layer this can result in a signal close to the region of interest. Evidence for surface contaminations of germanium detectors was found in previous experiments [101].

6.3 Classification of signal and background signatures

The signatures of the signal and the main background processes are classified according to the particles in the final state:

- Class I: Two electrons. This class encompasses the neutrinoless and neutrino accompanied double beta-decay processes. If the energy resolution is better than about 10 keV, the two modes of double beta-decay can be separated, since the energy region around the $Q_{\beta\beta}$-value is hardly populated by events from the $2\nu\beta\beta$-decay process. The two electrons deposit their energy locally, i.e., on a millimeter scale.

- Class II: Photon(s) and electron. This class contains all β^--decay processes accompanied by the emission of one or more photons which occur inside the detector or close to its surface. The energy of the electron is deposited locally, whereas the photon scatters and not all of its energy is necessarily deposited inside the detector. An example for this class is the decay of ^{60}Co inside the germanium.

- Class III: Photon(s) and positron. Similar to Class II, this class contains all β^+-decay processes accompanied by the emission of one or more photons inside the detector. The positron deposits most of its energy locally and annihilates. The photons (the two 511 keV gammas plus any additional photons) scatter and mostly do not deposit all of their energy inside one detector. The most prominent example for this class is the decay of ^{68}Ge inside the germanium.

- Class IV: Photon(s) only. If the decay occurs outside the germanium detectors, α-particles or electrons/positrons are normally stopped before they reach the crystals. Most prominent examples are the decays of ^{208}Tl and ^{214}Bi which come from radio-impurities in the surrounding of the detectors.

- Class V: α-particles. Surface contamination with ^{210}Pb or other isotopes which decay via α-emission can contribute to the background. α-particles in the 2–10 MeV-energy range deposit their energy on a 5–50 μm scale. α-particles emitted at the surface therefore potentially deposit only a fraction of their initial energy inside the active volume of the detector.

The spatial distribution over which energy is deposited inside a detector is the key to most of the background rejection techniques introduced in the following. A second classification scheme is therefore introduced. Two types of events are distinguished:

- *Single-site events* (SSE): This class contains all events in which energy is deposited on a scale of about one millimeter or below [1]. Three different types of events contribute to this class: (a) Class I and V events in which no hard bremsstrahlung processes are present; (b) events with photons in the final state in which the photon only scatters once inside the detector volume; (c) *double escape* events in which a photon produces an electron-positron pair and both photons from the subsequent annihilation of the positron escape.

- *Multi-site events* (MSE): This class contains all events in which energy is deposited on a scale larger than about one millimeter. Compton-scattered photons are likely to deposit energy at multiple sites. Thus, a large fraction of Class II–IV events contribute to this class. Events from Class I can also contribute if an electron emits a hard bremsstrahlung photon.

6.4 Background rejection techniques

Several background rejection techniques are developed and implemented in the design of GERDA:

- Anti-coincidence between events: In the decay of ^{68}Ge an x-ray of 10 keV is released before the subsequent decay of ^{68}Ga which has a half-life of $T_{1/2} = 68$ min. Events following a detected x-ray of that energy can therefore be vetoed in a time window compatible with the half-life of ^{68}Ga. A low detection threshold is required in order to apply this technique. Feasibility studies are currently carried out.

- Anti-coincidence between detectors: Compton-scattered photons are likely to deposit energy in more than one detector while $0\nu\beta\beta$-decay electrons will predominantly deposit energy in only one detector. Photons can thus be identified by requiring more than one detector to see energy above the threshold. For an evaluation of the potential to distinguish between electron induced and photon induced events with this method, see the results of a Monte Carlo study presented in Chapter 7 and in [68].

- Anti-coincidence between segments: Considering the segmented detectors foreseen for Phase II photons can, with the same argument as for the detector anti-coincidence, be identified by requiring more than one segment to show energy. An evaluation of the potential to distinguish between electron induced and photon induced events with this method is presented in Chapter 7 and in [68]. A study using data from a GERDA Phase II prototype detector is presented in Chapter 11 and in [69].

- Pulse shape analysis: Photons and electrons can be distinguished by analyzing the time structure of the detector response. For details see Chapter 8 or [96]. A study using data from a GERDA Phase II prototype detector is presented in Chapter 11 and in [102].

[1] A quantitative classification criterion for single-site events is derived in Chapter 8.

- Instrumentation of the cryostat: Liquid argon scintillates if energy is deposited inside the argon volume. The scintillation light can be detected by photomultipliers mounted on the walls of the cryostat. Events with photons in the final state which deposit only a fraction of their energy inside the germanium detectors can be vetoed by requiring an anti-coincidence between the observed scintillation light and the energy deposit inside the detectors. This technique is not part of the GERDA baseline design. Feasibility studies are currently being performed [70, 72].

The distinction between electrons and photons using segmented detectors and the analysis of the time structure of the detector response are focused on in this thesis. These techniques are investigated for the GERDA experiment and applied to data taken with a GERDA Phase II prototype detector. Monte Carlo studies provide an estimate of the background rejection. The prototype data is compared to Monte Carlo predictions in order to verify the simulations.

Chapter 7

Background rejection using segmented detectors - a Monte Carlo study

Segmented germanium detectors can be used to reject photons by requiring anti-coincidences between the segments of a detector. This technique is well established in experiments such as AGATA [103] and GRETA [97] and provides a basis for γ-ray tracking [104].

In the following, the results of a Monte Carlo study are presented. First, the Monte Carlo framework is introduced. An idealized Phase II setup is simulated. The spatial distribution over which energy is deposited inside the germanium detectors by isotopes from the different classes introduced in Chapter 6 is discussed. The rejection power for those isotopes using anti-coincidence requirements between crystals and between segments is presented.

7.1 MaGe - the GERDA Monte Carlo framework

Monte Carlo studies of the GERDA setup and the physics processes encountered in the experiment are performed in order to (1) estimate the background index expected for the experiment, (2) support the design of detector components and (3) support R&D projects by simulating individual setups. The simulation is performed using the MaGe package, a GEANT4 [105] based tool which simulates the GERDA geometry and all relevant physics processes. Emphasis was placed on low energy interactions and hadronic interactions resulting from cosmic ray spallation. The physics list is optimized for underground-physics applications [106]. A description of the implemented physics processes and models can be found in [107]. MaGe was developed in cooperation with the Majorana project to support both experiments. Details are described in [108]. A validation of the simulation is aimed at by comparing data from a variety of auxiliary experiments with Monte Carlo data. With a few exceptions the overall agreement is on the percent level and satisfactory.

7.1.1 Simulation of the GERDA geometry

A schematic of the simplified GERDA infrastructure and an idealized Phase II array of detectors as simulated are shown in Figure 7.1. The design and the geometry of GERDA were not fixed at the time of the simulation. The cryogenic liquid in the simulation is nitrogen as originally proposed [3]. Simulations with liquid argon as cooling medium are currently being performed.

An array of 21 identical detectors, placed hexagonally in strings of three detectors each, is assumed. The simulated detectors have a height of 8 cm, an inner diameter of 1 cm and an outer diameter of 8 cm. The detectors are segmented into 6 ϕ- and 3 z-segments each. Unsegmented detectors are simulated by summing the energy deposits of all segments in one detector. The vertical distance between two crystals is 5 cm and the distance of closest approach between two strings is 2 cm. The crystal array is placed inside a three-walled copper cryostat with an outer radius of 2 m and a height of 5 m. The cryostat itself is surrounded by a water tank with a diameter of 10 m and a height of 8.90 m.

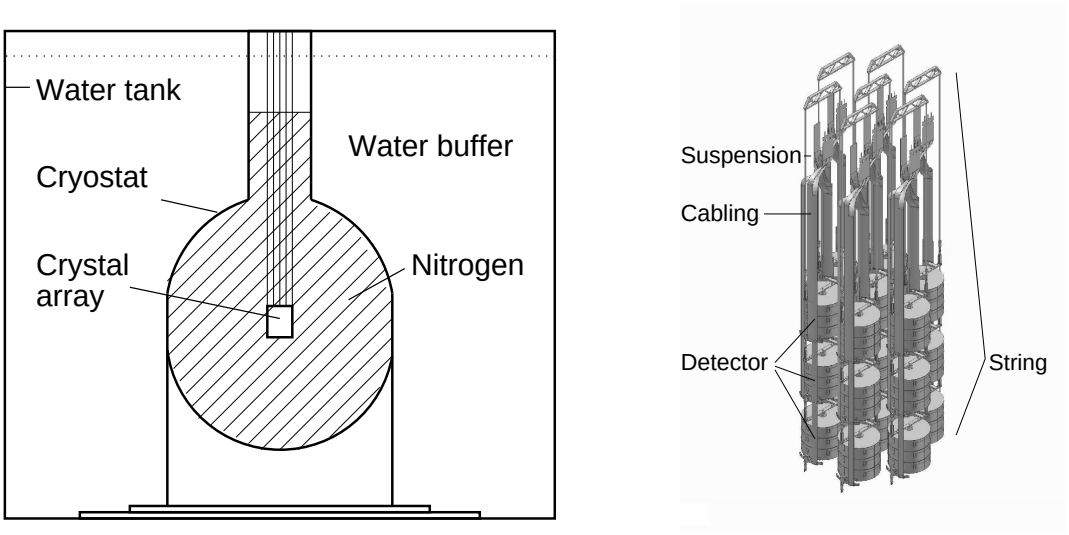

Figure 7.1: Schematic drawing of the GERDA geometry (left) and an idealized Phase II array of detectors (right) as simulated.

Events are simulated for the signal and background processes. Each unstable nucleus under consideration is placed randomly inside the geometrical component under study. Subsequently, the decay products are propagated through the GERDA geometry and the energy deposited inside the detectors is recorded.

An estimate of the expected background index from radioactive isotopes close to the detector is presented in Chapter 12. The muon induced background is discussed in [98]. Chapter 12 also summarizes the total background index anticipated for the idealized Phase II setup.

7.1.2 Simulation of test stands

Test stands are simulated making use of the flexibility provided by the MaGe tool. Among these are the Germanium Detector Lab facility at LNGS, low-background germanium detectors for screening experiments, several test stands operated in Munich and of those especially the setup for the first GERDA Phase II prototype detector. Details of this particular simulation can be found in Chapter 9 and in [69].

7.2 Selected background processes

The classes of signatures of the signal and background processes are listed in Section 6.3. Representative processes from each class are selected. Between 10^5 and 10^6 events are simulated for every background process and configuration. As decays inside the germanium crystals the $0\nu\beta\beta$-decay process (Class I), the decay of ^{60}Co (Class II) and the decay of ^{68}Ge (Class III) are studied. The decay of ^{208}Tl inside the detector holders serves as an example for Class IV. The decay of ^{210}Pb nuclei on the surface of the crystals is given as an example for Class V.

7.3 Spatial distribution of energy deposition

A measure of the spatial distribution of the energy deposition in an event is the radius R_{90} within which 90% of the total energy deposited is contained. To begin with, the center-of-energy-deposition is calculated for each event as:

$$\vec{x}_{\text{c.o.e.d.}} = \frac{\sum_i E_i \vec{x}_i}{\sum_i E_i}, \tag{7.1}$$

where the sum runs over all individual energy deposits in germanium. Afterwards, the energy deposits are ordered according to their distance to the center-of-energy-deposition. Summing over all energy deposits with increasing distance, R_{90} is defined as the distance of the particular energy deposit which is the first that satisfies the requirement that the sum of energies is larger than 90% of the total energy.

Figure 7.2 (top) shows the distributions of R_{90} for the processes considered without a cut on the total energy deposited. The distribution of the $0\nu\beta\beta$-decay process has a strong peak in the millimeter range. This reflects the range of the electrons in germanium at the relevant energy. The distribution ranges up to the centimeter scale due to events with hard bremsstrahlung in the final state. The distributions for Class II and III

processes show a peak at several centimeters. This is expected due to the range of the photons which undergo Compton scattering. The shoulder towards lower radii is due to photons which only deposit part of their energy in the crystal. A second, much smaller peak in the micrometer range is visible for Class II events. In this case, the photons escape the detector and only electrons deposit their energy in the crystal. The range for these electrons is smaller than for those in the $0\nu\beta\beta$-decay process due to their lower energy. The distribution for Class III events also shows a second peak, but smaller than for the Class II events and shifted towards higher radii. This is due to the 511 keV photons which deposit their energy over a larger volume than the electrons.

Since photons in Class IV events deposit only a fraction of their energy in the crystals, the range of energy deposition varies from the sub-micrometer to the centimeter range. Again, a smaller peak in the micrometer range is visible. It is due to electrons which come from decays of ^{208}Tl in the holder structure and are not stopped in the liquid nitrogen. The distribution for Class V events ranges from the micrometer to the centimeter scale. The sharp peak at 1 μm is an artifact of the simulation due to the threshold for the production and tracking of δ-rays[1]. The peak at around 10 μm is due to the range of α-particles in the relevant energy region. The distribution above 10 μm is due to δ-rays and bremsstrahlung photons.

Figure 7.2 (bottom) shows the distribution of R_{90} for Classes I to IV in the region from 0.1 mm to 10 cm. The total energy for the events in these distributions is required to be within a window of $\pm$50 keV around $Q_{\beta\beta}$. The difference in R_{90} for the signal process and the chosen background processes is more pronounced than in Figure 7.2 (top). Note the change in the x-scale. Similar calculations for a different setup [109] are compatible with the results obtained in this study.

As can be seen in Figure 7.2 the range of the photons involved in the processes under study is indeed approximately 2 - 3 cm. In the chosen segmentation scheme, considering the size of the crystals, the size of a single segment is comparable with a sphere of radius 1.4 cm. The simple considerations that led to the choice of the segmentation scheme are thus confirmed.

[1] A variation of threshold parameters did not have an effect on the simulation results presented in the following.

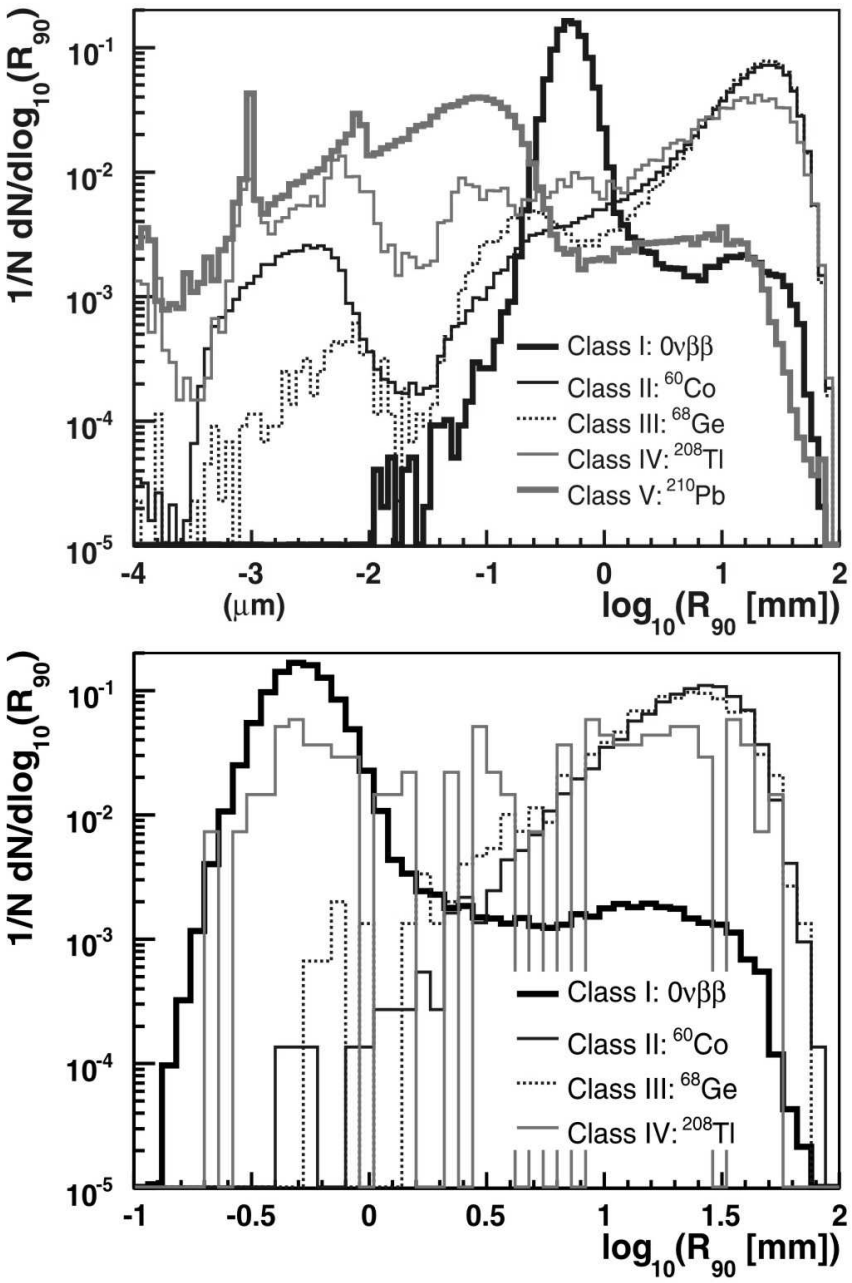

Figure 7.2: Distributions of the radii R_{90} containing 90% of the energy of the events. The thick black solid line represents $0\nu\beta\beta$ events, the other lines show distributions for selected background events, see inset. A cut on the total energy is either not applied (top) or applied (bottom). Note the change in the x-scale. Each distribution is normalized to unity.

7.4 Multiplicities and suppression factors

The *crystal multiplicity*, N_c, is defined as the number of crystals in an event which see energies larger than 10 keV. Similarly, the *segment multiplicity*, N_s, is defined as the number of segments in an event with energies larger than 10 keV. The segments do not necessarily have to belong to the same crystal. Distributions of the crystal/segment multiplicity for the processes selected in Section 7.2 are displayed in Figure 7.3 (left/right).

Events from all five classes predominantly show energy deposition in only one crystal. However, for Classes I and V the multiplicity drops faster than for Classes II to IV. The segment multiplicities for Classes II, III and IV drop off only beyond a multiplicity of three. Again, the multiplicities drop significantly faster for the classes without photon emission. The distributions behave as expected from the distributions of R_{90}. The segment multiplicities show that the segment size is large compared to the size of energy deposits from electrons in the signal process and comparable to the range of photons in background events.

The distributions of the energy deposited inside the detectors are shown in Figure 7.4 for the processes selected. For each process the total energy measured for all events (total energy spectrum) is shown as well as the spectrum of events after anti-coincidence cuts between crystals (single crystal spectrum, $N_c = 1$) and between segments (single segment spectrum, $N_s = 1$).

The top left histogram shows the energy distributions for the $0\nu\beta\beta$-decay process. Most of the events deposit energy at the $Q_{\beta\beta}$-value, although a tail towards lower energies is present due to bremsstrahlung. 87% of the signal events deposit their energy within a 10 keV window around $Q_{\beta\beta}$. Since the range of electrons is small compared to the size of the crystals and segments, anti-coincidence requirements change the energy spectrum only slightly. The shoulder close to the peak is reduced because soft bremsstrahlung photons interact in the crystal. The long tail is not affected, because the photons totally escape.

The top right histogram shows the spectra for intrinsic ^{60}Co. The two characteristic lines from the de-excitation of ^{60}Ni as well as the summation peak are visible in all three cases. The lines are broadened due to the additional electron that is emitted in the decay. The suppression is extremely large due to the presence of two photons.

The *number suppression factor*, SF_N, is defined as the ratio of the number of events which have a measured total energy in a 10 keV window around $Q_{\beta\beta}$ and the number of events which, in addition, fulfill the respective anti-coincidence requirement. This is either an anti-coincidence between crystals (SF_N^C) or between segments (SF_N^S).

The single crystal spectrum reflects a clear suppression of the process for ^{60}Co. The suppression factors for crystal and segment anti-coincidence are SF_N^C=3.2 and SF_N^S= 38.3, respectively.

The middle left histogram of Figure 7.4 shows the energy spectra for ^{68}Ge. As in the case of ^{60}Co the single crystal and single segment spectra are suppressed. The suppression factor is $SF_{\mathrm{N}}^{\mathrm{C}}$=2.4 for the single crystal spectrum and $SF_{\mathrm{N}}^{\mathrm{S}}$=18.0 for the single segment spectrum. In comparison to ^{60}Co the suppression is not as strong since only one photon is present in the final state of the decay of ^{68}Ge (^{68}Ga), and the probability of multiple energy deposits is therefore smaller.

The middle right histogram shows the energy spectra for ^{208}Tl in the copper of the detector holder. The suppression factor for the single crystal spectrum is $SF_{\mathrm{N}}^{\mathrm{C}}$=2.2. The single segment spectrum is further suppressed with a suppression factor of $SF_{\mathrm{N}}^{\mathrm{S}}$=4.6. This is due to multiple interactions in one crystal.

The spectra from the decay of ^{210}Pb on the surface of the detectors are shown in the bottom left histogram of Figure 7.4. As expected, the anti-coincidence requirements do not change the spectrum visibly since α-particles have a range which is small compared to the size of the detectors and the segments.

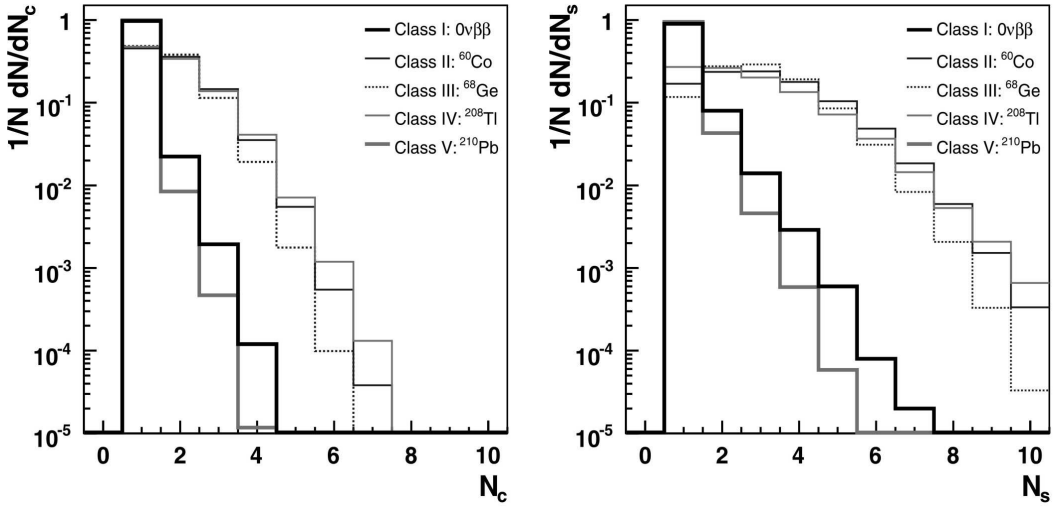

Figure 7.3: Distributions of crystal (left) and segment (right) multiplicities for the five selected processes.

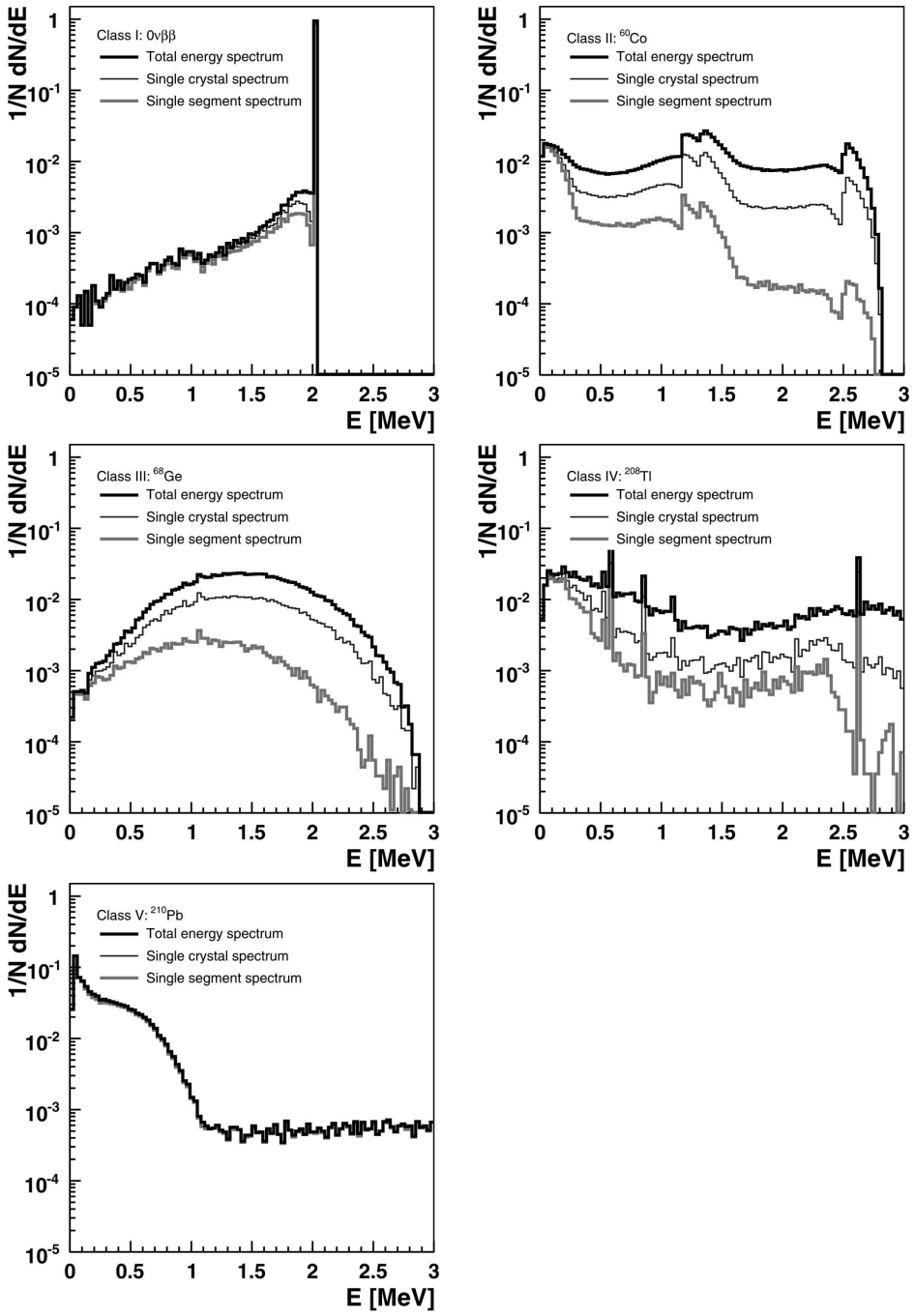

Figure 7.4: Energy spectra of the five selected processes (top left: $0\nu\beta\beta$, top right: ^{60}Co, middle left: ^{68}Ge, middle right: ^{208}Tl, bottom left: ^{210}Pb). The thick black solid line corresponds to the total energy in all crystals. The thin black line indicates the energy deposited in one crystal requiring only one crystal to fire ($N_c = 1$). The thick gray line is the spectrum of energy deposited in one segment requiring exactly one segment to fire ($N_s = 1$). The numerical values for the suppression factors can be found in Table 7.1.

In order to quantify the benefit of segmentation the simulation was carried out for the main sources of radioactive background expected in the GERDA experiment. The suppression factors achieved by anti-coincidence requirements between crystals and between segments were calculated for different isotopes located in different components. The results are summarized in Table 7.1. Note that the class of background an isotope belongs to also depends on its position.

Table 7.1: Summary of suppression factors for single crystal ($SF_{\mathrm{N}}^{\mathrm{C}}$) and single segment ($SF_{\mathrm{N}}^{\mathrm{S}}$) anti-coincidence requirements for a representative selection of isotopes. A detector unit consists of the crystal, a holder structure (copper and Teflon), Kapton cables and electronics. The electronics is placed about 30 cm above the detector array.

Material	Source	Class		$SF_{\mathrm{N}}^{\mathrm{C}}$	$SF_{\mathrm{N}}^{\mathrm{S}}$
Crystal					
Germanium	^{214}Bi	II	$(e^- + \gamma)$	1.8 ± 0.1	5.5 ± 0.3
	^{208}Tl	II	$(e^- + \gamma)$	2.6 ± 0.4	13.0 ± 3.7
	^{60}Co	II	$(e^- + \gamma)$	3.2 ± 0.1	38.3 ± 1.0
	^{68}Ge	III	$(e^+ + \gamma)$	2.4 ± 0.1	18.0 ± 1.4
Surface	^{210}Pb	V	(α)	$1.0^{+0.4}_{-0}$	$1.0^{+0.4}_{-0}$
Detector holder					
Copper	^{214}Bi	IV	(γ)	2.8 ± 0.5	6.0 ± 1.4
	^{208}Tl	IV	(γ)	2.2 ± 0.4	4.6 ± 0.9
	^{60}Co	IV	(γ)	6.7 ± 0.2	157.2 ± 26.7
Teflon	^{214}Bi	IV	(γ)	2.2 ± 0.3	12.8 ± 3.7
	^{208}Tl	IV	(γ)	2.5 ± 0.3	10.0 ± 2.1
	^{60}Co	IV	(γ)	3.8 ± 0.1	106.3 ± 7.6
Cables					
Copper	^{214}Bi	IV (II)	(γ)	3.3 ± 0.5	7.4 ± 1.3
	^{208}Tl	IV (II)	(γ)	3.1 ± 0.7	4.7 ± 1.2
Kapton	^{214}Bi	IV (II)	(γ)	3.3 ± 0.5	7.4 ± 1.3
	^{208}Tl	IV (II)	(γ)	3.1 ± 0.7	4.7 ± 1.2
Electronics					
Misc.	^{208}Tl	IV	(γ)	1.5 ± 0.3	2.9 ± 0.6

As expected Class V events do not show an improved rejection by requiring anti-coincidence between segments. The suppression factors for Class II to IV events for segment anti-coincidence are much larger than the suppression factors for crystal anti-coincidence. The ratio of the segment and crystal suppression factors ranges from 3 to 12 for Class II events and is 8 for Class III events. For Class IV events the ratio ranges from 2 to 30. ^{60}Co events with their two photons in the final state are particularly well suppressed.

The suppression factor for the decay of ^{208}Tl strongly depends on the position of the isotope. For radio-impurities inside or close to the crystal (germanium, detector holder) the suppression factor is larger than for those in a larger distance to the crystal (cables, electronics). This is due to the electrons in the final state which do not reach the detector in the latter case.

Note, that the absolute values of the suppression factors depend on the geometry of the detectors, the array and the electronics as well as the cooling medium.

Chapter 8

Background rejection using pulse shape analysis

The time structure of the germanium detector response, or pulse shape, is analyzed to distinguish between electrons and multiply scattered photons.

Pulse shape analysis methods have already been used for double beta-decay experiments [110–115]. They are now extended to segmented detectors. In this study the focus is on pulse shape analysis after the application of a single segment requirement as presented in the previous chapter and in [68]. Note that the study presented in the previous chapter was purely based on Monte Carlo data. This study will be based on data since no adequate pulse shape simulation is currently available. Thus, the techniques are outlined in this chapter and the results will be discussed in Chapter 11 once the experimental apparatus is described (see Chapter 9).

8.1 Analysis methods

The methods introduced in the following are developed to distinguish two types of events, referred to as *electron-like* and *photon-like*. The methods are trained with *training samples* which are dominated by either of the two types of events. The methods are then tested with independent *test samples*.

8.1.1 Likelihood discriminant method

Four quantities are calculated for each pulse shape. These quantities provided separation power in previous studies [114, 115]. Figure 8.1 shows an ideal pulse and the quantities calculated are indicated. All quantities are given subscripts C and S for the core and segment pulse shapes, respectively. These are:

- the risetime τ_{10-30}, defined as the difference between the times the integrated charge amplitude has reached 10% and 30% of its maximal amplitude;

- the risetime τ_{10-90}, defined as the difference between the times the integrated charge amplitude has reached 10% and 90% of its maximal amplitude;
- the left-right asymmetry ζ, defined as the asymmetry of the area below the left and the right half of the current pulse, A_l and A_r, measured from the maximum[1], $\zeta = \frac{A_l - A_r}{A_l + A_r}$;
- the current pulse width δ, defined as the full width at half maximum of the current pulse.

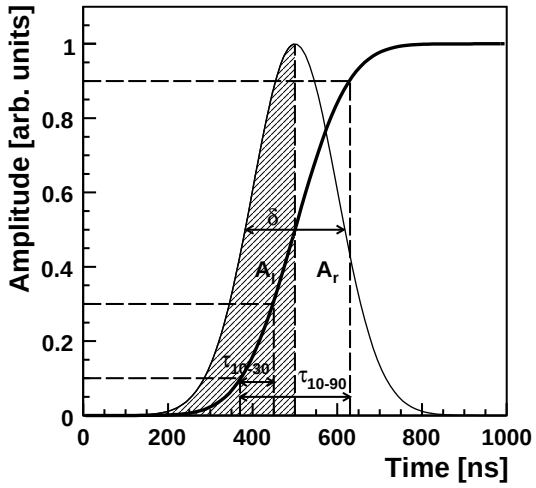

Figure 8.1: Ideal pulse shape: the integrated charge (thick black) and the current (thin black). Indicated are the quantities τ_{10-30}, τ_{10-90}, δ, A_l (hatched) and A_r (open) according to [115].

The variables are histogrammed for both training samples and their integrals are normalized to unity. These relative frequencies are used to define a discriminant, given the event is electron-like or photon-like. The respective overall discriminants, p_{e^-} and p_γ, are calculated by multiplying the individual discriminants:

$$p^k_{e^-} = p(\tau_{10-30,k}|e^-) \cdot p(\tau_{10-90,k}|e^-) \cdot p(\zeta_k|e^-) \cdot p(\delta_k|e^-) \ , \tag{8.1}$$

$$p^k_{\gamma} = p(\tau_{10-30,k}|\gamma) \cdot p(\tau_{10-90,k}|\gamma) \cdot p(\zeta_k|\gamma) \cdot p(\delta_k|\gamma) \ , \tag{8.2}$$

with $k = C$ or S for the core and segment pulses, respectively. Note that no correlations among these quantities are taken into account.

[1]The definition differs from the one given in [114, 115].

Likelihood discriminants (LHD) are constructed from the electron-like and photon-like probability densities for each individual event:

$$D^C = \frac{p^C_{e^-}}{p^C_{e^-} + p^C_\gamma} , \tag{8.3}$$

$$D^{C+S} = \frac{p^C_{e^-} \cdot p^S_{e^-}}{p^C_{e^-} \cdot p^S_{e^-} + p^C_\gamma \cdot p^S_\gamma} , \tag{8.4}$$

where D^C uses information from the core electrode only and D^{C+S} uses information from the core and segment electrodes. D varies between 0 and 1 by construction. D peaks at 1 for electron-like events; for photon-like events D peaks at 0. Events are identified as electron-like for $D > \overline{D}$ and as photon-like for $D < \overline{D}$, where $\overline{D}$ is a chosen parameter.

8.1.2 Library method

The electron-like training samples are interpreted as libraries of electron-like reference pulses. An average χ^2 with respect to all reference pulses is calculated for each pulse shape in the test samples. For the kth reference pulse and the lth pulse shape under study the average χ^2 is defined as

$$\chi^2_{k,l} = \frac{1}{N} \sum_{i=1}^{N} \frac{(x_{k,i} - x_{l,i})^2}{\sigma^2}, \tag{8.5}$$

where N is the number of bins of the pulse shapes and $x_{k,i}$ and $x_{l,i}$ are the pulse heights in bin i of the kth reference pulse and the lth pulse under study. σ^2 is defined as

$$\sigma^2 = \sigma^2_{\mathrm{k}} + \sigma^2_{\mathrm{l}}, \tag{8.6}$$

where σ_{k} and σ_{l} are the noise amplitudes of the reference pulse shape and the pulse shape under study. The noise amplitude is the RMS of the baseline measured during the one μs before the onset of the pulse.

The minimum χ^2 is selected with respect to the reference pulses and denoted $\chi^2_{\mathrm{min}} = \chi^2_{k_{\mathrm{min}},l}$ for each pulse shape in the test sample. Ideally, the minimum χ^2 for electron-like events should be smaller than that for photon-like events. Events are identified as electron-like for $\chi^2_{\mathrm{min}} < \overline{\chi^2}$ and as photon-like for $\chi^2_{\mathrm{min}} > \overline{\chi^2}$, where $\overline{\chi^2}$ is a chosen parameter.

8.1.3 Neural network method

Artificial neural networks (ANNs) are used to separate electron-like from photon-like events. Input neurons are fed with samples of the normalized pulse shapes, starting from the time when the amplitude has reached 10%. 40 consecutive samples per pulse shape are used. In case only the core information is used, the ANN consists of 40 input neurons, 40 hidden neurons and one output neuron. An additional 40 input neurons are used in the ANN if the segment pulse shape is also used.

The ANNs are trained by feeding them with pulse shapes from the two training samples and simultaneously providing the information which of the samples each pulse belongs to (0: electron-like, 1: photon-like). The ANNs adjust the internal neurons iteratively using the Broyden, Fletcher, Goldfarb, Shanno (BFGS) learning method [116]. Each ANN is trained in about 1 000 iterations. The output quantity, NN, is larger for photon-like events than for electron-like events. Events are identified as electron-like for $NN < \overline{NN}$ and as photon-like for $NN > \overline{NN}$, where $\overline{NN}$ is a chosen parameter.

Chapter 9

GERDA test facility

The GERDA test facility at the Max-Planck-Institut für Physik, Munich, was founded with the aim to develop and study germanium detectors for the Phase II of the GERDA experiment. Studies are performed to (1) verify the concept of operating n- and p-type germanium detectors directly in liquid nitrogen or argon and to (2) choose a segmentation scheme suitable for the rejection of background events as described in Chapter 7. Within this context an 18-fold segmented n-type prototype detector for the Phase II of GERDA was developed and produced in close collaboration with the manufacturer Canberra-France [117]. The detector setup and the corresponding simulation are described in Sections 9.2 and 9.3. The operation of an unsegmented n-type germanium detector submerged in liquid nitrogen or argon was the first step towards the GERDA experiment. This test stand is described in Section 9.1.

An additional test stand in which p-type detectors are used for long-term studies is also currently in operation. It provided for example information about the infrared-sensitivity of detectors which is independent of the bulk type.

9.1 Cryoliquid-submersion test stand

A test stand was built which allows the operation of an n-type germanium detector submerged in liquid nitrogen or argon. The cylindrical closed-ended coaxial detector *Mikesch* has an outer and inner diameter of 64.5 mm and 10.0 mm, respectively. The crystal has a height of 77.2 mm with an inner bore depth of 61.0 mm. The operation bias voltage is (-)3 500 V.

The detector is mounted onto a dip-stick allowing the lowering of the crystal into a dewar filled with cryogenic liquid. The dewar holds 4 liters of liquid nitrogen which allows a measuring time of approximately 6 hours. A heating element on the bottom of the dewar is used to increase the evaporation rate of the cryogenic liquid during the warm-up. The FET is mounted onto the dip-stick close to the diode and is also submerged into the cryogenic liquid. A flange is mounted above the FET which closes the opening of

the dewar once the detector is submerged. A feed-through connects the output line to a PSC-823C pre-amplifier board outside the dewar. A copper Faraday shield is mounted onto the board. A heating element on the flange protects the outer surface from icing. A specially produced ^{60}Co source can be lowered into the cryogenic volume through the flange. Figure 9.1 (left) shows a sketch of the setup. Photos of the test stand are shown in the same figure (middle and right).

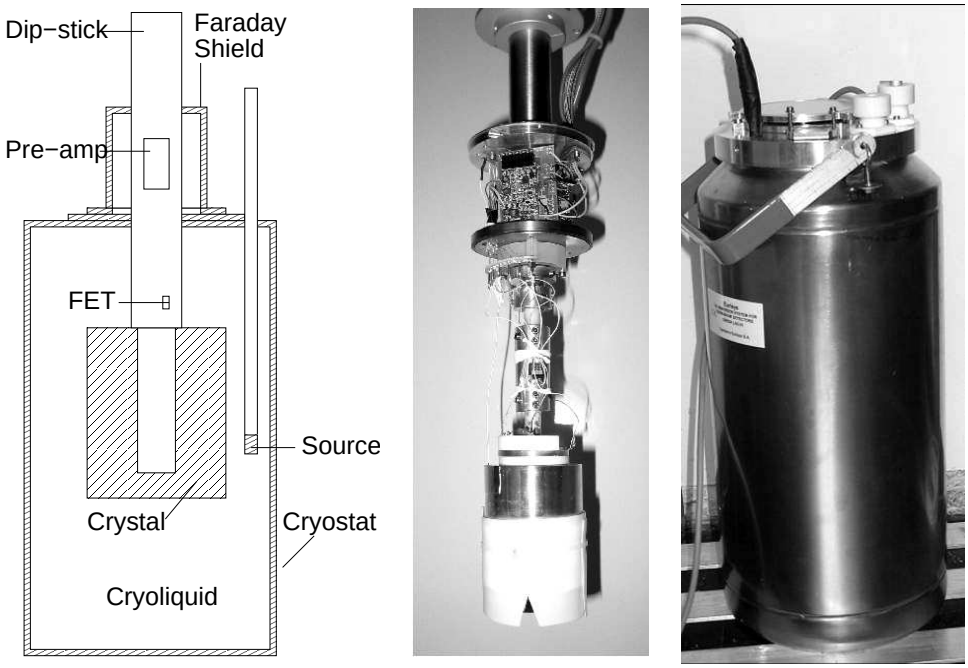

Figure 9.1: Left: Sketch of the submersion test stand. Middle: Photo of the n-type detector attached to the dip-stick. The FET is located close to the crystal. The detector is protected against mechanical damage by a Teflon shield. Right: Photo of the dewar into which the n-type detector is lowered.

9.1.1 Cooling cycle

The time from the submersion of the detector into the cryogenic liquid to the time it is removed and warmed up is referred to as one *cooling cycle*. The detector surface is particularly fragile and sensitive to moisture from the surrounding laboratory air. The warm-up procedure is thus critical with respect to the integrity of the crystal and is described in the following.

After the high voltage is ramped down and the radioactive source is removed the cryostat is sealed with clamps. A safety valve is mounted onto the feed-through for the source. A tube connected to a line with pressurized gaseous nitrogen is inserted through a second feed-through. The heating element on the bottom of the dewar is switched on and causes a

fast evaporation of the cryogenic liquid. After the liquid is evaporated the crystal remains in the cryostat to warm up to room temperature. This steps takes approximately four hours. Gaseous nitrogen is flushed during this stage in order to prevent moisture from the surrounding air to settle onto the detector surface. This is particularly important while the crystal is still cold. After the detector has reached room temperature it is removed and inserted into an aluminum storage container. The container is sealed and a vacuum of about 100 mbar is pumped.

9.1.2 Results

The performance of the *Mikesch* detector was evaluated with respect to the operation in liquid nitrogen or argon and with respect to the stability over several cooling cycles. During each cooling cycle a measurement with a ^{60}Co source was performed.

Figure 9.2 shows the very first ^{60}Co spectrum taken with the detector operated in liquid nitrogen. About 32 000 events were collected in a measuring time of 30 minutes. The two lines of ^{60}Co at 1 173 keV and 1 332 keV are clearly visible. The FWHM of the 1 332 keV peak is about 6 keV. The resolution of the detector was dominated by electronic noise due to the imperfection of the Faraday shield which could not be replaced.

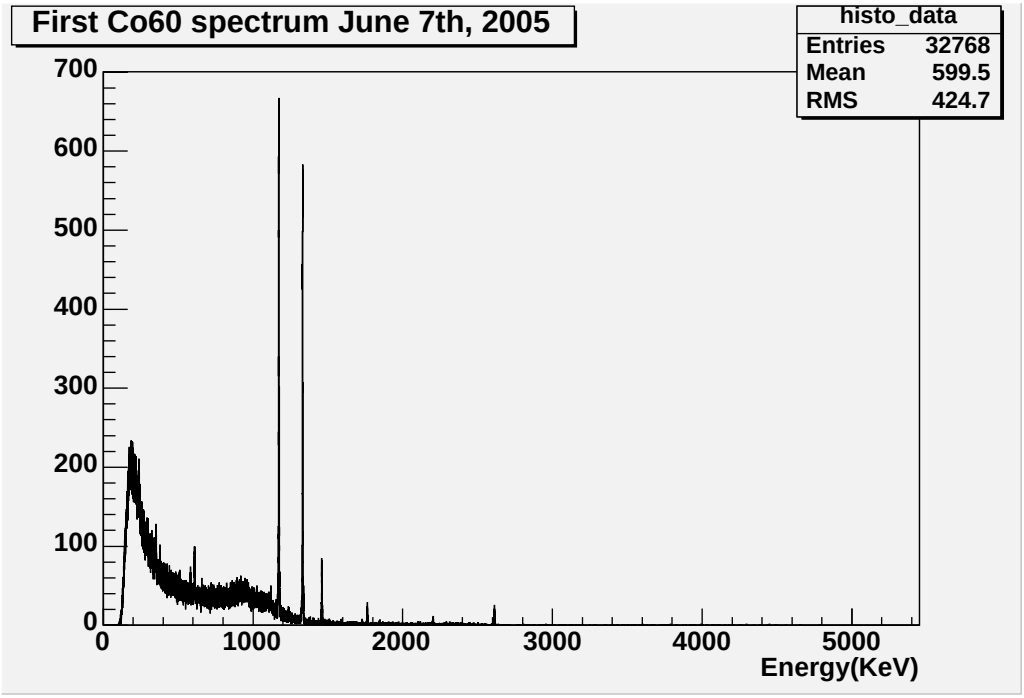

Figure 9.2: First ^{60}Co spectrum taken with *Mikesch* operated in liquid nitrogen. The two lines of ^{60}Co at 1 173 keV and 1 332 keV are clearly visible.

In total 20 cooling cycles were performed with liquid nitrogen as cooling medium over a period of about 8 months. No degradation of the detector performance was observed during that time. The energy resolution at 1 332 keV was constantly around 6 keV and dominated by electronic noise. Further longterm tests with the detector are planned.

The detector showed a similar performance with liquid argon as cooling medium for which three cooling cycles were performed (see Figure 9.2). Due to an insufficiently shielded high voltage feed-through the tests were interrupted.

9.2 Phase II prototype detector *Siegfried*

The first GERDA Phase II prototype detector *Siegfried* is a high-purity n-type germanium detector with a true coaxial geometry. The detector specifications as provided by the manufacturer are summarized in Table 9.1. The germanium crystal has a height of 70 mm and an outer diameter of 75 mm. The inner diameter is 10 mm. The active volume is 302 cm^3, the total mass is 1.6 kg. The detector is 6-fold segmented in the azimuthal angle ϕ and 3-fold segmented in the height z. The segmentation scheme and the detector coordinate system are displayed in Figure 9.3 where a scheme of the cabling (left) and the segment numbering (right) are shown. The segments are read out using a Kapton printed-circuit-board (PCB) with snap-contacts [118]. The operation voltage of the detector is (+)3 000 V.

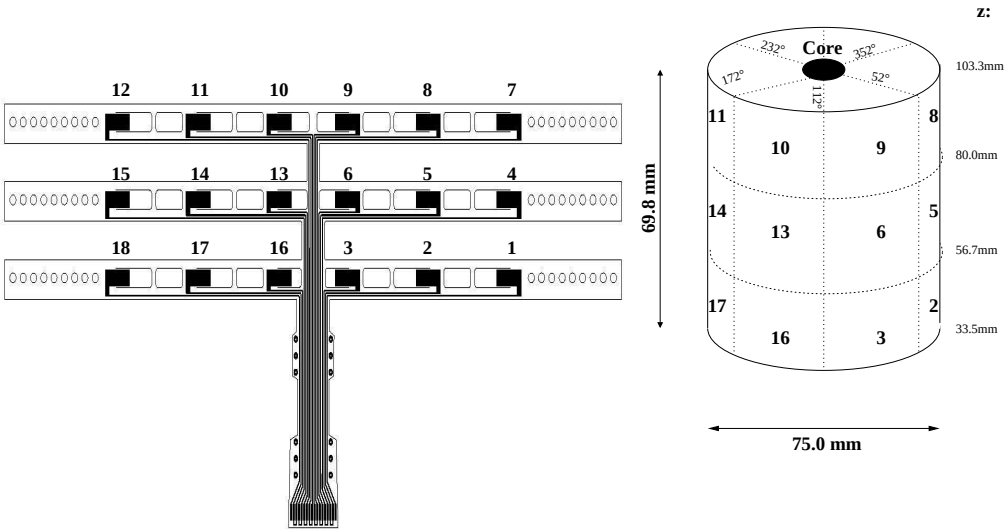

Figure 9.3: Cabling scheme (left) and segment numbering (right) of the prototype detector together with the detector coordinate system.

Table 9.1: Detector specifications as provided by the manufacturer.

Parameter	Value
Operating voltage	(+)3 000 V
Outer diameter	75 mm
Inner diameter	10 mm
Height	70 mm
Active volume	302 cm^3
Mass	1.6 kg
FWHM at 122 keV	0.99 keV
FWHM at 1 333 keV	1.99 keV
Rel. efficiency	80.4%
Peak to Compton ratio	75.7

The crystal was placed inside a two-walled aluminum cryostat with a combined thickness of 6 mm. The detector center is at $z = 66$ mm and $r = 0$ mm, the cryostat extends up to $z = 116$ mm and $r = 75$ mm. A copper cooling finger was used as thermal link between the detector and a 60 l dewar below the detector filled will liquid nitrogen. A temperature monitor was used to measure the temperatures at several locations in the detector cryostat using Pt100 resistors. Liquid nitrogen was refilled daily resulting in a temperature stability of about ± 3 K. A comparison of spectra taken at different temperatures within this range showed neither significant differences in the general shape of the spectra nor in the energy resolution.

A schematic diagram of the detector and the read out scheme are shown in Figure 9.4 (left). The core and each segment were read out using charge sensitive PSC-823C preamplifiers with a decay time of 50 μs. The FET for the core electrode was mounted inside the cryostat close to the detector, the FETs for the segment electrodes were incorporated into the pre-amplifier boards. The boards were mounted onto two massive copper grounding plates of 3 mm thickness on both sides of the detector. These *ears* housed the pre-amplifiers as well as low and high voltage filters. A copper shielding was mounted onto the plates and served as a Faraday cage. Figure 9.4 (right) shows the layout of the feed-throughs to the detector cryostat. One side provided the feed-throughs for the high voltage and the signal lines for segments 10–18 (Connector A). The other side serviced the signal lines for segments 1-7 (Connector B) and housed a multi-purpose connector (Connector C) for the signal lines for segments 8–9 and a test-input for the core pre-amplifier. In addition, the Pt100 at the end of the cooling finger was connected here. The feedback (FB) and drain (D) for the core signal line were also connected to Connector C.

The pre-amplified signals were digitized using a data acquisition system based on 5 14-bit ADC PIXIE-4 modules at a sampling rate of 75 MHz. Energy was calculated using software filters [119]. Recorded pulse shape data consisted of 300 13.3 ns samples of the

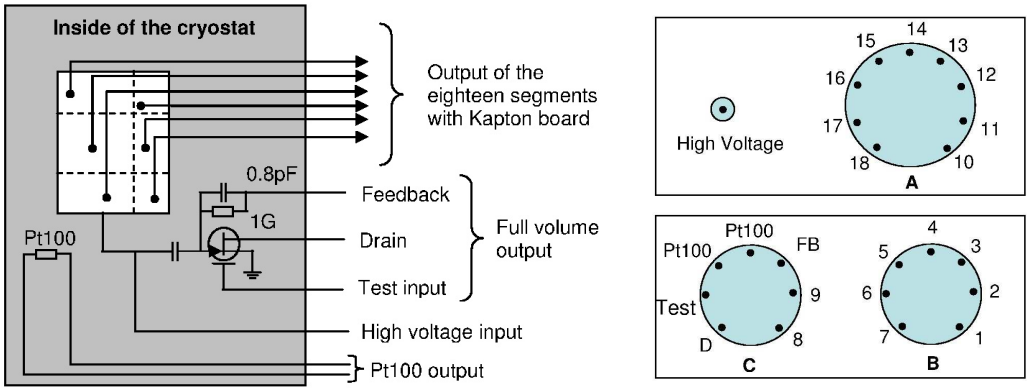

Figure 9.4: Schematic diagram of the detector and the read out scheme (left) and the layout of the feed-throughs to the detector cryostat (right).

integrated charge amplitude. The onset of the signal was delayed by 1 μs. The energy threshold of the core and segment electrodes was set to 20 keV. Cross-talk between the core and the segment pre-amplifiers was corrected for (see Section 11.1). A constraint in the DAQ system, which resulted in the inability to handle late arriving signals, caused a fraction of less than 10% of individual segment signals to not be recorded.

Figure 9.5 (left) shows a detector mock-up with the cable for the prototype detector. A photograph of the detector setup as operated is shown on the right. The pre-amplifiers inside the copper housing are visible in the right ear.

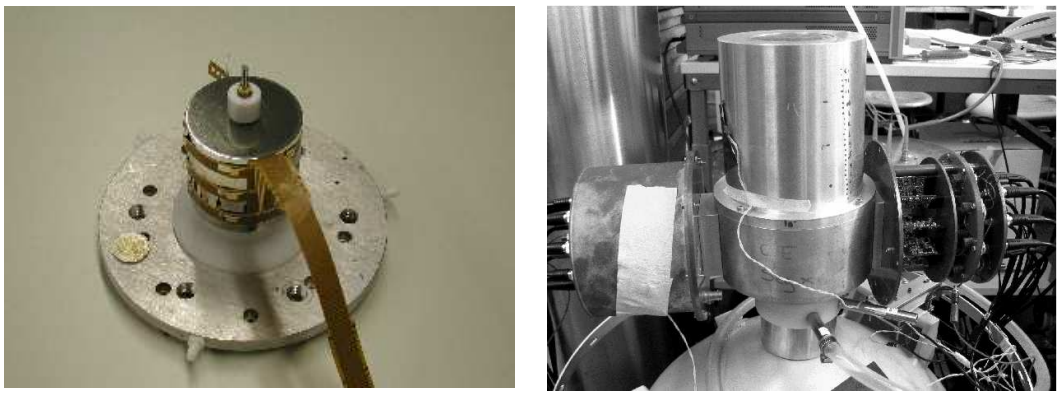

Figure 9.5: Left: Detector mock-up with the cable for the prototype detector. Right: Photo of the prototype detector setup with the two copper ears. The pre-amplifiers inside the copper housing are shown on the right.

9.3 *Siegfried* Monte Carlo simulation

A Monte Carlo simulation of the prototype detector *Siegfried* and the surrounding infrastructure was performed using the MaGe framework introduced in Section 7.1. The energy deposited in each segment was recorded and the core energy was calculated by adding all segment energies. The segment and core energies were individually smeared according to the energy resolutions of the prototype detector measured in the individual channels.

The drift anisotropy of charge carriers inside the germanium diode can cause electrons and holes to deviate from their nominal path. It is therefore possible to measure energy in one segment even if the energy was deposited in the neighboring segment. In the simulation a correction was applied to the segment energies in order to account for this effect. An effective model was used which assigned a segment to each energy deposit depending on its position with respect to the axes of the crystal and the segment borders. The maximum angular shift is 3.5°. The directions of the crystal axes were measured (see Chapter 11) and used as input for the Monte Carlo. The variation of this effect by 40% with respect to the two hemispheres of the detector was also simulated.

Each segment was assigned a relative efficiency with respect to the core of the order of 90%. This effectively models the DAQ-inefficiency.

Chapter 10

Siegfried measurements and data sets

Data were taken with the GERDA Phase II prototype detector *Siegfried* in the setup described in Chapter 9. The goal was to study the detector and to verify the Monte Carlo. Three different sets of measurements were performed to (1) characterize the detector properties and to test the performance of the segmentation; to (2) study the potential to distinguish between electron and photon induced events using energy information from the core and segment electrodes; and to (3) study the time-structure of the detector response. The three sets of measurements and the data sets collected are described in the following.

Due to the placement of the core FET cross-talk between the core signal line (amplified signal) and the segment signal lines (unamplified signals) was observed for one detector hemisphere (segments 1–9). All data sets were corrected for this. Details of the correction procedure can be found in Section 11.1.

10.1 Detector characterization measurements

A 60 kBq ^{60}Co source was positioned 10 cm above the center of the detector cryostat ($z = 216$ mm, $r = 0$ mm). The energy seen by the core electrode was recorded for different bias voltages from 1.5 kV to 3.1 kV in steps of 0.1 kV. The measuring time was 300 s for each measurement.

Segment 14 was scanned in z- and ϕ-directions using a 75 kBq ^{152}Eu source with a copper collimator. The collimator had a length of 52 mm and a pin-hole diameter of 1 mm. The inner and outer diameter were 11 mm and 25 mm, respectively. The spot size on the detector surface was estimated to be 150 mm^2, where the distance between the collimator and the detector was 50 mm. The core energy was required to exceed the threshold. For the scan in the z-direction the source was centered in ϕ on segment 14. A total of 11 measurements with a step size of 5 mm were performed. An uncertainty in z of

$\Delta z = 1.0$ mm was estimated. For the scan in the ϕ-direction the source was centered in z on segment 14. In total 26 measurements were performed. Within the range of Segment 14 the step size was chosen to be 5°. For the neighboring segments 13 and 15 a step size of 10° was chosen. An uncertainty in ϕ of $\Delta\phi = 2.5°$ was estimated. A total of 180° was covered. For each event the pulse shapes of the core and segment electrodes were recorded. About 50 000 events per measurement were written to file.

Segment 11 was scanned in the radius r using the same source and collimator. The distance between the collimator and the top of the detector was 20 mm. The source was centered in ϕ on segment 11. In total seven measurements with a step size of 5 mm were performed. The uncertainty in r was estimated to be $\Delta r = 1.0$ mm. The core energy was required to exceed the threshold. For each measurement the pulse shapes of the core and segment electrodes were recorded. About 50 000 events per measurement were written to file.

10.2 Segmentation study

Several measurements were performed with radioactive sources positioned 10 cm above the center of the detector cryostat ($z = 216$ mm, $r = 0$ mm). For each event the energy and time information of the core and segment electrodes were recorded. The core energy was required to exceed the threshold. Measurements were performed with three different sources: (1) a 60 kBq ^{60}Co source, (2) a 100 kBq ^{228}Th source and (3) a 75 kBq ^{152}Eu source. In the context of the analysis, these data samples are referred to as *source data samples* in the following and contain approximately $4 \cdot 10^6$ events each. An additional measurement without any source was performed in order to estimate the background in the laboratory. This *background data sample* contains approximately 10^6 events. Figure 10.1 shows the raw energy spectra obtained with the core electrode for the three source data samples and the background data sample. The photon lines from the sources are cleary visible. The background lines, in particular the 2 615 keV line from ^{208}Tl, are also visible in each spectrum.

10.3 Pulse shape analysis

A 100 kBq ^{228}Th source was placed at $z = 66$ mm and $r = 175$ mm facing towards the center of segment 14, located in the middle row. Two data sets were taken with different trigger conditions labeled TR_C and TR_S. The former trigger condition requires the core electrode to show an energy above 1 MeV. The collected data set is referred to as *core data set* and contains 127 000 events. The latter trigger condition requires segment S to show an energy above 1 MeV. The collected data set is referred to as *segment data set* and contains 420 000 events. As an example, Figure 10.2 shows a pulse shape measured with the core (left) and segment S electrode (right) for an event in the segment data set.

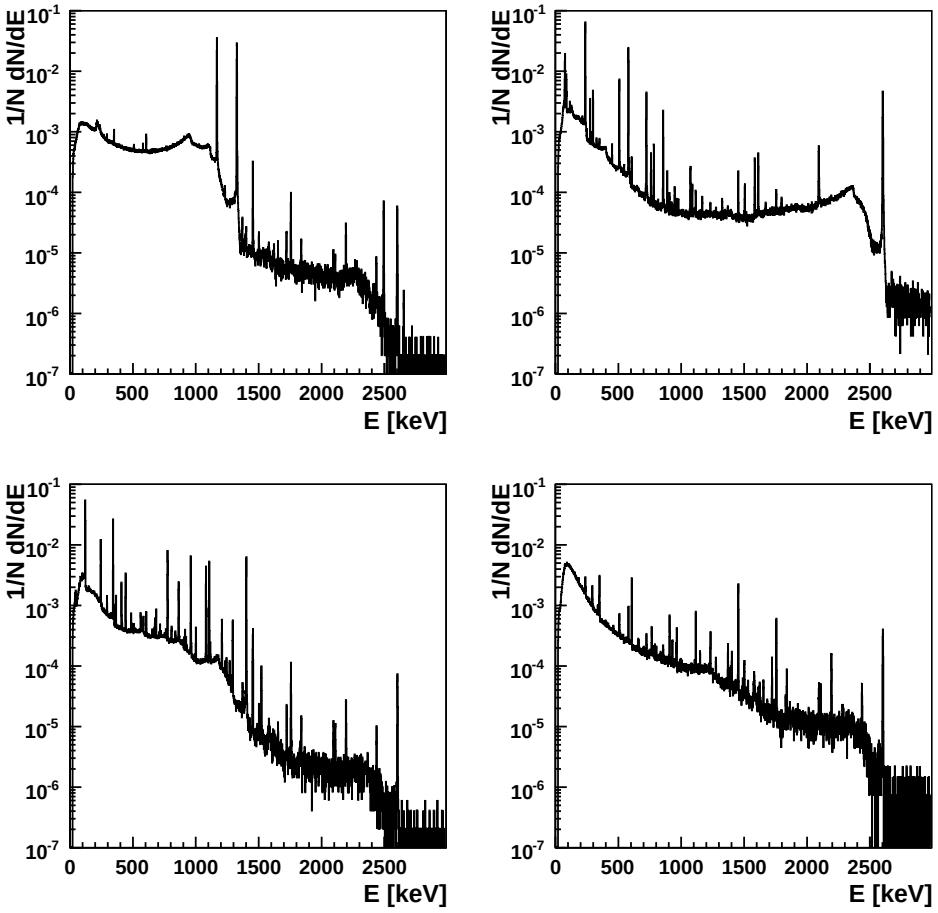

Figure 10.1: Raw energy spectra obtained with the core electrode for the ^{60}Co (top, left), ^{228}Th (top, right) and the ^{152}Eu (bottom, left) source data samples. The sources were placed 10 cm above the detector cryostat. The energy spectrum for the background data sample is also shown (bottom, right). The bin size is 1 keV and the area of each spectrum is normalized to unity.

10.3.1 Event selection

A pre-selection applied to the segment data set collects events with energy deposited in only one segment. It requires the energy measured in segment 14 to be the same as the energy measured in the core within ±5 keV. In total, 150 396 events fulfill the pre-selection criterion.

Four data samples each are selected from the core and segment data sets. The data samples are defined by the energy measured in the core and are labeled:

- *DEP*: The sample contains events with a core energy in the region of (1 593 ± 5) keV. These events are associated with the double escape peak of the 2 615 keV ^{208}Tl pho-

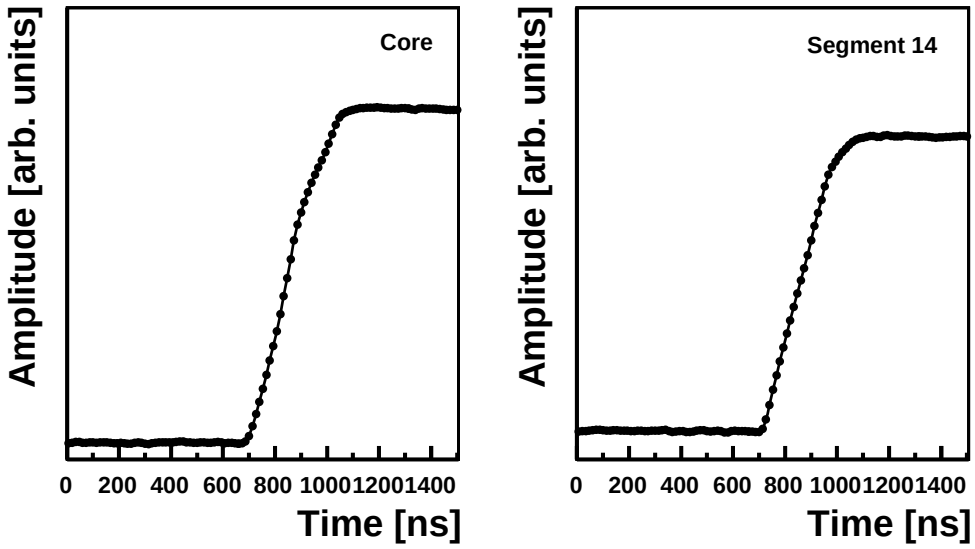

Figure 10.2: Pulse shape measured with the core (left) and segment 14 electrodes (right) for an event in the segment data set. The energy of 1 758 keV seen in the core is completely contained in segment 14. The starting time is chosen arbitrarily in this example. The amplitude is in arbitrary units but the scale is the same for both pulse shapes. The pulse shapes are different as is expected for the different charge carrier types which dominate the development of the pulses.

ton. The photon produces electron-positron pairs of which the positron subsequently annihilates. Both 511 keV annihilation photons escape the detector. Energy is deposited locally, i.e., on a millimeter scale.

- Γ_1: The sample contains events with a core energy in the region of $(1\,620 \pm 5)$ keV. These events are associated with photons of this energy produced in the decay of ^{212}Bi. The photons mostly scatter multiple times before their energy is fully deposited inside the detector.

- Γ_2: The sample contains events with a core energy in the region of $(2\,615 \pm 5)$ keV. These events are associated with photons of this energy produced in the decay of ^{208}Tl. The photons mostly scatter multiple times before their energy is fully deposited inside the detector.

- *ROI*: The sample contains events with a core energy in the region of interest, $(2\,039 \pm 50)$ keV. These events are predominantly associated with Compton scattered photons from ^{208}Tl.

The requirements of the trigger, pre-selection and event selection are listed in Table 10.1. Also the number of events in the corresponding data samples are shown. The amount of background in each data sample, as estimated from taking spectra without the ^{228}Th source present, was found to be less than 1%.

Table 10.1: Requirements of the trigger, pre-selection and event selection, and the number of events in the corresponding data samples. E_C and E_S are the core and segment 14 energy, respectively.

Cut	Condition	Events
Trigger (TR_C)	$E_C > 1$ MeV	127 000
Pre-selection	-	127 000
Selection (DEP)	$\lvert E_C - 1\,593$ keV$\rvert < 5$ keV	1 673
Selection (Γ_1)	$\lvert E_C - 1\,620$ keV$\rvert < 5$ keV	1 965
Selection (Γ_2)	$\lvert E_C - 2\,615$ keV$\rvert < 5$ keV	22 924
Selection (ROI)	$\lvert E_C - 2\,039$ keV$\rvert < 50$ keV	6 431
Trigger (TR_S)	$E_S > 1$ MeV	420 000
Pre-selection	$\lvert E_C - E_S \rvert < 5$ keV	150 396
Selection (DEP)	$\lvert E_C - 1\,593$ keV$\rvert < 5$ keV	3 492
Selection (Γ_1)	$\lvert E_C - 1\,620$ keV$\rvert < 5$ keV	1 972
Selection (Γ_2)	$\lvert E_C - 2\,615$ keV$\rvert < 5$ keV	19 243
Selection (ROI)	$\lvert E_C - 2\,039$ keV$\rvert < 50$ keV	7 707

10.4 Full event display

Figure 10.3 shows the pulse shapes from the core and segment electrodes for an event in the ^{152}Eu sample collected with the source located at an angle of $\phi = 200°$ and $z = 66$ mm. The energy measured with the core electrode is approximately 1 408 keV. The event is associated with a photon from the decay of ^{152}Eu. No energy was deposited in the segments 1–9 - the pulse shapes seen are due to cross-talk induced by the core signal line. Energy was deposited in the segments 11, 13 and 14. This is interpreted as an incident photon which scattered three times inside the crystal. The identification of multiply scattered photons using segmented detectors is demonstrated in the next chapter.

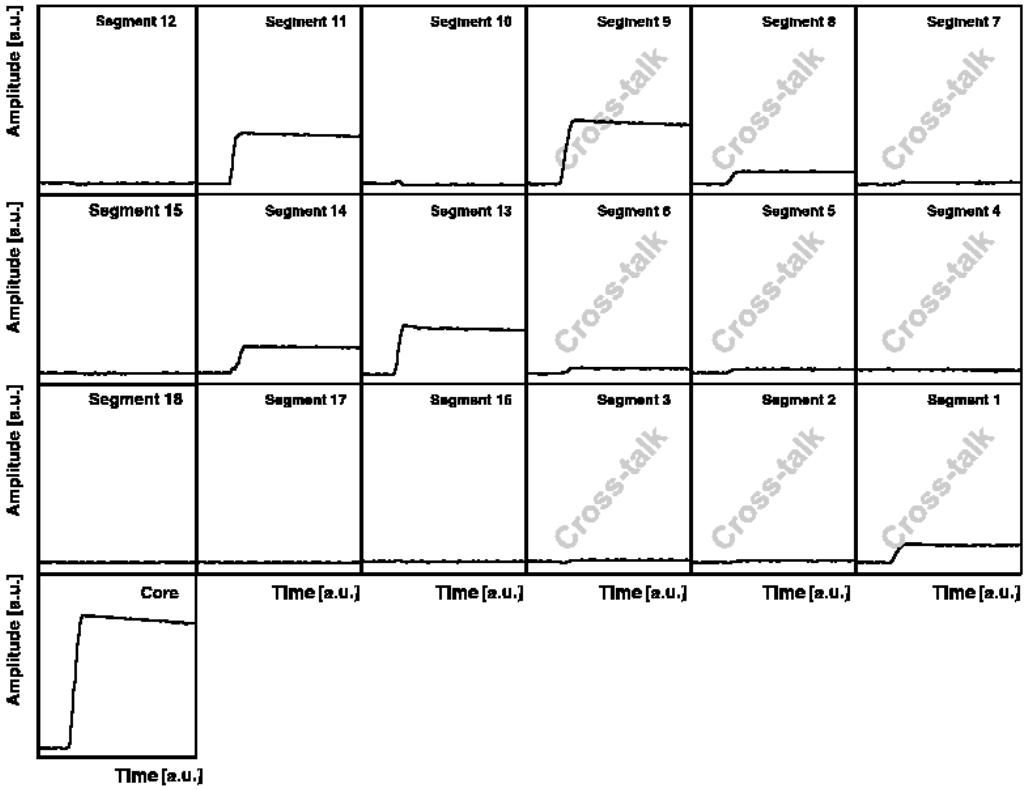

Figure 10.3: Event display for an event with a multiply scattered photon. For details see text.

Chapter 11

Siegfried results

11.1 Prototype detector characterization

11.1.1 Leakage current and capacitance

The leakage current and the capacitance of the detector were measured at Canberra-France. Figure 11.1 shows the total capacity (top) and the leakage current (bottom) as a function of the applied bias voltage. The capacity drops with increasing voltage until it stabilizes at around 2.5 kV at a level of 35 pF. In comparison, the capacitances of the individual segments are of the order of 2 pF (at 3.0 kV). The leakage current increases with increasing voltage until it stabilizes at around 2.5 kV and is of the order of 10 pA.

11.1.2 Bias voltage

The number of events under the 1 333 keV peak of ^{60}Co in the core electrode spectrum was calculated and divided by the measuring time. This average count rate is shown in Figure 11.2 (left) as a function of the applied bias voltage. The rate increases from about 10 Hz at 1.5 kV to 20 Hz at 2.5 kV where it reaches a plateau. As discussed in Section 5.4, partially depleted detectors have a reduced charge collection efficiency, and thus the observed count rate decreases. The charge collection efficiency is constant for bias voltages above the full depletion voltage.

The full width at half maximum (FWHM) of the 1 333 keV peak of ^{60}Co in the core electrode spectrum is shown in Figure 11.2 (right) as a function of the applied bias voltage. The resolution improves from 6 keV at 1.5 kV to about 2.6 keV at 2.5 kV where it reaches a plateau. This is consistent with the measured rate and indicates a full depletion voltage of about 2.5 kV.

11.1.3 Cross-talk

Cross-talk between the core and the segment lines as well as cross-talk between the segment electrodes were studied using the large ^{228}Th sample. Figure 11.3 (left) shows the

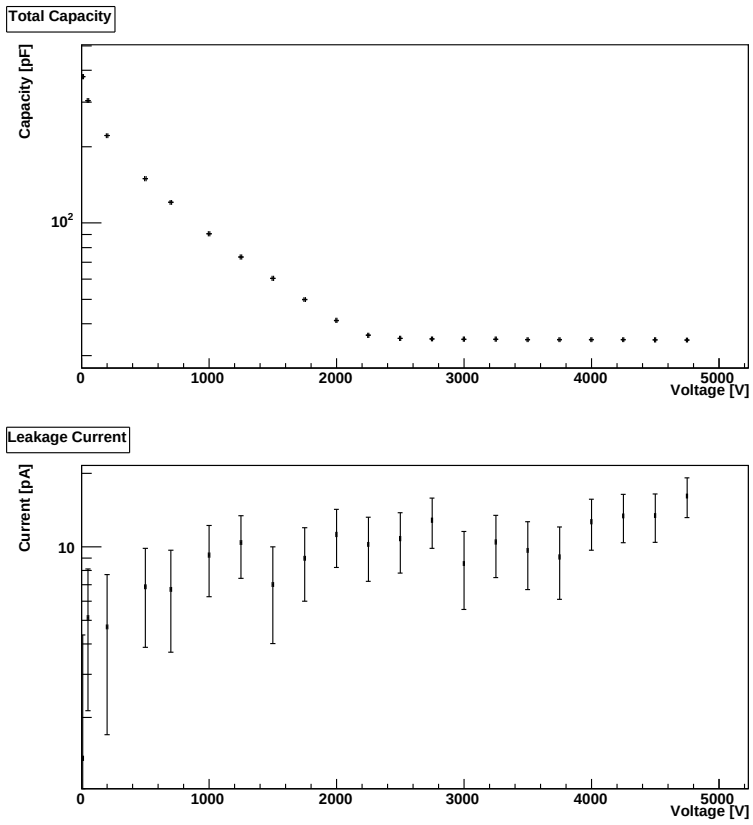

Figure 11.1: Total capacity (top) and leakage current (bottom) as a function of the applied bias voltage. The measurements were performed at Canberra-France.

scatter plot of the energy measured in segment 1 vs. the core energy. Events in which all energy is deposited inside segment 1 are located in the upper diagonal line. Events above this line are physically not possible (neglecting the energy resolution), since the energy measured in the core is the sum of all energy deposits. The vertical lines correspond to events in which the energy of a photon is fully deposited inside the detector but only a fraction of the energy is deposited inside segment 1. The events in which no energy is deposited inside segment 1 should be visible as a horizontal line at zero segment energy. Due to cross-talk between the core and the segment this line is tilted and has a non-vanishing, positive slope. This slope is visible in the segments 1–9 and expected as the amplified core signal is passed close to the segment lines as described in Section 9.2. Neither cross-talk between the core and segments 10–18 nor between the segment electrodes themselves is observed.

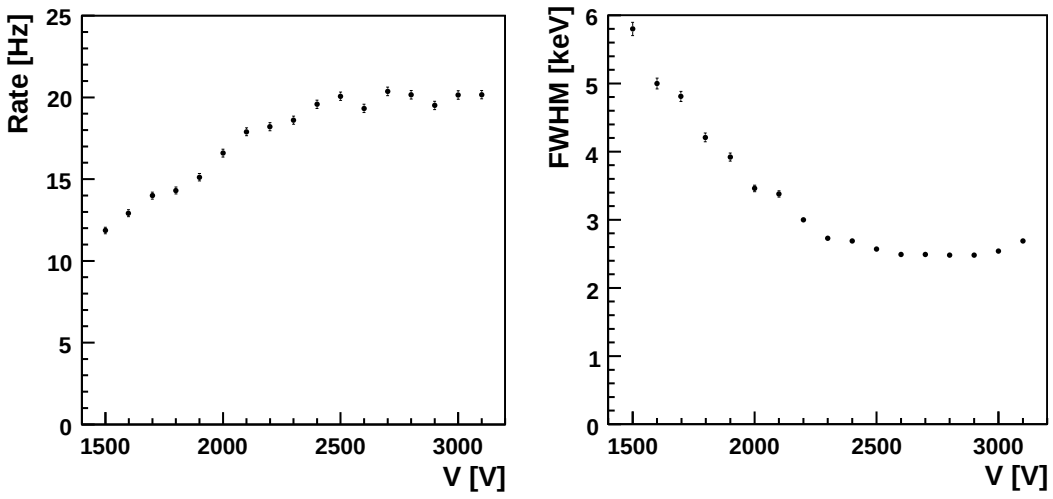

Figure 11.2: Rate (left) and FWHM (right) of the 1 333 keV peak of ^{60}Co in the core electrode spectrum as a function of the applied bias voltage. Both reach a plateau at the full depletion voltage of about 2.5 kV.

A first order correction was applied to all data sets. The true energy deposited inside a segment, E_{true}, is composed of the measured energy, E_{meas}, reduced by a fraction of the core energy, E_{core}:

$$E_{\text{true}} = E_{\text{meas}} - \kappa \cdot E_{\text{core}} \ , \tag{11.1}$$

where κ is a measure for the strength of the cross-talk into each individual segment. Table 11.1 summarizes the measured values for κ which vary between 0.1% and 39%, where only two segments show a cross-talk larger than 4%. Figure 11.3 (right) shows the scatter plot of the energy measured in segment 1 vs. the core energy after the cross-talk correction.

Table 11.1: Strength of the cross-talk between the core and segment lines.

Segment	1	2	3	4	5	6	7	8	9
κ	0.128	0.014	0.0009	0.033	0.024	0.037	0.014	0.037	0.385

Figure 11.4 shows the corrected energy spectrum of segment 1 close to zero energy with $E_{\text{core}} > 1\,750$ keV. Ideally, the spectrum should be Gaussian distributed around zero. As can be seen, second order effects contribute to the spectrum which are not accounted for in the correction. The spectrum peaks at zero and is fitted with a Gaussian, yielding a mean value of (0.207 ± 0.002) keV and a FWHM of (3.04 ± 0.001) keV. A second, much smaller peak around -13 keV is ignored.

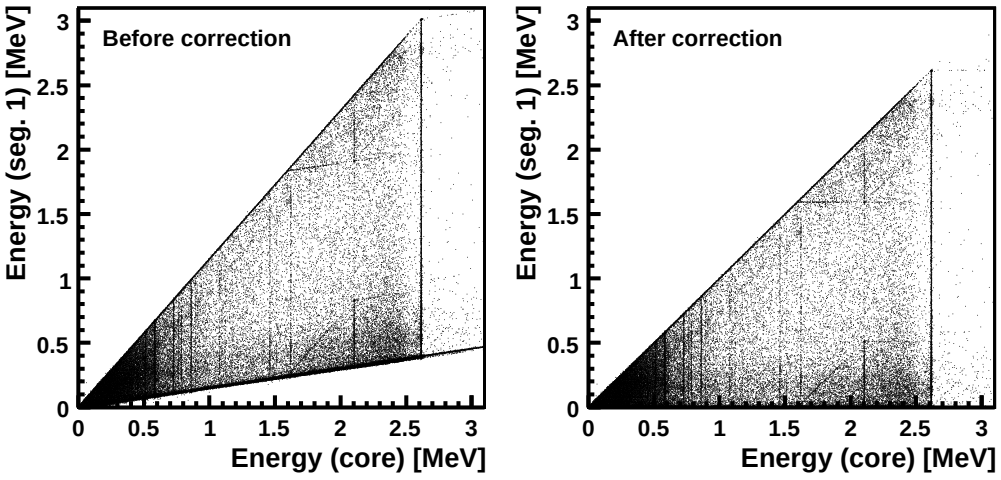

Figure 11.3: Scatter plots of the energy measured in segment 1 vs. the core energy before (left) and after (right) the cross-talk correction described in the text.

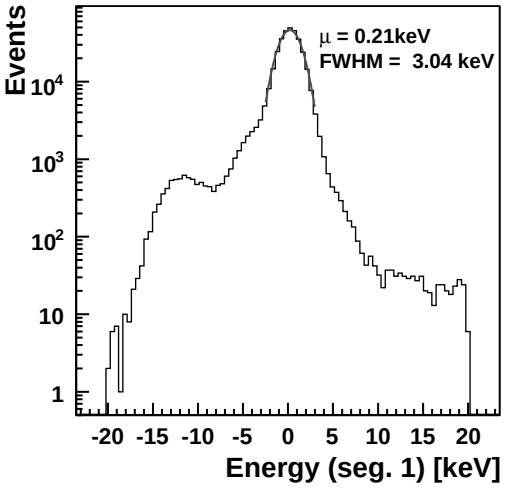

Figure 11.4: Energy spectrum of segment 1 after the cross-talk correction for core energies larger than 1 750 keV and segment 1 energies around zero. For a discussion, see text.

11.1.4 Segment-core correlation

The large ^{228}Th data sample was used to study the correlation between the energy measured in the segments and the core. Figure 11.5 shows a scatter plot of the energy measured in segment 13 vs. the core energy. Several features are visible which are due to the 2 615 keV photon of ^{208}Tl. A few of these are:

- P1: The 2.6 MeV photon does not scatter outside segment 13. Pair production occurs in this segment. One 511 keV annihilation photon escapes segment 13 and deposits its energy in another segment.
- P2: As for P1, but both annihilation photons escape the segment. One photon deposits its energy somewhere else in the detector, the other one escapes the detector.
- P3: The 2.6 MeV photon induces pair production outside segment 13 and one 511 keV annihilation photon escapes the detector. The other annihilation photon deposits its full energy inside segment 13.
- P4: As P3, but the second annihilation photon is absorbed in the detector.
- D1–D3: The 2.6 MeV photon induces pair production. One of the 511 keV annihilation photons deposits a part of its energy inside segment 13 before escaping the detector.

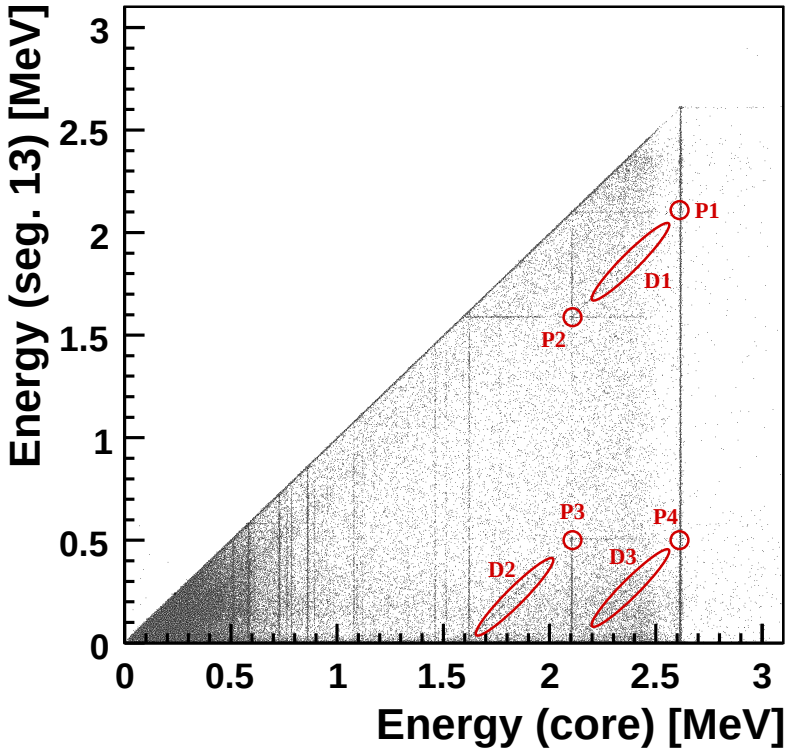

Figure 11.5: Scatter plot of the energy measured in segment 13 vs. the core energy. Several features are visible and some (P1–P4, D1–D3) are described in the text. The few events above the diagonal line for low core energies are due to the DAQ-inefficiency described in Section 9.2.

11.1.5 Linearity

The linearity of the detector and the DAQ-system were evaluated using the large ^{228}Th sample. The most prominent photon lines of the ^{228}Th source, ranging from 510.7 keV to 2614.5 keV were used. The resulting peaks in the energy spectra were fitted with a Gaussian plus linear function. The relative deviation from the nominal peak positions were calculated and fitted with a linear function. The maximum deviation from the line was defined as the deviation from linearity. The deviations of the core and the segments range from 0.02% to 0.09%.

11.1.6 Energy resolution

The energy resolution, the FWHM at 1 333 keV, of the core and segment electrodes are shown in Figure 11.6. The core had an energy resolution of 2.6 keV. The segment resolution varied between 2.4 keV and 4.8 keV with an average of 3.3 keV. The energy resolution was limited by electronic noise. The tightness of the Faraday cage and the proper connection of the grounding plates affected the resolution by an order of one keV. The radiation from machinery in neighboring laboratories also contributed to the noise.

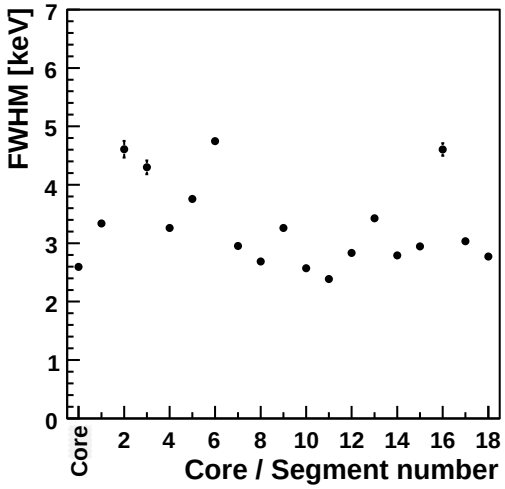

Figure 11.6: Energy resolution of the core and segment electrodes measured as FWHM of the 1.3 MeV peak of ^{60}Co.

11.1.7 Segment scan

The 122 keV line in the spectra of segments 13–15 were fitted with a Gaussian for each data sample collected in the ϕ-scan of segment 14 (see Section 10.1). The average count rate was calculated from the number of events under the peak and the measuring time. Photons in this energy region are expected to deposit their energy locally. Figure 11.7 (left) shows the average count rate of segments 13–15 as a function of the angle ϕ, where the center of segment 14 is found to be at 200°. All three distributions were fitted with

a step function folded with a Gaussian. The step function reflects the small distance between the segments. The Gaussian accounts for the finite spot size of the collimator ($r \sim \mathcal{O}(7)$) mm, the scattering process of these low-energy photons inside the germanium ($r \sim \mathcal{O}(1)$ mm) and the diffusion of charge carriers ($r \sim \mathcal{O}(1)$ mm). The maxima of the three distributions were forced to be separated by 60°. The height and width of each distribution were free parameters. The fit describes the data well although the maximum rate in segment 13 is only 70% of the maximum rate observed in the other two segments. It is most likely that additional material like cabling or support structure inside the cryostat caused this attenuation.

Figure 11.7 (right) shows the rate of the 122 keV line for the segments 11, 14 and 17 as a function of the height z. The distributions were fitted with the same function as for the ϕ-scan while forcing the maxima to be separated by 2.3 cm corresponding to the segmentation scheme. The maximum count rates vary by about 30% which was most likely caused by the geometrical acceptance of the collimated source and the distribution of material inside the cryostat.

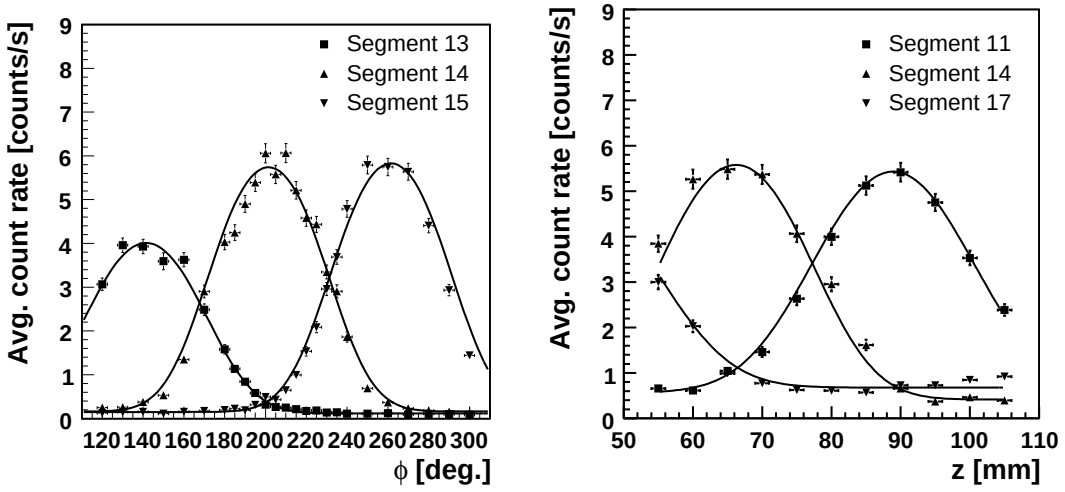

Figure 11.7: Average count rate in the 122 keV peak of ^{152}Eu measured in different segments as a function of the angle ϕ (left) and the height z (right) of the source position.

The widths of the distributions are constant as expected and listed in Table 11.2. On average, they are about $(12.5 \pm 0.3)^\circ$ in ϕ and about (5.9 ± 0.4) mm in z.

11.1.8 Drift anisotropy

The ϕ-scan data samples were used to investigate the drift anisotropy of electrons. Events with a measured core energy of (122±2.5) keV were selected and the 10%-30% and 10%-

Table 11.2: Widths of the average count rate distributions for the ϕ- and z-scan.

Segment	ϕ-scan, FWHM [°]	z-scan, FWHM [mm]
11	-	(5.9±0.8)
13	(12.3±0.5)	-
14	(12.0±0.5)	(5.6±0.6)
15	(13.3±0.7)	-
17	-	(6.1±0.7)

90% risetimes, τ_{10-30} and τ_{10-90}, were calculated. The pulse shapes were dominated by the drift of electrons as the low-energy photons deposited their energy close to the outer surface of the detector. In case the charge carriers drift along the field lines (neglecting the drift anisoptropy discussed in Chapter 5) the risetime is expected to only depend on the radius at which energy is deposited and not on the angle. Figure 11.8 shows the average risetime as a function of the angle ϕ. The dashed lines indicate the segment borders identified in the previous study.

The risetimes vary by about 5% and have a maximum at the center of segment 14. The solid line is a fit with a sine function. The oscillatory behavior shows a period which is consistent with 90°. The effect is smaller than anticipated which can be explained by the finite spot size of the collimator and the fact that not all photons deposit their energy at or close to the outer surface of the detector.

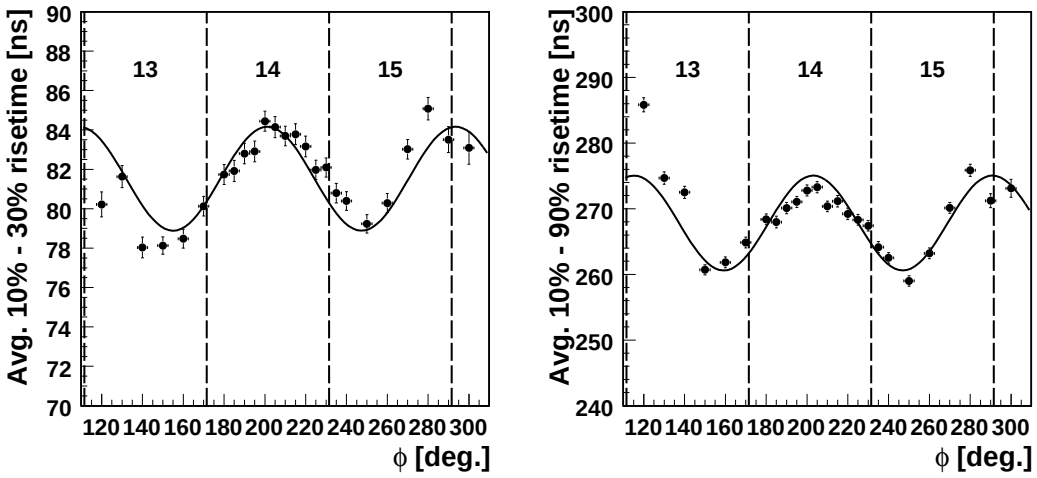

Figure 11.8: Average 10%-30% (left) and 10%-90% (right) risetime measured with the core electrode as a function of the angle ϕ.

11.1.9 Mirror charges and position sensitivity

As discussed in Section 5.5 the charge carriers not only induce charges in the electrodes they drift towards, but also in the neighboring electrodes. In events in which energy is deposited locally the relative heights of pulse shapes from neighboring segments can be used to obtain information on the position of the energy deposit. Events with a measured core and segment energy of (122±2.5) keV were selected from the z- and ϕ-scan data samples and the ratios of the neighboring pulse heights, A, were calculated. The mirror charge asymmetries for a single segment (here: segment 14) are defined as

$$A_{\mathrm{r-l}} = \log\left(\frac{A_{\mathrm{l}}}{A_{\mathrm{r}}}\right) = \log\left(\frac{A_{15}}{A_{13}}\right) , \tag{11.2}$$

$$A_{\mathrm{t-b}} = \log\left(\frac{A_{\mathrm{t}}}{A_{\mathrm{b}}}\right) = \log\left(\frac{A_{11}}{A_{17}}\right) . \tag{11.3}$$

Figure 11.9 (left) shows the average asymmetries for segment 14 as a function of the angle ϕ. A clear dependence of the right-left asymmetry on the angle ϕ is observed. The top-bottom asymmetry is constant as expected. Figure 11.9 (middle) shows the average asymmetries for segment 14 as a function of the height z. A clear dependence of the top-bottom asymmetry on the height z is observed. The right-left asymmetry is constant as expected. The asymmetries are not centered around zero due to the different amplification factors of the pre-amplifiers.

Figure 11.9 (right) shows the average 10%-30% risetime as a function of the radius r for the 122 keV peak measured with segment 11 and the core. The risetime depends almost linearly on the radius. Segment and core risetimes show opposite trends. This can be explained in the context of Ramo's Theorem. The weighting fields used to calculate the induced charge on an electrode are stronger close to the electrode. Charge carriers created close to the core electrode cause a steeper onset of the pulse compared to charge carriers created closer to the outer surface of the detector and thus a shorter 10%-30% risetime. The opposite holds true for the segment electrode. At small radii the risetime as seen in the core electrode does not decrease linearly; a saturation effect in the risetime occurs.

Figure 11.10 shows pulse shapes of an event measured with segments 15, 14 and 13. The data was collected with the ^{152}Eu source at an angle of $\phi = 220°$ and a height of $z = 66$ mm. The energy measured with the core and segment 14 electrode is 1 408 keV. Both neighboring segments show mirror charges induced by the charge carriers.

The position of the energy deposit for a single event cannot be obtained in the data sets used, because the spread in the position sensitive quantities for the $z-$, $\phi-$ and r-coordinate are too large. This is due to the spot size of the collimator used. It was shown in other experiments that pulse shape analysis can yield spatial resolutions of about 0.5 mm [103]. Only the average values of the position sensitive quantities in each data set show a correlation with the source position.

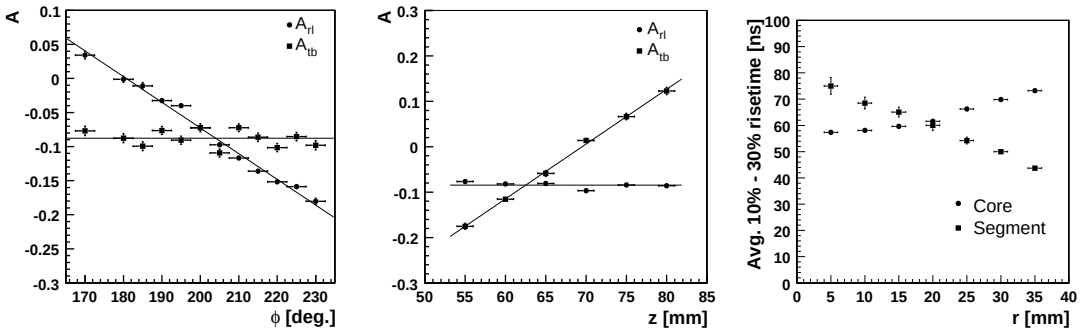

Figure 11.9: Mirror charge asymmetries for the ϕ- (left) and z- (middle) scan data sets. The average 10%-30% risetime versus r as seen in segment 11 and the core are shown on the right.

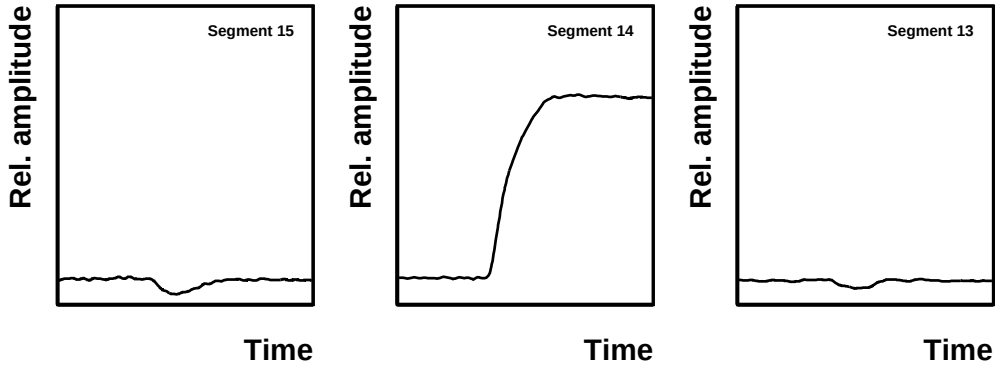

Figure 11.10: Pulse shapes of an event in which energy is deposited in segment 14. The left and right segments show mirror charges.

11.1.10 Summation of segment energies

In order to simulate different segmentation schemes the segment energies were added up in three different schemes: sectors, rings and hemispheres. A sector is obtained by adding the energies of all segments with identical ϕ. A ring is obtained by adding the energies of all segments with identical z. Two hemispheres are obtained by adding the energies of the segments which are read out by pre-amplifiers in the same ear. The effective number of segments for the segmentation schemes are 18, 6, 3 and 2, respectively. Figure 11.11 shows examples of energy spectra for the four effective segmentation schemes, the sum of all segments and the energy measured in the core. The ^{60}Co source data set was used. The spectra show the region around the 1 333 keV peak.

The segment and sector spectra show an almost undisturbed Gaussian shape of the peak. A broadening of the peak is visible in the ring and hemisphere spectra as well as in the sum spectrum. This might be due to the calibration uncertainty and the cross-talk

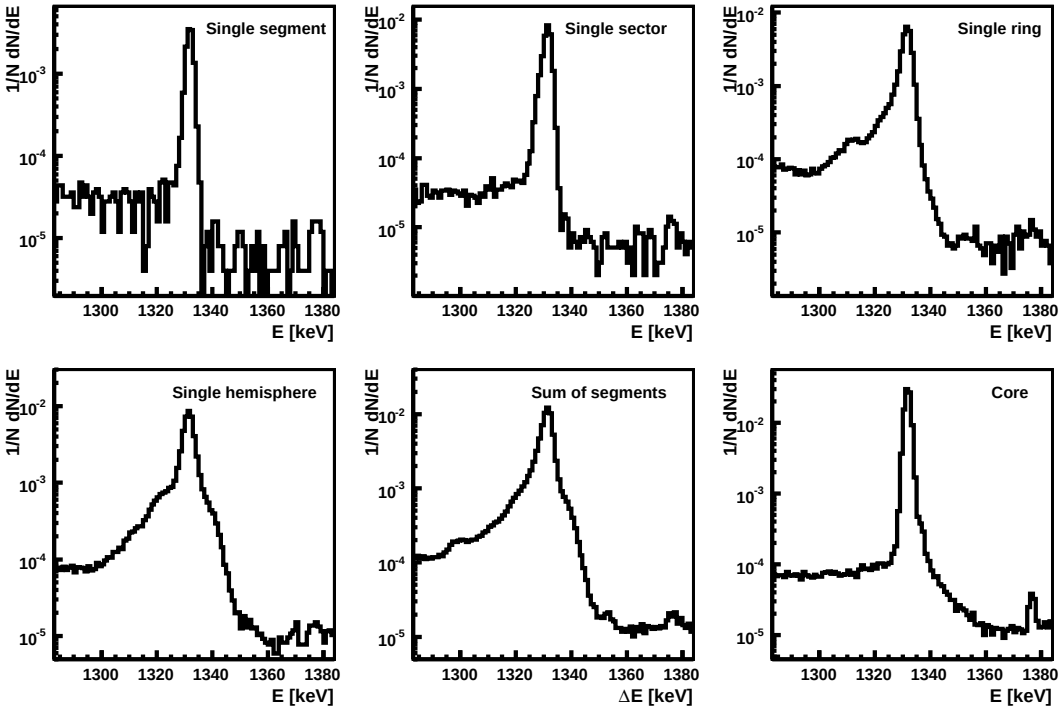

Figure 11.11: Energy spectra of the 1 333 keV line of ^{60}Co for a single segment (top, left), sector (top, middle), ring (top, right) and hemisphere (bottom, left). The sum spectrum of all segments is shown (bottom, middle) as is the core energy spectrum (bottom, right).

between the core and segments 1–9. The core energy spectrum shows a tail towards higher energies which is due to pile-up. The line in each spectrum is fitted with a Gaussian plus linear function in a region ±2 keV around 1 333 keV. The relative energy shift with respect to the core spectrum and the resolutions are summarized in Table 11.3. The largest energy shift is 0.03%. The widths of the distributions vary from (2.74 ± 0.05) keV for the segment spectrum to (3.60 ± 0.03) keV for the ring spectrum.

Table 11.3: Energy shifts of the 1 333 keV peak seen in the segment, sector, ring, hemisphere and sum spectra with respect to the core spectrum. The uncertainty in the shifts are negligible. Also listed are the line resolutions.

Spectrum	Deviation [%]	FWHM [keV]
Segment	< 0.01	2.74 ± 0.05
Sector	-0.03	2.91 ± 0.02
Ring	-0.02	3.60 ± 0.03
Hemisphere	-0.02	3.31 ± 0.03
Sum	-0.01	2.92 ± 0.01

11.2 Distinction between electron and photon induced events using segment energies

The results of the segment anti-coincidence measurements are presented in the following together with a comparison between data and Monte Carlo.

11.2.1 Background estimate

To account for background from radioactive isotopes in the laboratory the fraction of background events in each source data sample is estimated using characteristic photon lines in each spectrum. These lines are associated with the decays of ^{214}Pb (352 keV), ^{214}Bi (609 keV, 1 120 keV, 1 765 keV, 2 204 keV) and ^{40}K (1 461 keV). The photon lines were fitted with a Gaussian plus linear function and the number of events, n_i, under each peak is calculated.

The fraction of events under the ith peak is denoted $f_i = N_i/N$ for the background data sample, where N_i is the number of events under the ith peak and N is the total number of events in the spectrum. The total number of background events, n_{bkg}, was estimated for each source data sample by minimizing a χ^2-function defined as

$$\chi^2 = \chi^2(n_{\mathrm{bkg}}) = \sum_i \frac{(n_{\mathrm{bkg}} \cdot f_i - n_i)^2}{\sigma_i^2 + n_i}, \tag{11.4}$$

where σ_i is the Poissonian uncertainty on the expression $n_{\mathrm{bkg}} \cdot f_i$.

The fraction of background events in the source data samples were estimated to be 14.0% ($\chi^2/d.o.f. = 1.0$) for ^{60}Co, 8.3% ($\chi^2/d.o.f. = 0.7$) for ^{228}Th and 15.8% ($\chi^2/d.o.f. = 8.4$) for ^{152}Eu. The uncertainty of the background fraction was estimated to be 0.1%.

11.2.2 Rejection of photon induced events

The *line suppression factor*, SF_L, is defined similarly to the number suppression factor, SF_N, introduced in Chapter 7 to quantify the power to identify events induced by photons which deposit their full energy within the detector. Events with the line energy not confined to one segment ($N_{\mathrm{s}} > 1$) are identified as photons.

The suppression factors were calculated after the background was subtracted. Line suppression factors were calculated for the photon lines of ^{60}Co (1 173 keV, 1 333 keV and the summation peak at 2 506 keV), ^{208}Tl (511 keV, 583 keV, 861 keV, 2 615 keV and the corresponding single and double escape peaks at 2 104 keV and 1 593 keV), ^{212}Bi (1 620 keV) and ^{152}Eu (122 keV, 245 keV, 344 keV, 779 keV, 964 keV, 1 086 keV, 1 112 keV and 1 408 keV). The results are given in Table 11.4 for data and Monte Carlo. The agreement between data and Monte Carlo will be discussed in Section 11.2.7.

Table 11.4: Suppression factors for different sources and energies as obtained for data and Monte Carlo. The background was subtracted from the data. The agreement between data and Monte Carlo will be discussed in Section 11.2.7. The uncertainties are statistical uncertainties only.

Source	Energy [keV]	SF_N (data)	SF_L (data)	SF_N (MC)	SF_L (MC)
^{60}Co	1 173	-	2.56 ± 0.01	-	2.56 ± 0.01
	1 333	-	2.63 ± 0.01	-	2.63 ± 0.01
	2 506	-	34.6 ± 5.7	-	43.0 ± 11.0
	2 039	14.2 ± 2.1	-	12.5 ± 2.1	-
^{228}Th	511	-	1.92 ± 0.01	-	1.91 ± 0.02
	583	-	2.04 ± 0.01	-	2.01 ± 0.01
	861	-	2.35 ± 0.03	-	2.37 ± 0.05
	1 593	-	1.09 ± 0.02	-	1.09 ± 0.04
	1 620	-	2.85 ± 0.01	-	2.84 ± 0.13
	2 104	-	3.13 ± 0.01	-	3.20 ± 0.11
	2 615	-	3.04 ± 0.02	-	3.23 ± 0.04
	2 039	1.68 ± 0.02	-	1.66 ± 0.05	-
^{152}Eu	122	-	1.01 ± 0.002	-	1.01 ± 0.003
	245	-	1.26 ± 0.01	-	1.22 ± 0.01
	344	-	1.54 ± 0.01	-	1.55 ± 0.01
	779	-	2.29 ± 0.01	-	2.26 ± 0.02
	964	-	2.46 ± 0.02	-	2.41 ± 0.02
	1 086	-	2.54 ± 0.02	-	2.50 ± 0.03
	1 112	-	2.52 ± 0.02	-	2.54 ± 0.04
	1 408	-	2.64 ± 0.02	-	2.72 ± 0.02

The line suppression factors increase from 1.01 ± 0.002 at 122 keV to 3.04 ± 0.02 at 2 615 keV. This increase is expected as the average number of Compton scattering processes increases with increasing photon energy. The rejection power for a single crystal is lower than for an array of detectors due to the geometrical acceptance. Figure 11.12 shows the line suppression factor as a function of the core energy for data and Monte Carlo data.

The double escape peak of the 2 615 keV photon from the de-excitation of ^{208}Tl at 1 593 keV is basically not suppressed. These events are, indeed, mostly single-site events. In comparison, the 1 620 keV line from the decay of ^{212}Bi is suppressed by a factor of 2.85 ± 0.01. These events are predominantly multi-site events. Figure 11.13 shows the energy spectrum of the ^{228}Th data sample with and without a segment multiplicity requirement of $N_\mathrm{s} = 1$. The left figure shows the energy region up to 3 MeV, the right figure shows a close-up of the region around 1.6 MeV. Note that background has not been subtracted from the spectra.

The number suppression factor for the ^{60}Co source is $SF_N = 14.2 \pm 2.1$. It is large compared to the suppression factor for the ^{228}Th source of $SF_N = 1.68 \pm 0.02$. The $Q_{\beta\beta}$-region lies within the Compton continuum of the ^{208}Tl photon. A single scattering process can cause a local energy deposit. In contrast, the ^{60}Co source can cause an energy deposit in this energy region only if both photons (1 173 keV and 1 333 keV) deposit energy in the same segment. Figure 11.14 shows the energy spectrum of the ^{60}Co data sample with and without a segment multiplicity requirement of $N_s = 1$. The left figure shows the energy region up to 3 MeV, the right figure shows a close-up of the region around the $Q_{\beta\beta}$-value. Note that background has not been subtracted from the spectra.

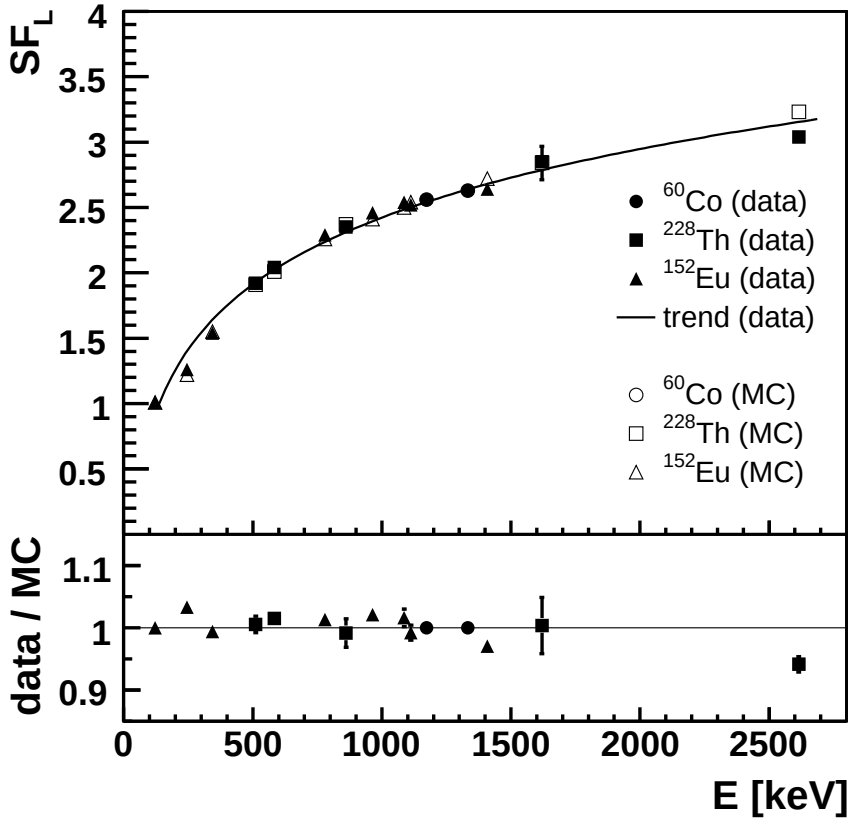

Figure 11.12: Top: Line suppression factor as a function of the core energy for data (solid marker) and Monte Carlo data (open marker). The curve guides the eye. Bottom: Data to Monte Carlo ratio. The average deviation is less than 5%. A discussion of the agreement between data and Monte Carlo is presented in Section 11.2.7.

11.2.3 Segmentation scheme evaluation

To study the power of different segmentation schemes to identify events induced by photons, segment energies were added in three patterns: sector, ring and hemisphere. The sup-

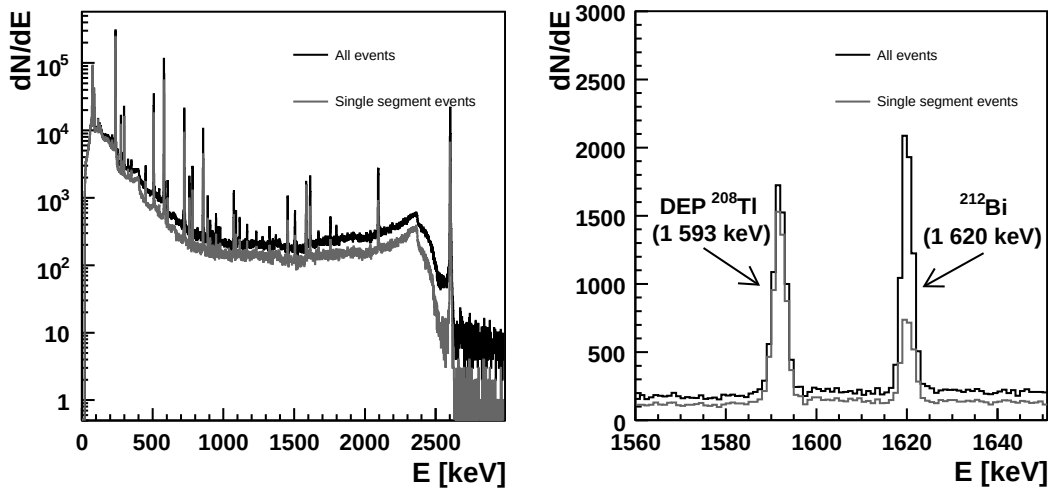

Figure 11.13: Core energy spectrum of the ^{208}Th source data sample for all events (black spectrum) and those with a segment multiplicity of $N_s = 1$ (gray spectrum). The left spectrum shows the energy region up to 3 MeV, the right spectrum is a close-up of the region around 1.6 MeV. The double escape peak from ^{208}Tl (1 593 keV) is hardly suppressed ($SF_L = 1.09 \pm 0.02$) while the ^{212}Bi line (1 620 keV) is suppressed by a factor of $SF_L = 2.85 \pm 0.01$. Note that background has not been subtracted from the spectra.

pression factors for each segmentation scheme were obtained as described in Section 11.2.2 with segments replaced by sectors, rings or hemispheres. Table 11.5 gives the number suppression factors and line suppression factors for selected photon lines for all four schemes (including the 18-fold segmentation scheme) obtained from the measurements. As expected, the number and line suppression factors increase with an increasing effective number of segments.

Table 11.5: Number and line suppression factors for selected photon lines for all four segmentation schemes. Background was subtracted from the data. The numbers in brackets are the effective number of segments of the specific scheme. The uncertainties are statistical uncertainties only.

Source	Energy [keV]	SF (18)	SF (6)	SF (3)	SF (2)
^{152}Eu	344	1.54 ± 0.01	1.36 ± 0.004	1.24 ± 0.003	1.12 ± 0.003
^{60}Co	1 333	2.63 ± 0.01	1.94 ± 0.01	1.71 ± 0.004	1.30 ± 0.003
^{228}Th	2 615	3.04 ± 0.02	2.16 ± 0.01	1.86 ± 0.01	1.38 ± 0.01
^{60}Co	2 039	14.2 ± 2.1	9.63 ± 1.21	3.92 ± 0.33	2.61 ± 0.19
^{228}Th	2 039	1.68 ± 0.02	1.43 ± 0.02	1.40 ± 0.02	1.18 ± 0.02

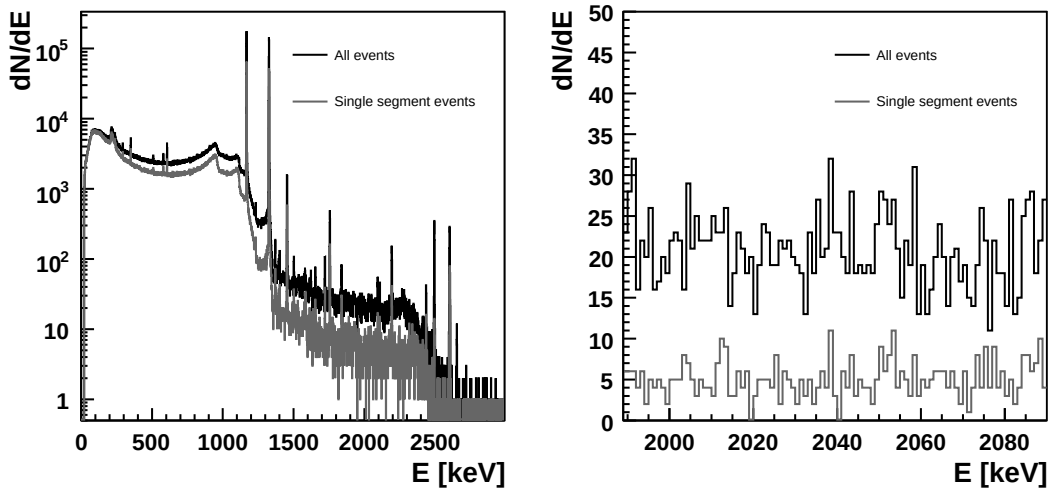

Figure 11.14: Core energy spectrum of the ^{60}Co source data sample for all events (black spectrum) and those with a segment multiplicity of $N_{\mathrm{S}} = 1$ (gray spectrum). The left spectrum shows the energy region up to 3 MeV, the right spectrum is a close-up of the $Q_{\beta\beta}$-region (2 039 keV). In this energy region the single-segment spectrum is suppressed by a factor of $SF_N = 14.2 \pm 2.1$. Note that background has not been subtracted from the spectra.

Figure 11.15 shows the line suppression factors for the selected photon lines as a function of the effective number of segments for data and Monte Carlo data.

11.2.4 Threshold effects

The effect of the threshold on the line suppression factors was studied by varying the threshold of the core and segment channels from 15 keV to 100 keV. A sharp rise of the line suppression factors was observed towards 15 keV due to an increased noise level. Noise is not simulated in the Monte Carlo and the effect is not present. Between 20 keV and 100 keV the line suppression factors decrease by up to 7%. In particular, the suppression factor for the double escape peak at 1 593 keV decreases by about 4%. The threshold of 20 keV proves to be stable with respect to noise and sufficient with respect to the identification of photons.

11.2.5 Geometry dependence of results

Several source positions were studied. Its distance from the crystal was varied. In addition, the source was placed at half the crystal height facing the detector surface ($z = 66$ mm). The radial distance between the source and the crystal was varied. No significant difference in the suppression factors was found.

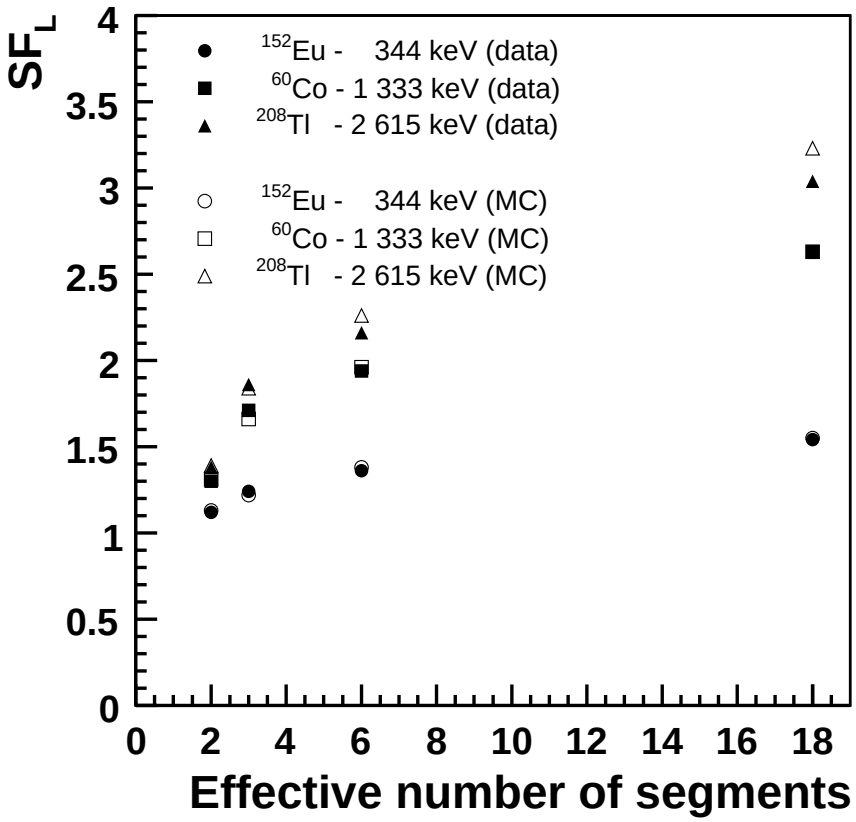

Figure 11.15: Line suppression factors for selected photon lines as a function of the effective number of segments for data (solid marker) and Monte Carlo (open marker).

11.2.6 Background

The uncertainty on the background fraction in the data samples was estimated to be 0.1%. A variation of the estimated background fraction by this amount did not reveal significant differences in the line suppression factors. For ^{60}Co the number suppression factor decreases with an increasing background fraction because background events in the energy region around 2 MeV are mostly induced by singly Compton scattered photons from ^{208}Tl.

11.2.7 Data to Monte Carlo comparison

The results of the Monte Carlo simulation introduced in Section 9.3 are compared with data from the ^{60}Co measurement. Equivalent results were obtained for all three sources used. The data were normalized to unity as was the sum of the background plus Monte Carlo data. The fraction of background was estimated as described in Section 11.2.1.

Figure 11.16 (top, left) shows the core energy spectrum for the ^{60}Co source. The data are indicated by the black marker. Also shown is the statistical uncertainty. The background data are represented by the hatched histogram, the Monte Carlo data by the open histogram. The background contribution was estimated as described in Section 11.2.1. Below energies of 100 keV the Monte Carlo plus background exceeds the data due to the trigger turn-on which is not described by Monte Carlo. The Compton continuum of the two ^{60}Co lines is described by Monte Carlo with an average deviation of about 5%. The number of events under the peak for the two ^{60}Co lines are lower in data by about 10%. The tails left and right of the gamma peaks in data are due to the charge collection efficiency and pile-up. These effects are not included in the simulation. The region above 1.3 MeV is significantly populated by background events. In this region the average deviation between data and Monte Carlo plus background data is of the order of 10% or less. In particular, the number of events under the peak for the ^{60}Co summation line and the ^{208}Tl line agree within the statistical uncertainties.

Figure 11.16 (top, right) shows the occupancy of each segment, i.e., the fraction of events in which energy is deposited in the segment under study. No cut on the energy has been applied apart from the threshold requirement. Clearly visible are three groups of segments (channels 1-6, 7-12, 13-18) which correspond to the three z-positions bottom, middle and top, respectively[1]. As expected, the bottom segments have the lowest, the top segments the highest occupancy. A pattern within each group is present which can be explained by the drift anisotropy of the charge carriers. The structure is reproduced by Monte Carlo using an effective model for the anisotropy. Without taking the anisotropy into account no structure is visible. The deviation between data and Monte Carlo plus background data is in the range of 5-10%.

Figure 11.16 (middle, left) shows the segment multiplicity N_{s} without any cut on the core energy. Data and Monte Carlo range up to multiplicities of 7-8. For multiplicities up to 3 the deviation between data and Monte Carlo plus background data is not significant. For higher multiplicities the data exceeds the Monte Carlo with increasing multiplicity.

Figure 11.16 (middle, right) shows the average segment multiplicity as a function of the energy measured with the core electrode up to 3 MeV. A larger bin size is chosen for energies above 1.5 MeV due to limited statistics. For energies up to 1 MeV the average multiplicity increases with energy from 1 to about 1.5. For energies between 1 MeV and 1.3 MeV the multiplicity increases up to 2.2. The deviation between data and Monte Carlo plus background for energies below 1.3 MeV ranges up to 5%. The Monte Carlo describes all features visible in the data. For higher energies the average deviation is of the order of 15%, where the Monte Carlo shows a larger average multiplicity.

[1]Note the difference between the channel ID and the segment number.

Figure 11.16 (bottom, left) shows the energy spectrum measured with (arbitrarily chosen) segment 6 up to energies of 3 MeV. The features described for the core electrode are also seen here. The deviation between data and Monte Carlo plus background data ranges up to 10%.

Figure 11.16 (bottom, right) shows the occupancy for segment 6 as a function of the energy measured with the core electrode up to 3 MeV. A larger bin size is chosen for energies above 1.5 MeV due to limited statistics. The occupancy ranges from 5% to 8% for energies below 1.3 MeV. For larger energies the occupancy ranges up to 15%. The Monte Carlo describes all features visible in the data. Data and Monte Carlo plus background data agree within the statistical fluctuations.

The suppression factors derived from the data are compared with those obtained from the Monte Carlo simulation in Table 11.4. The average deviation between data and Monte Carlo is less than 5%. The absolute values depend on the DAQ-inefficiency and the detector geometry.

The overall agreement between data and Monte Carlo plus background data is good. The remaining discrepancies between data and Monte Carlo plus background data could stem from (1) the modeling of the exact detector geometry including dead layers and segment borders, (2) the missing modeling of the drift of charge carriers, especially close to the surface of the crystal, (3) the missing simulation of the pre-amplifier response and (4) effects which are not included in the simulation such as pile-up, the charge collection efficiency and the trigger turn-on.

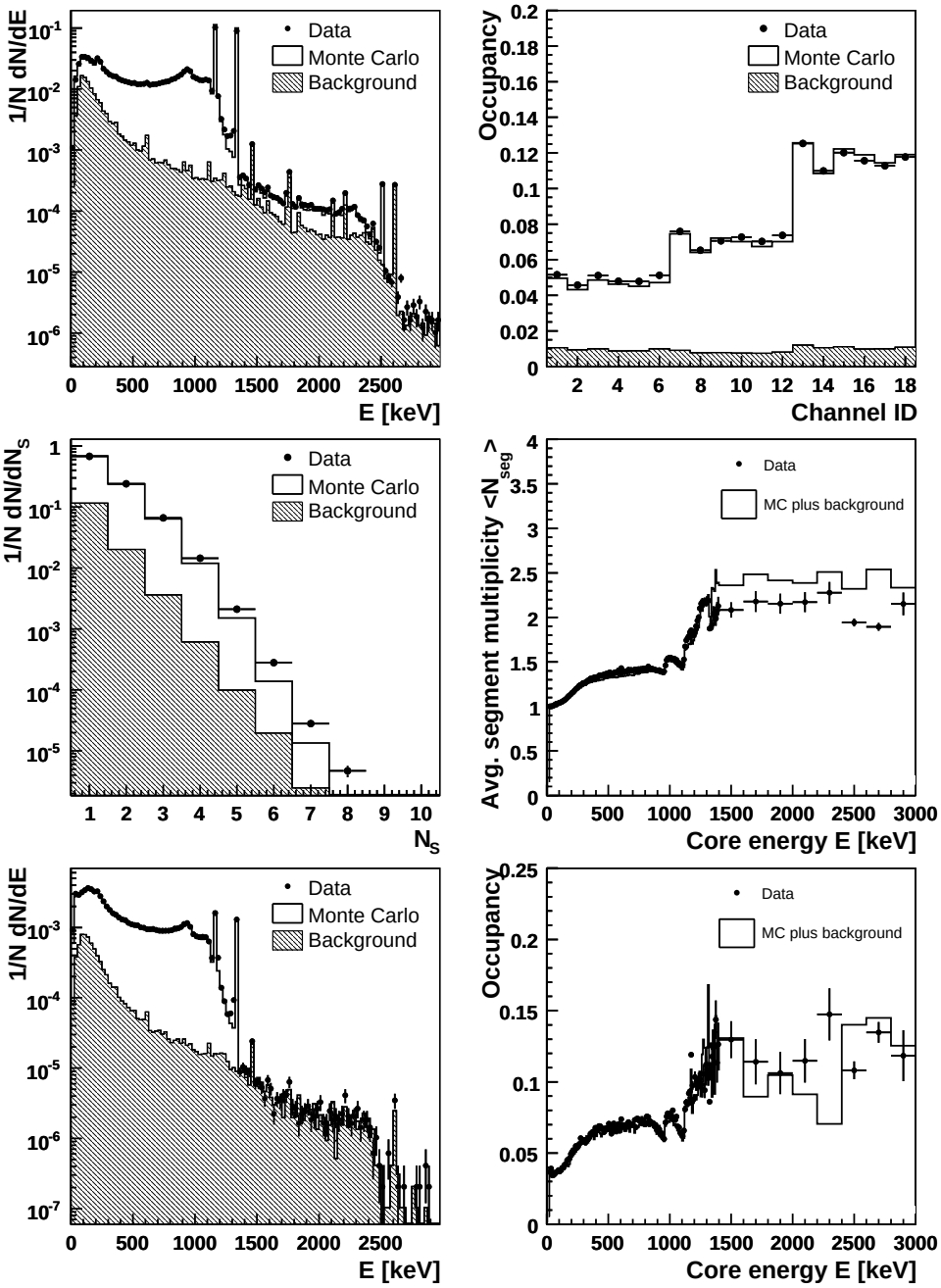

Figure 11.16: Comparison between data and Monte Carlo plus background for several quantities under study for the ^{60}Co source data set. The data is indicated by the black marker. The background data is represented by the hatched histogram, the Monte Carlo data by the open histogram. The background contribution is estimated as described in Section 11.2.1. Top, left: core energy spectrum. Top, right: occupancy of all segments. Middle, left: segment multiplicity. Middle, right: average multiplicity as a function of the core energy. Bottom, left: energy spectrum taken with segment 6. Bottom, right: occupancy of segment 6 as a function of core energy. See text for further details.

11.3 Identification of photon events using pulse shape analysis

The three analysis methods introduced in Chapter 8 are applied to the data sets defined in Section 10.3. A special Monte Carlo study is presented to allow the interpretation of the results of the pulse shape analysis. The performance of the pulse shape analysis with and without segment information is compared.

11.3.1 Monte Carlo simulation

A Monte Carlo study similar to the one described in Chapter 7 was performed to estimate the spatial distribution of the energy deposited in the detector for events in the data sample. The trigger, pre-selection and event selection requirements discussed in the previous section were applied to the Monte Carlo data. The data sets are referred to as *core* and *segment Monte Carlo data sets*.

The radius R_{90} introduced in Chapter 7 is used as measure for the spatial distribution of the energy deposited inside the detector. Figure 11.17 shows the distribution of R_{90} for the DEP, Γ_1, Γ_2 and ROI samples for the core (left) and segment (right) Monte Carlo data sets. All distributions are normalized to unity. The R_{90} distributions range from 0.1 mm ($\log_{10}(R_{90}) = -1$) up to 7 cm ($\log_{10}(R_{90}) = 1.8$). The DEP samples are dominated by events with R_{90} in a region from 0.1 mm to 1 mm. A long tail towards larger radii is visible and mostly due to events in the underlying Compton-shoulder of ^{208}Tl and events in which electrons undergo hard bremsstrahlung processes. The R_{90} distributions for the Γ_1 and ROI samples have two prominent regions each, one at radii from 0.3 mm to 1 mm and a second from 3 mm to 6 cm. The latter one is due to multiply scattered photons whereas the former is due to photons with higher energy which only scatter once and then leave the detector. The R_{90} distributions for the Γ_2 samples range from 0.3 mm to about 7 cm with a maximum at around 2 cm for the core Monte Carlo data sample and at around 1 cm for the segment Monte Carlo data sample. The sample is dominated by events in which photons scatter multiple times. No peak at small R_{90} is visible.

It is expected that the single segment requirement suppresses events with large values of R_{90}. Events in which energy is deposited over a large volume compared to the size of the segment are expected to be removed. Indeed, the distributions of R_{90} in the segment Monte Carlo data samples are suppressed in the region above 1 cm. The peaks between 0.1 mm and 1 mm in the DEP, Γ_1 and ROI samples are more pronounced in this case.

Single-site and multi-site events are defined by requiring $R_{90} < \overline{R}$ and $R_{90} > \overline{R}$, respectively, where $\overline{R}$ is a chosen parameter value. The distributions of R_{90} for the DEP samples suggest $\overline{R} = 2$ mm ($\log_{10}(\overline{R}) = 0.3$). Also, due to the sampling rate of 75 MHz and the average drift velocity of charge carriers ($\mathcal{O}(10^8)$ mm/s) energy deposits closer than about 2 mm cannot be resolved. The fractions of single-site events in the Monte Carlo data samples are thus defined and summarized in Table 11.6. Also listed are the

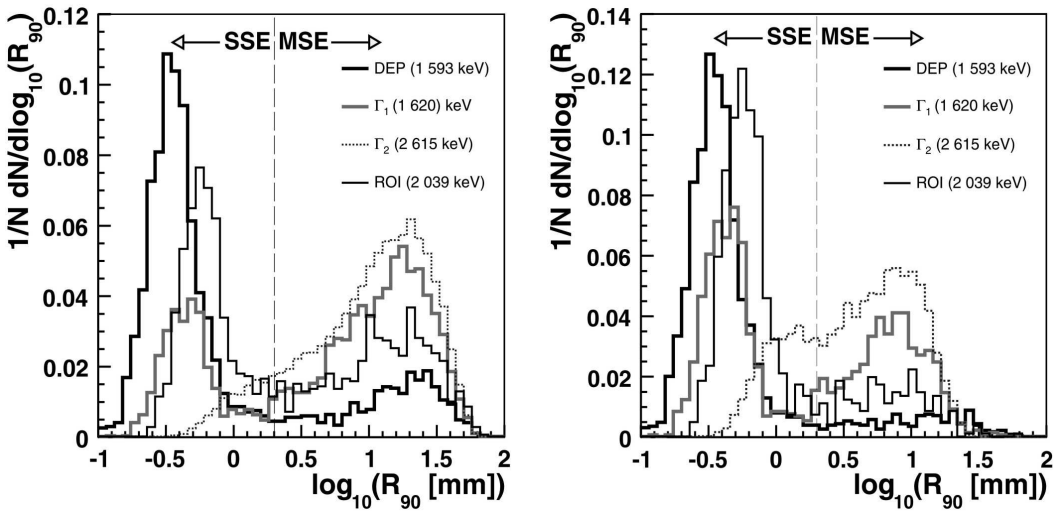

Figure 11.17: Normalized distributions of R_{90} for the DEP, Γ_1, Γ_2 and ROI samples for the Monte Carlo core (left) and segment data sets (right). Single-site events (SSE) and multi-site events (MSE) are defined by requiring $R_{90} < 2$ mm and $R_{90} > 2$ mm (dashed line) as discussed in the text.

corresponding systematic uncertainties of the fractions which are derived by varying the parameter $\overline{R}$ by ± 1 mm.

Table 11.6: Fractions of single-site events in the Monte Carlo data samples. The errors are derived by varying the parameter $\overline{R}$ by ± 1 mm.

Monte Carlo data samples	DEP (1 593 keV)	Γ_1 (1 620 keV)	Γ_2 (2 615 keV)	ROI (2 039 keV)
Core samples	$(77.9^{+1.6}_{-3.4})\%$	$(30.5^{+4.0}_{-3.6})\%$	$(12.2^{+\ 6.0}_{-\ 7.6})\%$	$(52.4^{+3.8}_{-7.6})\%$
Segment samples	$(89.0^{+1.1}_{-3.0})\%$	$(55.0^{+5.0}_{-4.4})\%$	$(30.0^{+10.0}_{-16.8})\%$	$(77.6^{+3.4}_{-6.7})\%$

The Monte Carlo data samples are not purely composed of single-site or multi-site events. The DEP samples are dominated by single-site events, the Γ_1 and Γ_2 have large fractions of multi-site events. Events in the DEP samples are referred to as *electron-like* while events in the Γ_1 and Γ_2 samples are referred to as *photon-like* in the following. Note, that these two labels do not describe an intrinsic property of an event (such as the range of energy deposition), but they are used to emphasize the different probabilities of the event being single-site or multi-site.

11.3.2 Results

Half of the DEP and Γ_1 data samples were used to train the methods. The other half of the samples, together with the Γ_2 and ROI samples, were used to test the analysis methods. The DEP and Γ_1 samples were selected for training in order to avoid biases due to the difference in energy of events in the two samples. For each event the maximum of each pulse shape was normalized to unity.

Figure 11.18 shows the normalized distributions of the four quantities calculated for the likelihood discriminant method. The quantities are calculated from the core pulse shape in the two segment data samples. The average risetime of pulses in the DEP sample are larger than that in the Γ_1 sample [2].

The analyses were applied to the core and segment data samples in order to study the effect of pulse shape analysis before and after the application of a single segment requirement. In the former case, only the core pulse shape was used. In the latter case, the core pulse shape was used and, optionally, the segment 14 pulse shape in addition.

The likelihood discriminant and neural network analysis were performed on the segment data samples (a) with information from the core electrode only and (b) with information from the core and the segment 14 electrode.

As an example, Figure 11.19 shows the output distributions for the two segment training data samples DEP and Γ_1 for the likelihood method (left), the library method (middle) and the neural network (right). The segment pulse shapes have not been taken into account for these examples.

The results of the analysis are used to either distinguish between electron-like and photon-like or between single-site and multi-site events. Different values of the cut parameters are chosen depending on the goal. The estimate of the power to distinguish between single-site and multi-site events requires knowledge of the fraction of single-site and multi-site events in the data samples. That information is taken from the Monte Carlo simulation and based on the parameter R_{90}.

11.3.3 Selection of electron-like events and discrimination against photon-like events

The power to distinguish between electron-like and photon-like event samples is estimated. The events in the DEP sample are assumed to give the same output in the analyses as events from neutrinoless double beta-decay. The cut values are chosen to keep 90% of the events in the DEP training samples for the three analysis methods and thus a high detection efficiency. The fraction of events in each test data sample identified as electron-like are summarized in Table 11.7. The uncertainties are estimated from the deviation from 90% of the fraction of events identified as electron-like in the DEP test data samples and found to be about 2%. Note that no deviation is found in case of the library method since the DEP training data sample is used as a reference library.

[2] This behavior was also found in a simple calculation of pulse shapes.

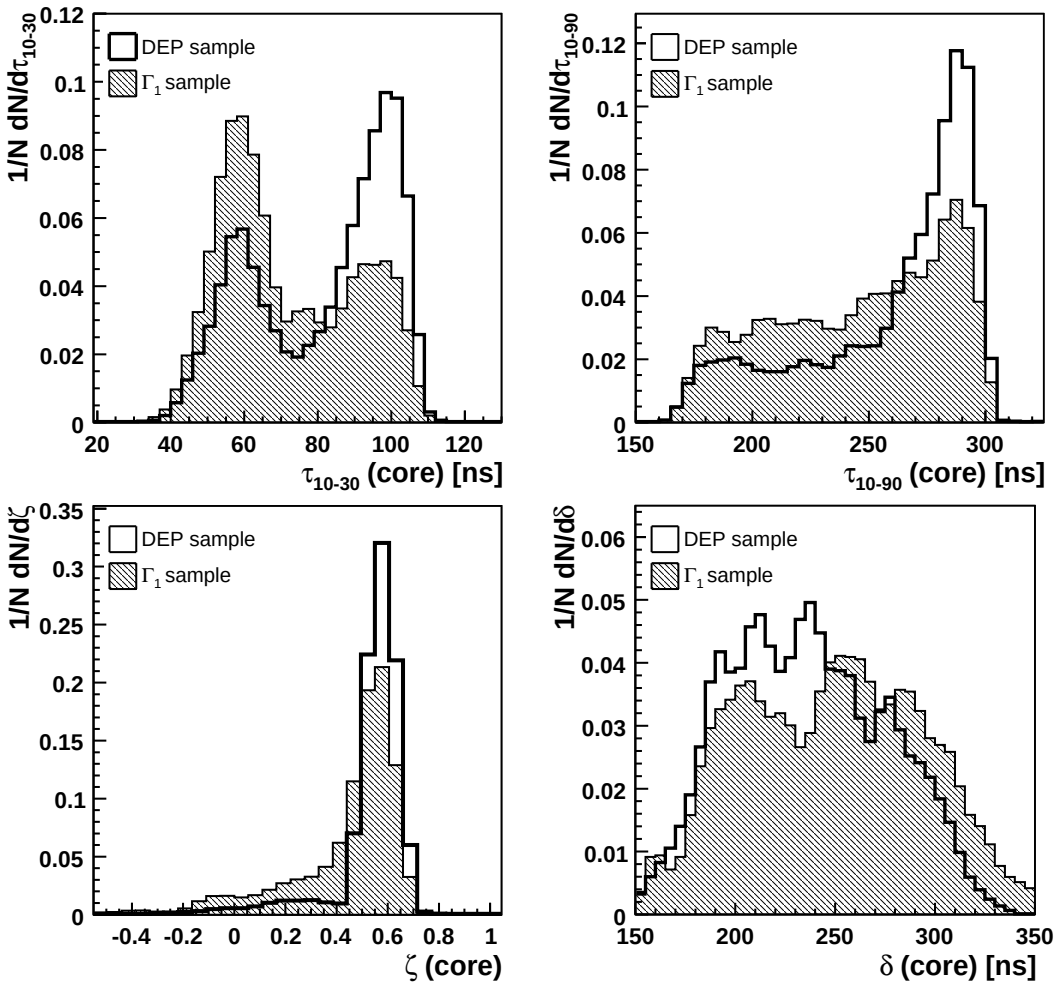

Figure 11.18: Quantities calculated from the core pulse shapes in the *DEP* (open histogram) and Γ_1 (hatched histogram) segment data samples. Top left: risetime τ_{10-30}, top right: risetime τ_{10-90}, bottom left: left-right asymmetry ζ, bottom right: current pulse width δ.

The fraction of events identified as electron-like is significantly lower than 90% in the Γ_1, Γ_2 and *ROI* samples. For each method the fraction in the Γ_1 sample is found to be larger than that in the Γ_2 sample. This is expected, as the range of photons increases with the photon energy.

For all three methods the fraction of events identified as electron-like in the Γ_1 and Γ_2 segment data samples (using the core pulse shape only) is found to be lower than that in the core data samples. The additional usage of the segment pulse shape in the analyses reduces the fraction by maximally 3%; and in case of the neural network the fraction even increases by up to 5%. This demonstrates that the additional information is highly correlated with the existing information and does only marginally contribute to the analysis.

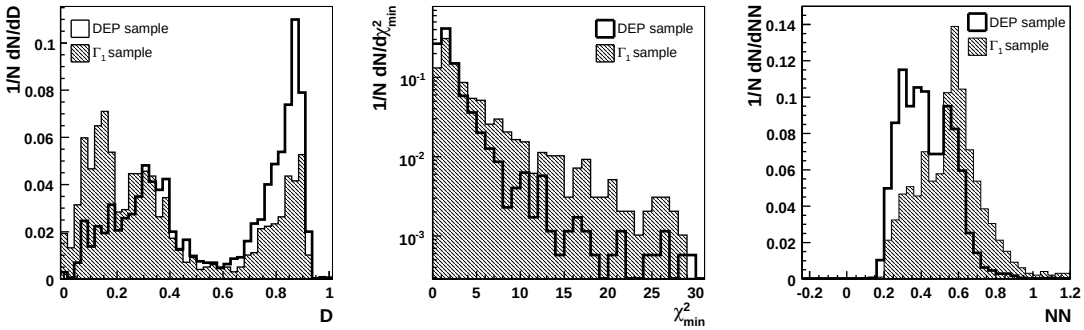

Figure 11.19: Output distributions for the two segment training data samples DEP (open histograms) and Γ_1 (hatched histograms) for the likelihood method (left), the library method (middle) and the neural network (right). The segment pulse shapes have not been taken into account for these examples.

Table 11.7: Fraction of events in the test data samples identified as electron-like for the three analyses. The uncertainties are estimated to be about 2%.

Data samples	DEP (1 593 keV)	Γ_1 (1 620 keV)	Γ_2 (2 615 keV)	ROI (2 039 keV)
Likelihood discriminant method				
Core samples	89.3%	76.5%	75.4%	83.4%
Segm. samples, core only	89.3%	67.1%	64.1%	84.8%
Segm. samples, core and segment	88.0%	66.7%	61.1%	83.4%
Library method				
Core samples	90.0%	86.9%	85.8%	86.7%
Segm. samples, core only	90.0%	68.4%	56.4%	83.1%
Neural network method				
Core samples	90.4%	65.8%	63.2%	79.9%
Segm. samples, core only	89.3%	54.1%	44.3%	80.8%
Segm. samples, core and segment	89.3%	56.1%	49.9%	79.6%

The neural network shows the best performance, although the results should be taken with care as discussed later. This is expected, since the ANN uses the largest fraction of information and also takes correlations between input variables into account.

11.3.4 Selection of single-site events and discrimination against multi-site events

As demonstrated in Table 11.6, neither the DEP nor the Γ_1, Γ_2 and ROI samples are solely composed of single-site or multi-site events. The probability to correctly identify single-site and multi-site events as such, ϵ and η, can be deduced from the fraction of single-site and multi-site events in each sample (estimated from Monte Carlo) and the output of the analyses, D, $\chi^2_{\min}$, NN:

$$\epsilon = \frac{N_{id}^{SSE}/N_{true}^{MSE} - M_{id}^{SSE}/M_{true}^{MSE}}{N_{true}^{SSE}/N_{true}^{MSE} - M_{true}^{SSE}/M_{true}^{MSE}} , \tag{11.5}$$

$$\eta = \frac{N_{id}^{MSE}/N_{true}^{SSE} - M_{id}^{MSE}/M_{true}^{SSE}}{N_{true}^{MSE}/N_{true}^{SSE} - M_{true}^{MSE}/M_{true}^{SSE}} , \tag{11.6}$$

where N_{id}^{SSE} and N_{id}^{MSE} are the number of events in the DEP sample identified as single-site and multi-site events, respectively. The numbers depend on the cut value chosen for each analysis. N_{true}^{SSE} and N_{true}^{MSE} are the true number of single-site and multi-site events in the same sample and are estimated from the Monte Carlo simulation. M_{id}^{SSE} and M_{id}^{MSE} are the number of events in the Γ_1 sample identified as single-site and multi-site events, respectively. M_{true}^{SSE} and M_{true}^{MSE} are the true number of single-site and multi-site events in the same sample. The probabilities are assumed to be the same for all samples. This assumption is reasonable as the energies in the DEP and Γ_1 samples are very close.

The cut values for the three analysis methods are chosen to maximize the figure of merit, the identification efficiency $\sqrt{\epsilon \cdot \eta}$. The probabilities obtained from the data samples using Equations 11.5 and 11.6 are listed in Table 11.8.

The likelihood and library methods work better on events with only one segment hit. The additional usage of the segment pulse shape in the likelihood analysis does not improve these methods.

The analysis of the neural network output yields probabilities larger than one for the segment data samples. The calculation of ϵ and η depends on the real fraction of single-site and multi-site events and is therefore model dependent. The current model assumes the fraction of single-site and multi-site events to be completely reflected in the parameter R_{90}. The validity of the assumed model is limited and the extraction of the probabilities ϵ and η carries systematic uncertainties. For the core data samples the efficiencies do not exceed unity for the chosen cut parameter. Figure 11.20 shows ϵ and η together with the identification efficiency as a function of the neural network cut parameter for the core data samples.

11.3.5 Application to the ^{228}Th data set

Figure 11.21 (left) shows the energy spectrum resulting from a ^{228}Th source in the region from 1.3 MeV to 2.7 MeV as seen by the core electrode. The black line corresponds to all

Table 11.8: Probabilities ϵ and η obtained for all three analysis methods. The errors are due to the fraction of single-site and multi-site events and thus introduced by the choice of $\overline{R}$.

Analysis	ϵ	η	$\sqrt{\epsilon \cdot \eta}$
Likelihood discriminant method			
Core samples	$(74.8^{+1.8}_{-0.3})\%$	$(\ 84.7^{+\ 3.4}_{-\ 2.4})\%$	$(79.6^{+1.4}_{-0.2})\%$
Segm. samples, core only	$(84.3^{+1.8}_{-0.2})\%$	$(\ 97.7^{+10.4}_{-\ 5.9})\%$	$(90.8^{+4.8}_{-1.9})\%$
Segm. samples, core and segment	$(83.9^{+1.7}_{-0.1})\%$	$(\ 94.0^{+\ 9.9}_{-\ 5.6})\%$	$(88.8^{+4.6}_{-1.8})\%$
Library method			
Core samples	$(68.7^{+\ 0.8}_{-\ 0.1})\%$	$(56.1^{+\ 1.4}_{-\ 1.0})\%$	$(62.1^{+0.7}_{-0.2})\%$
Segm. samples, core only	$(90.9^{+\ 0.1}_{-13.4})\%$	$(80.4^{+10.1}_{-\ 9.1})\%$	$(85.6^{+4.8}_{-1.7})\%$
Neural network method			
Core samples	$(85.6^{+2.4}_{-0.4})\%$	$(\ 91.0^{+\ 4.3}_{-\ 0.3})\%$	$(\ 88.3^{+1.9}_{-0.3})\%$
Segm. samples, core only	$(96.4^{+2.5}_{-0.2})\%$	$(121.6^{+15.0}_{-\ 8.5})\%$	$(108.3^{+6.6}_{-2.5})\%$
Segm. samples, core and segment	$(90.6^{+2.3}_{-0.2})\%$	$(115.4^{+13.4}_{-\ 7.7})\%$	$(102.3^{+5.9}_{-2.2})\%$

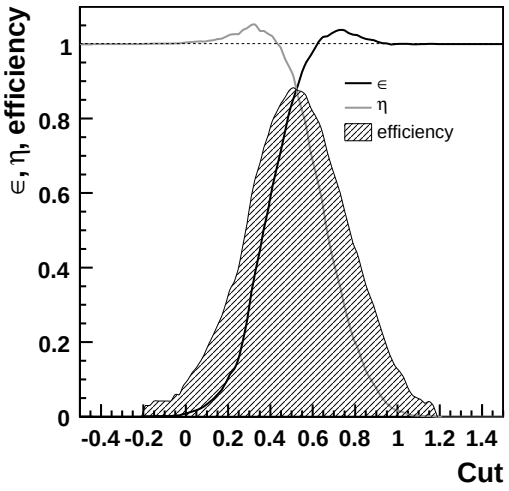

Figure 11.20: Probabilities to correctly identify single-site, ϵ, and multi-site events, η, and the efficiency, $\sqrt{\epsilon \cdot \eta}$, for the neural network analysis of the core data samples. Probabilities above one are caused by uncertainties in the extraction process.

events with only segment S hit, the gray line represents events with only segment S hit and pulse shape analysis, using the ANN, applied. Only the pulse shape of the core was used and the cut parameter was chosen to keep 90% of the events in the DEP training data sample.

The gray spectrum is suppressed with respect to the black spectrum. The suppression ranges up to a factor of about two at the photon peaks. The suppression is weak in the double escape peak. Figure 11.21 (right) shows a close-up of the spectrum in the region

from 1 560 keV to 1 650 keV. The application of the pulse shape analysis removes photon induced events (1 620 keV photon line from the decay of ^{212}Bi) but keeps most of the electron induced events (double escape peak of the 2 615 keV ^{208}Tl photon at 1 593 keV). Pulse shape analysis is thus suitable to confirm the signal process.

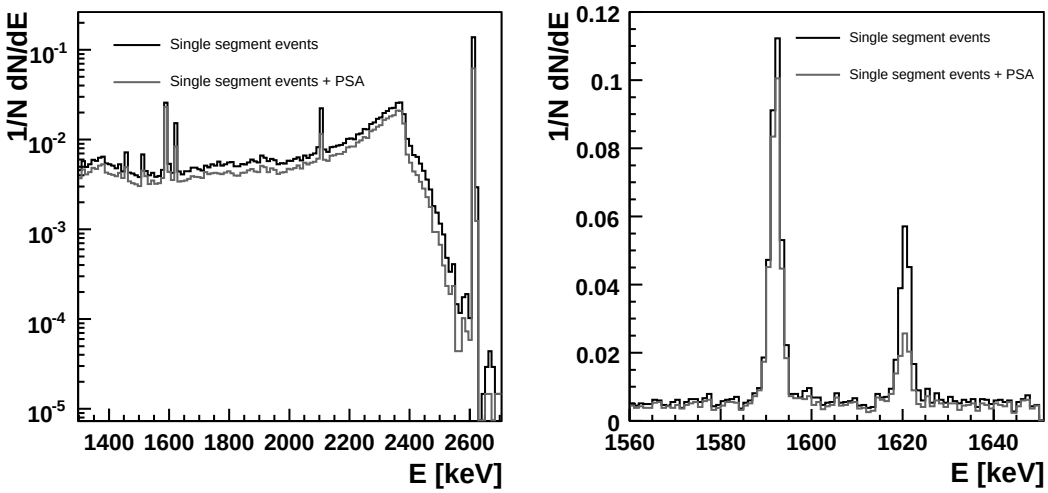

Figure 11.21: Spectrum from a ^{228}Th source as seen by the core electrode. The black line corresponds to all events with only segment S hit, the gray line represents events with only segment S hit and pulse shape analysis, using the ANN, applied. Only the pulse shape of the core was used and the cut parameter was chosen to keep 90% of the DEP events. Left: Spectrum from 1.3 MeV to 2.7 MeV. Right: Close-up of the region from 1 560 keV to 1 650 keV. For a discussion see text.

Chapter 12

Background estimate for the GERDA experiment

The expected background index of the GERDA experiment is estimated. The estimate is based on the simulation of the idealized Phase II setup as described in Section 7.1.1 and an anti-coincidence analysis as described in Chapter 7. The background contributions from radioactive sources are calculated based on the nominal masses and material compositions of the detector surroundings, and on material screening results. The muon induced background is taken from [98].

12.1 Materials and masses

The choice of materials for GERDA is not yet final and material screening results are still pending (see Chapter 3). Table 12.1 summarizes the simulated parts, the foreseen material and the corresponding masses. Table 12.2 lists the assumed activities for each material. The activities are either measured or estimated.

Table 12.1: Table of materials and masses simulated in the setup.

Part	Materials used [g]	
Crystal	Germanium	2107 (per detector)
Holder	Copper	31 (per holder)
	Teflon	7 (per holder)
Cable	Copper	1.3 (per cable)
	Kapton	0.8 (per cable)
Support wire	Copper	10 (per support string)
Electronics	Misc	10 (total)

Table 12.2: Table of contaminations. [a] The amount of ^{68}Ge depends on the storage above ground and the production rate. As not all information necessary is available 100 atoms/kg are assumed at the start of data taking. About 60 decays/kg are expected in the first year, about 25 decays/kg are expected in the second year. [b] The amount of ^{60}Co depends on the storage above ground and the production rate. As not all information necessary is available 40 atoms/kg are assumed at the start of data taking. About 5 decays/kg are expected in the first and second year. [c] The calculation corresponds to an estimate of 20 decays per surface and year. For this geometry the activity is 0.30 μBq/kg. [d] The calculation corresponds to an estimate of 4 decays per surface and year. For this geometry the activity is 0.06 μBq/kg.

Material	Contamination	
Copper (LENS)	≤ 16 μBq/kg	^{226}Ra (U) [120]
	≤ 19 μBq/kg	^{228}Th (Th) [120]
	≤ 88 μBq/kg	^{40}K [120]
	≤ 10 μBq/kg	^{60}Co [120]
Teflon	≤ 160 μBq/kg	^{226}Ra (U) [120]
	≤ 160 μBq/kg	^{228}Th (Th) [120]
	1500 ± 240 μBq/kg	^{40}K [120]
	≤ 70 μBq/kg	^{137}Cs [120]
Kapton	1 mBq/kg	^{226}Ra (U)
	1 mBq/kg	^{228}Th (Th)
	1 mBq/kg	^{60}Co
Liquid N_2	≤ 1 μBq/kg	^{238}U [3]
	≤ 0.3 μBq/kg	^{232}Th [3]
	≤ 200 μBq/m^3	^{222}Ra [3]
Enr. Germanium	≤ 0.1 μBq/kg	^{226}Ra (U)
	≤ 0.1 μBq/kg	^{228}Th (Th)
	100 atoms/kg[a]	^{68}Ge [100]
	40 atoms/kg[b]	^{60}Co [100]
Detector surface	0.63 μBq/surface[c]	^{210}Pb (U) [3]
	0.13 μBq/surface[d]	^{232}Th [3]
Misc	10 mBq/kg	^{226}Ra (U)
	10 mBq/kg	^{228}Th (Th)
	10 mBq/kg	^{60}Co

12.2 Expected background index for Phase II of the GERDA experiment

A segment-cut based analysis of the Monte Carlo data is performed. Events are required to have a measured energy above a threshold of 10 keV in one segment only. The measured energy is required to be ±5 keV around the $Q_{\beta\beta}$-value. The simulation is performed for each source and part listed in Tables 12.1 and 12.2.

The individual background contributions are calculated as

$$b = \frac{p_{\text{survival}}}{\Delta E} \cdot A \cdot \frac{m_{\text{mat.}}}{m_{\text{Ge}}} \ , \tag{12.1}$$

where p_{survival} is the survival probability for the isotope and part, A is the activity per kg material and $m_{\text{mat.}}$ and m_{Ge} are the masses of the material under study and the total amount of germanium. ΔE is 10 keV. The survival probability is the fraction of simulated events which fulfill the event selection criteria.

Table 12.3 summarizes the background contribution for each component. The numbers for the cryogenic liquid and the infrastructure are taken from [121], the numbers for the muon and neutron background are taken from [98]. The background is expected to be dominated by the decay of ^{68}Ge atoms in the first year. The cabling and holder structure will be the most dominant contribution in the second year. These simulations triggered a re-design of the detector suspension which will result in an additional reduction of material and the choice of material (such as electroformed copper which is investigated by the MAJORANA collaboration). The total background level of $3.7 \cdot 10^{-3}$ counts/(kg·keV·y) will be further reduced.

Further studies with an improved modeling of the geometry (including liquid argon as cooling medium) are currently being worked on. The shielding of external photons improves in liquid argon but additional muon and neutron background components have to be taken into account. The analysis of pulse shapes has not yet been taken into account and is expected to further reduce the background. The detailed effect of pulse shape analysis will require an improved Monte Carlo.

For a background level of $3.7 \cdot 10^{-3}$ counts/(kg·keV·y) and an exposure of 100 kg·years the sensitivity calculation presented in Chapter 4 yields a 90% probability lower limit on the half-life of about 10^{26} y. The half-life for which a discovery would be claimed with a probability of 50% is about $3.2 \cdot 10^{25}$ y.

Table 12.3: Background contribution for each component of GERDA calculated using the Monte Carlo simulation tool MaGe and the setup described in Section 7.1.1. The contribution for ^{68}Ge and ^{60}Co are those for the first (second) year.

Part		Background contribution b 10^{-4} counts/(kg·keV·y)
Detector	^{68}Ge	10.8 (4.3)
	^{60}Co	0.3 (0.3)
	Bulk	3.0
	Surface	3.5
Holder	Copper	1.4
	Teflon	2.0
Cabling		7.6
Electronics		3.5
Cryoliquid		0.1
Infrastructure		2.9
Muons and neutrons		2.0
Total		37.1 (30.6)

Chapter 13

Conclusions and outlook

Various methods to distinguish between electron and photon induced events with segmented germanium detectors were evaluated. Detectors of this type will be used in the second phase of the GERDA experiment, which is currently under construction. The goal of GERDA is to search for neutrinoless double beta-decay of ^{76}Ge. An overall estimate of the background expected in GERDA Phase II was given. The sensitivity of the GERDA experiment was evaluated for different background scenarios. The key feature, the operation of bare germanium detectors in a cryogenic liquid, was proven to be feasible.

The power of the methods developed to identify photon induced events was studied with Monte Carlo and with data. The array of segmented detectors described in Section 7.1.1 was the basis for the Monte Carlo study. The first Phase II prototype detector provided the data.

In the Monte Carlo study the background rejection based on anti-coincidence requirements for segmented and unsegmented germanium detectors was compared. The power to distinguish between events with electrons and photons in the final state is significantly improved if segment anti-coincidences are used. The improvement for the particularly interesting case of ^{60}Co inside the crystals is about one order of magnitude.

The first 18-fold segmented n-type prototype detector was operated in a conventional cryostat. The detector was characterized with respect to its operational parameters (depletion voltage, resolution), the segmentation (surface scans) and the crystal properties (crystal axes positions). Special data were taken to evaluate the power to distinguish between electron and photon induced events based on (1) anti-coincidence requirements between segments and on (2) the analysis of the time structure of the detector response. A Monte Carlo simulation of the test setup complemented the measurements.

It was shown that the identification of events with multiply scattered photons in the final state using segmented detectors is feasible. The power to reject events in which the full photon energy is deposited inside the detector is energy dependent. The suppression

in the spectrum increases from 1.01 ± 0.002 at 122 keV to 3.04 ± 0.02 at 2 615 keV in the experimental setup described. The suppression of Compton scattered events in the $Q_{\beta\beta}$-region of ^{76}Ge (2 039 keV) coming from ^{60}Co and ^{228}Th sources was measured to be 14.2 ± 2.1 and 1.68 ± 0.02, respectively.

The power to reject photon induced events was shown to improve with increasing number of segments and to be stable against threshold variations and the background normalization. A data to Monte Carlo comparison, considering background from radioactive isotopes in the laboratory, showed a good agreement with deviations of the order of 5-10%. This shows that simulations based on the MaGe tool are suitable and can reliably predict background levels.

Three pulse shape analysis techniques were developed and applied to data. The analyses targeted the separation of electron-like and photon-like event samples and, based on Monte Carlo modeling, the separation of single-site and multi-site events. All three methods were trained with double escape events. These events are expected to be similar to $0\nu\beta\beta$-events as in both processes the energy deposition in the detectors is due to the charged leptons in the final state. This was confirmed by Monte Carlo.

Two signals, i.e., from the core and the segment electrode, are provided in single-segment events. Two methods were tested for the case that the pulse shapes from the segment electrode were either taken into account or not. It was shown that the power to identify photon events does not increase with the straightforward usage of additional information from the pulse shape of the segment.

The performance of the three methods is slightly worse than what is reported in [115]. A reason for this is the purity of the samples. Also, the spatial distribution of energy deposited inside the detector is not homogeneous in the DEP sample. Methods to select cleaner and more homogeneous training samples are currently being tested. The artificial neural network performed better than the likelihood discriminant and the library method. Photon peaks remaining after a single segment cut and pulse shape analysis are suppressed by a factor of about two around 1.6 MeV. At the same time 90% of the events in the single-site dominated sample are kept. This demonstrates that the association of a particular peak with the signal process can be substantiated by such an analysis.

Methods to distinguish between electron and photon induced events using pulse shape analysis are still being developed. Methods which make use of the mirror charges in segmented detectors could not only lead to further rejection of photon induced events but could also regain signal efficiency. Feasibility studies are currently carried out.

A simulation of the development of pulse shapes will improve the reliability of the interpretation of the pulse shape analyses. Studies aiming at the identification of neutron induced events are currently being pursued and show promise. The identification of α-particles seems also possible. Events which deposit energy close to the surface will have to be investigated to quantify this.

The segmented prototype detector worked reliably and within specifications over a period of several months. The next step will be to operate it in a cryogenic test facility currently under construction. Several other, also long-term, measurements with n-type and p-type detectors are currently being performed or planned.

The studies presented here allow the conclusions that (1) energy and pulse shape information from segmented detectors can be used to significantly reduce the background in double beta-decay experiments such as GERDA, and that (2) the Monte Carlo tools used are reliable with respect to their predictive power. Monte Carlo simulations of the GERDA experiment together with the results of screening measurements show that a background index of the order of 10^{-3} counts/(kg·keV·y) is feasible for the Phase II of the experiment.

A spectral analysis method, based on Bayes' Theorem, was developed to evaluate the probability that a spectrum can be explained by background processes alone, and thereby determine whether a signal process is present. A criterion for claiming evidence for, or discovery of, a signal was proposed. Monte Carlo techniques were described to make predictions about the possible outcomes of the experiments and to evaluate the sensitivity for the process under study. As an example the method was applied to the case of the GERDA experiment for which the sensitivity to neutrinoless double beta-decay of ^{76}Ge was calculated. With a background index of 10^{-3} counts/(kg·keV·y) and an exposure of 100 kg·years a lower limit on the half-life of the $0\nu\beta\beta$-process of $13.5 \cdot 10^{25}$ years is expected to be set if no $0\nu\beta\beta$-events are observed.

Acknowledgement

Many people have helped me writing this thesis and I am grateful for their support.

First of all I would like to thank Prof. Allen Caldwell for the opportunity to let me work in his group and for his support during this time. I would like to thank Dr. Iris Abt for her support, her patience and all the red pens. Also, I would like to thank the whole working group (Allen, Bela, Dan, Daniel and Maike, Dano and Monika, Iris, Jens, Jing, Manuela and Xiang), in particular Xiang Liu and Daniel Kollar - my postdocs who taught me how to brew real coffee. Thank you all for the support and the great help.

I would also like to thank my parents, my brother Dennis, and Katrin for their love and support. I am grateful for all the motivation and strength they gave me during the time of writing.

Bibliography

[1] C. E. Aalseth *et al.* [IGEX Collaboration], "The IGEX Ge-76 neutrinoless double-beta decay experiment: Prospects for next generation experiments," Phys. Rev. D **65** (2002) 092007 [arXiv:hep-ex/0202026].

[2] H. V. Klapdor-Kleingrothaus, I. V. Krivosheina, A. Dietz and O. Chkvorets, "Search for neutrinoless double beta decay with enriched Ge-76 in Gran Sasso 1990-2003," Phys. Lett. B **586** (2004) 198 [arXiv:hep-ph/0404088].

[3] S. Schönert *et al.* [GERDA Collaboration], "The GERmanium Detector Array (GERDA) for the search of neutrinoless beta beta decays of Ge-76 at LNGS," Nucl. Phys. Proc. Suppl. **145** (2005) 242.

[4] F. Reines, "The neutrino: From poltergeist to particle," Rev. Mod. Phys. **68** (1996) 317.

[5] S. L. Glashow, "Partial Symmetries Of Weak Interactions," Nucl. Phys. **22** (1961) 579.

[6] S. Weinberg, "A Model Of Leptons," Phys. Rev. Lett. **19** (1967) 1264.

[7] A. Salam, "Weak and electromagnetic interactions," Proc. of the 8th Nobel Symposium on "Elementary particle theory, relativistic groups and analyticity," Almquist and Wiksells, Stockholm, (1969) 367.

[8] C. S. Wu, E. Ambler, R. W. Hayward, D. D. Hoppes and R. P. Hudson, "Experimental Test Of Parity Conservation In Beta Decay," Phys. Rev. **105** (1957) 1413.

[9] G. Arnison *et al.* [UA1 Collaboration], "Recent Results On Intermediate Vector Boson Properties At The Cern Super Proton Synchrotron Collider," Phys. Lett. B **166** (1986) 484.

[10] R. Ansari *et al.* [UA2 Collaboration], "Measurement Of The Standard Model Parameters From A Study Of W And Z Bosons," Phys. Lett. B **186** (1987) 440.

[11] [ALEPH, DELPHI, L3, OPAL and SLD Collaborations], "Precision electroweak measurements on the Z resonance," Phys. Rept. **427** (2006) 257 [arXiv:hep-ex/0509008].

[12] W. M. Yao *et al.* [Particle Data Group], "Review of particle physics," J. Phys. G **33** (2006) 1.

[13] R. Davis, "Solar neutrinos. II: Experimental," Phys. Rev. Lett. **12** (1964) 303.

[14] B. Kayser, "Neutrino Mass, Mixing, and Flavor Change," `http://www.slac.stanford.edu/spires/find/hep/www?irn=5993725`.

[15] L. Wolfenstein, "Neutrino oscillations in matter," Phys. Rev. D **17** (1978) 2369.

[16] S. P. Mikheev and A. Y. Smirnov, "Neutrino oscillations in a variable-density medium and nu bursts due to the gravitational collapse of stars," Sov. Phys. JETP **64** (1986) 4 [Zh. Eksp. Teor. Fiz. **91** (1986) 7].

[17] J. N. Bahcall, S. Basu and A. M. Serenelli, "What Is The Neon Abundance Of The Sun?," Astrophys. J. **631** (2005) 1281 [arXiv:astro-ph/0502563].

[18] R. J. Davis, D. S. Harmer and K. C. Hoffman, "Search for neutrinos from the sun," Phys. Rev. Lett. **20** (1968) 1205.

[19] B. T. Cleveland *et al.*, "Measurement of the solar electron neutrino flux with the Homestake chlorine detector," Astrophys. J. **496** (1998) 505.

[20] P. Anselmann *et al.* [GALLEX Collaboration], "Solar neutrinos observed by GALLEX at Gran Sasso," Phys. Lett. B **285** (1992) 376.

[21] M. Altmann *et al.* [GNO Collaboration], "GNO solar neutrino observations: Results for GNO I," Phys. Lett. B **490** (2000) 16 [arXiv:hep-ex/0006034].

[22] J. N. Abdurashitov *et al.* [SAGE Collaboration], "Measurement of the solar neutrino capture rate by SAGE and implications for neutrino oscillations in vacuum," Phys. Rev. Lett. **83** (1999) 4686 [arXiv:astro-ph/9907131].

[23] W. Hampel *et al.* [GALLEX Collaboration], "GALLEX solar neutrino observations: Results for GALLEX IV," Phys. Lett. B **447** (1999) 127.

[24] M. Altmann *et al.* [GNO Collaboration], "Complete results for five years of GNO solar neutrino observations," Phys. Lett. B **616** (2005) 174 [arXiv:hep-ex/0504037].

[25] J. N. Abdurashitov *et al.* [SAGE Collaboration], "Measurement of the solar neutrino capture rate by the Russian-American gallium solar neutrino experiment during one half of the 22-year cycle of solar activity," J. Exp. Theor. Phys. **95** (2002) 181 [Zh. Eksp. Teor. Fiz. **122** (2002) 211] [arXiv:astro-ph/0204245].

[26] H. Ikeda *et al.*, "Kamiokande: The Kamioka Nucleon Decay Experiment," UTLICEPP-82-04.

[27] K. S. Hirata *et al.* [Kamiokande-II Collaboration], "Observation of B-8 solar neutrinos in the Kamiokande-II detector," Phys. Rev. Lett. **63** (1989) 16.

[28] Y. Fukuda *et al.* [Kamiokande Collaboration], "Solar neutrino data covering solar cycle 22," Phys. Rev. Lett. **77** (1996) 1683.

[29] J. Hosaka *et al.* [Super-Kamkiokande Collaboration], "Solar neutrino measurements in Super-Kamiokande-I," Phys. Rev. D **73** (2006) 112001 [arXiv:hep-ex/0508053].

[30] Q. R. Ahmad *et al.* [SNO Collaboration], "Direct evidence for neutrino flavor transformation from neutral-current interactions in the Sudbury Neutrino Observatory," Phys. Rev. Lett. **89** (2002) 011301 [arXiv:nucl-ex/0204008].

[31] B. Aharmim *et al.* [SNO Collaboration], "Electron energy spectra, fluxes, and day-night asymmetries of B-8 solar neutrinos from the 391-day salt phase SNO data set," Phys. Rev. C **72** (2005) 055502 [arXiv:nucl-ex/0502021].

[32] T. Araki *et al.* [KamLAND Collaboration], "Measurement of neutrino oscillation with KamLAND: Evidence of spectral distortion," Phys. Rev. Lett. **94** (2005) 081801 [arXiv:hep-ex/0406035].

[33] Y. Ashie *et al.* [Super-Kamiokande Collaboration], "A measurement of atmospheric neutrino oscillation parameters by Super-Kamiokande I," Phys. Rev. D **71** (2005) 112005 [arXiv:hep-ex/0501064].

[34] M. Apollonio *et al.*, "Search for neutrino oscillations on a long base-line at the CHOOZ nuclear power station," Eur. Phys. J. C **27** (2003) 331 [arXiv:hep-ex/0301017].

[35] Y. Ashie *et al.* [Super-Kamiokande Collaboration], "Evidence for an oscillatory signature in atmospheric neutrino oscillation," Phys. Rev. Lett. **93** (2004) 101801 [arXiv:hep-ex/0404034].

[36] R. N. Mohapatra and G. Senjanovic, "Neutrino mass and spontaneous parity nonconservation," Phys. Rev. Lett. **44** (1980) 912.

[37] R. N. Mohapatra and G. Senjanovic, "Neutrino Masses And Mixings In Gauge Models With Spontaneous Parity Violation," Phys. Rev. D **23** (1981) 165.

[38] S. Hannestad, "Neutrinos in cosmology," New J. Phys. **6** (2004) 108 [arXiv:hep-ph/0404239].

[39] C. Weinheimer *et al.*, "High precision measurement of the tritium beta spectrum near its endpoint and upper limit on the neutrino mass," Phys. Lett. B **460** (1999) 219.

[40] V. M. Lobashev *et al.*, "Direct search for mass of neutrino and anomaly in the tritium beta-spectrum," Phys. Lett. B **460** (1999) 227.

[41] C. Kraus *et al.*, "Final results from phase II of the Mainz neutrino mass search in tritium beta decay," Eur. Phys. J. C **40** (2005) 447 [arXiv:hep-ex/0412056].

[42] A. Osipowicz *et al.* [KATRIN Collaboration], "KATRIN: A next generation tritium beta decay experiment with sub-eV sensitivity for the electron neutrino mass," arXiv:hep-ex/0109033.

[43] K. Assamagan *et al.*, "Upper limit of the muon-neutrino mass and charged pion mass from momentum analysis of a surface muon beam," Phys. Rev. D **53** (1996) 6065.

[44] NuMass collaboration, `http://www.hep.umn.edu/numass` .

[45] R. Barate *et al.* [ALEPH Collaboration], "An upper limit on the tau neutrino mass from three- and five-prong tau decays," Eur. Phys. J. C **2** (1998) 395.

[46] M. Goeppert-Mayer, "Double beta-disintegration," Phys. Rev. **48** (1935) 512.

[47] G. Racah, "On the symmetry of particle and antiparticle," Nuovo Cim. **14** (1937) 322.

[48] W. H. Furry, "On transition probabilities in double beta-disintegration," Phys. Rev. **56** (1939) 1184.

[49] R. N. Mohapatra, "New contributions to neutrinoless double-beta decay in supersymmetric theories," Phys. Rev. D **34** (1986) 3457.

[50] M. Hirsch, H. V. Klapdor-Kleingrothaus and S. G. Kovalenko, "New Supersymmetric Contributions To Neutrinoless Double Beta Decay," Phys. Lett. B **352** (1995) 1 [arXiv:hep-ph/9502315].

[51] J. Schechter and J. W. F. Valle, "Neutrinoless double-beta decay in SU(2) x U(1) theories," Phys. Rev. D **25** (1982) 2951.

[52] R. B. Firestone, "Table of Isotopes", 8th edition, 1999, John Wiley & Sons, Inc., ISBN 0-471-14918-7.

[53] A. Merle and W. Rodejohann, "The elements of the neutrino mass matrix: Allowed ranges and implications of texture zeros," Phys. Rev. D **73** (2006) 073012 [arXiv:hep-ph/0603111].

[54] T. Schwetz, "Global fits to neutrino oscillation data," Phys. Scripta **T127** (2006) 1 [arXiv:hep-ph/0606060].

[55] W. C. Haxton and G. J. Stephenson, "Double Beta Decay," Prog. Part. Nucl. Phys. **12** (1984) 409.

[56] E. Caurier, F. Nowacki, A. Poves and J. Retamosa, "Shell Model Study of the Double Beta Decays of 76Ge, 82Se and 136Xe," arXiv:nucl-th/9601017.

[57] V. Rodin, A. Faessler, F. Simkovic and P. Vogel, "Uncertainties in the 0nu beta beta decay nuclear matrix elements," Czech. J. Phys. **56** (2006) 495 [arXiv:nucl-th/0602004].

[58] J. Suhonen and O. Civitarese, "Weak-interaction and nuclear-structure aspects of nuclear double beta decay," Phys. Rept. **300** (1998) 123.

[59] A. S. Barabash, "Average and recommended half-life values for two neutrino double beta decay: Upgrade'05," Czech. J. Phys. **56** (2006) 437 [arXiv:nucl-ex/0602009].

[60] H. V. Klapdor-Kleingrothaus *et al.*, "Latest results from the Heidelberg-Moscow double-beta-decay experiment," Eur. Phys. J. A **12** (2001) 147 [arXiv:hep-ph/0103062].

[61] R. Arnold *et al.* [NEMO Collaboration], "First results of the search of neutrinoless double beta decay with the NEMO 3 detector," Phys. Rev. Lett. **95** (2005) 182302 [arXiv:hep-ex/0507083].

[62] F. A. Danevich *et al.*, "Search for 2 beta decay of cadmium and tungsten isotopes: Final results of the Solotvina experiment," Phys. Rev. C **68** (2003) 035501.

[63] C. Arnaboldi *et al.*, "A new limit on the neutrinoless beta beta decay of Te-130," Phys. Rev. Lett. **95** (2005) 142501 [arXiv:hep-ex/0501034].

[64] G. Douysset, T. Fritioff, C. Carlberg, I. Bergstrom and M. Bjorkhage, "Determination of the Ge-76 double beta decay Q value," Phys. Rev. Lett. **86** (2001) 4259.

[65] C. E. Aalseth *et al.* [Majorana Collaboration], "The Majorana neutrinoless double-beta decay experiment," Phys. Atom. Nucl. **67** (2004) 2002 [Yad. Fiz. **67** (2004) 2025] [arXiv:hep-ex/0405008].

[66] R. Gaitskell *et al.* [Majorana Collaboration], "White paper on the Majorana zero-neutrino double-beta decay experiment," arXiv:nucl-ex/0311013.

[67] G. Heusser, "Low-Radioactivity Background Techniques," Ann. Rev. Nucl. Part. Sci. **45** (1995) 543.

[68] I. Abt *et al.* [GERDA Collaboration], "Background reduction in neutrinoless double beta decay experiments using segmented detectors - a Monte Carlo study for the GERDA setup," Nucl. Instr. and Meth. A **570/3** (2007) 479.

[69] I. Abt *et al.* [GERDA Collaboration], "Identification of photons in double beta-decay experiments using segmented germanium detectors - studies with a GERDA Phase II prototype detector," arXiv:nucl-ex/0701005.

[70] P. Peiffer *et al.*, "Operation of bare HP-Germanium detectors in liquid argon (LAr)," Nucl. Phys. B Proc. Supp. **143** (2005) 511.

[71] M. Di Marco, P. Peiffer and S. Schonert, "LArGe: Background suppression using liquid argon (LAr) scintillation for 0nu beta beta decay search with enriched germanium (Ge) detectors," arXiv:physics/0701001.

[72] J. L. Orrell, C. E. Aalseth, J. F. Amsbaugh, P. J. Doe and T. W. Hossbach, "Operation of a high purity germanium crystal in liquid argon as a Compton suppressed radiation spectrometer," arXiv:nucl-ex/0610018.

[73] I. Abt *et al.* [GERDA Collaboration], "Technical Proposal," http://www.mpi-hd.mpg.de/ge76/publications.html .

[74] E. Meroni *et al.* [Borexino Collaboration], "The Borexino Project To Study The Solar Neutrinos," http://www.slac.stanford.edu/spires/find/hep/www?irn=3843939 . Given at 11th Moriond Workshop: Tests of Fundamental Laws in Physics, Les Arcs, France, 26 Jan - 2 Feb 1991.

[75] C. Cattadori *et al.*, "The GERmanium Detector Array read-out: Status and developments," accepted by Nucl. Instrum. Meth. A, http://dx.doi.org/10.1016/j.nima.2006.10.226 .

[76] I. Abt *et al.* [GERDA Collaboration], "Progress Report to the LNGS Scientific Commitee," http://www.mpi-hd.mpg.de/ge76/publications.html .

[77] http://www.irmm.jrc.be/html/about_IRMM/laboratories/underground_laboratory_HADES.htm .

[78] A. Caldwell and K. Kröninger, "Signal discovery in sparse spectra: A Bayesian analysis," Phys. Rev. D **74** (2006) 092003 [arXiv:physics/0608249].

[79] For an introduction to Bayesian analysis techniques, see e.g., "Bayesian Reasoning in Data Analysis", G. D'Agostini, World Scientific Publishing Company, 2003;
"Data Analysis. A Bayesian Tutorial," D. S. Sivia, Oxford University Press, USA, 2006;
"Probability Theory - The Logic of Science," E. T. Jaynes, Cambridge University Press, 2003;
"From Laplace to Supernova SN 1987A: Bayesian Inference in Astrophysics," T. Loredo, in "Maximum-Entropy and Bayesian Methods," Kluwer Academic Publishers, Netherlands, 1990.

[80] T. J. Loredo and D. Q. Lamb, "Bayesian analysis of neutrinos observed from supernova SN 1987A," Phys. Rev. D **65** (2002) 063002 [arXiv:astro-ph/0107260].

[81] V. A. Rodin, A. Faessler, F. Simkovic and P. Vogel, "Assessment of uncertainties in QRPA 0nu beta beta-decay nuclear matrix elements," Nucl. Phys. A **766** (2006) 107.

[82] "Radiation Detection and Measurements," G. F. Knoll, 3rd edition, John Wiley&Sons, Inc., 2000.

[83] U. Amaldi, "Fluctuations In Calorimetry Measurements," Phys. Scripta **23** (1981) 409.

[84] H. Bethe, "Theory of the passage of fast corpuscular rays through matter," Annalen Phys. **5** (1930) 325.

[85] F. Bloch, " Bremsvermögen von Atomen mit mehreren Elektronen," Z. Phys. **81** (1933) 363.

[86] "Teilchendetektoren", C. Grupen, B.I. Wissenschaftsverlag, 1993

[87] T. Mukoyama, "Range Of Electrons And Positrons," Nucl. Instrum. Meth. **134** (1976) 125.

[88] H. G. Reik and H. Risken, "Distribution functions for hot electrons in may-valley semiconductors," Phys. Rev. **124** (1961) 3.

[89] H. G. Reik and H. Risken, "Drift velocity and anisotropy of hot electrons in n germanium," Phys. Rev. **126** (1962) 5.

[90] M. I. Nathan, "Anisotropy of the conductivity of n-type germanium at high electric fields," Phys. Rev. **130** (1963) 6.

[91] C. Jacoboni *et al.*, "Electron drift velocity and diffusivity in germanium," Phys. Rev. B **24** (1981) 2.

[92] W. Sasaki and M. Shibuya, "Experimental Evidence of the Anisotropy of Hot Electrons in n-type Germanium," J. Phys. Soc. Japan **11** (1956) 1202.

[93] L. Mihailescu, W. Gast, R. M. Lieder, H. Brands and H. Jager, "The influence of anisotropic electron drift velocity on the signal shapes of closed-end HPGe detectors," Nucl. Instrum. Meth. A **447** (2000) 350.

[94] B. Bruyneel, "Characterization of Segmented Large Volume, High Purity Germanium Detectors," Dissertation, University of Cologne.

[95] Z. He, "Review of the Shockley-Ramo theorem and its application in semiconductor gamma-ray detectors," Nucl. Instrum. Meth. A **463** (200) 250.

[96] K. Kröninger, "Towards pulse shape analysis for the GERDA experiment," Prog. Part. Nucl. Phys. **57** (2006) 263.

[97] K. Vetter *et al.*, "Performance of the GRETA prototype detectors," Nucl. Instrum. Meth. A **452** (2000) 105.

[98] L. Pandola *et al.* [GERDA Collaboration], "Monte Carlo evaluation of the muon-induced background in the GERDA double beta decay experiment," Nucl. Instrum. Meth. A **570/1** (2007) 149 [LNGS-EXP/04-06].

[99] F. T. Avignone *et al.*, "Theoretical and experimental investigation of cosmogenic radioisotope production in germanium," Nucl. Phys. Proc. Suppl. **28A** (1992) 280.

[100] M. Altmann *et al.*, "Production of ^{68}Ge and ^{60}Co for Phase II Detectors," GERDA internal note GSTR-05-024.

[101] A. M. Bakalyarov, A. Y. Balysh, S. T. Belyaev, V. I. Lebedev and S. V. Zhukov [C03-06-23.1 Collaboration], "Results of the experiment on investigation of Germanium-76 double beta decay," Phys. Part. Nucl. Lett. **2** (2005) 77 [Pisma Fiz. Elem. Chast. Atom. Yadra **2** (2005) 21] [arXiv:hep-ex/0309016].

[102] I. Abt *et al.* [GERDA Collaboration], "Pulse shapes from electron and photon induced events in segmented high-purity germanium detectors," arXiv:0704.3016.

[103] J. Simpson, "The Agata Project," J. Phys. G **31** (2005) S1801.

[104] N. J. Hammond, T. Duguet and C. J. Lister, "Ambiguity of gamma-ray tracking of two-interaction events," Nucl. Instrum. Meth. A **547** (2005) 535 [arXiv:nucl-ex/0407014].

[105] S. Agostinelli *et al.* [GEANT4 Collaboration], "GEANT4: A simulation toolkit," Nucl. Instrum. Meth. A **506** (2003) 250.

[106] M. Bauer, J. Jochum and S. Scholl, "Simulations of muon-induced neutron background with GEANT4,"
`http://www.slac.stanford.edu/spires/find/hep/www?irn=6347657` . Prepared for IDM 2004: 5th International Workshop on the Identification of Dark Matter, Edinburgh, Scotland, United Kingdom, 6-10 Sep 2004.

[107] GEANT4 Physics Reference Manual,
`http://geant4.web.cern.ch/geant4`.

[108] M. Bauer *et al.*, "MaGe: A Monte Carlo framework for the Gerda and Majorana double beta decay experiments," J. Phys. Conf. Ser. **39** (2006) 362.

[109] H. V. Klapdor-Kleingrothaus, I. V. Krivosheina and I. V. Titkova, "Theoretical Investigation Of The Dependence Of Double Beta Decay Tracks In A Ge Detector On Particle And Nuclear Physics Parameters And Separation From Gamma Ray Events," Phys. Rev. D **73** (2006) 013010.

[110] J. Hellmig and H. V. Klapdor-Kleingrothaus, "Identification of single-site events in germanium detectors by digital pulse shape analysis," Nucl. Instrum. Meth. A **455** (2000) 638.

[111] B. Majorovits and H. V. Klapdor-Kleingrothaus, "Digital pulseshape analysis by neural networks for the Heidelberg-Moscow-double-beta decay experiment," Eur. Phys. J. A **6** (1999) 463 [arXiv:hep-ex/9911001].

[112] D. Gonzalez *et al.*, "Pulse shape discrimination in the IGEX experiment," Nucl. Instrum. Meth. A **515** (2003) 634 [arXiv:hep-ex/0302018].

[113] I. Abt *et al.* [GERDA Collaboration], "Test of pulse shape analysis procedures using single Compton scattering," to be published.

[114] C. E. Aalseth, "Germanium spectrometer pulse shape discrimination for germanium 76 double beta decay," UMI-30-06000, `http://www.slac.stanford.edu/spires/find/hep/www?r=umi-30-06000`.

[115] S. R. Elliott, V. M. Gehman, K. Kazkaz, D. M. Mei and A. R. Young, "Pulse shape analysis in segmented detectors as a technique for background reduction in Ge double-beta decay experiments," Nucl. Instrum. Meth. A **558** (2006) 504 [arXiv:nucl-ex/0509026].

[116] C. G. Broyden, Journal of the Institute for Mathematics and Applications, **6** (1970) 222;
R. Fletcher, Computer Journal **13** (1970) 317;
D. Goldfarb, Mathematics of Computation **24** (1970) 23;
D. F. Shanno, Mathematics of Computation **24** (1970) 647;
See also summary in: D. F. Shanno, J. of Optimization Theory and Applications, **46** (1985) 87.

[117] `http://www.canberra.com/products/1129.asp`

[118] I. Abt *et al.* [GERDA Collaboration], "Characterization of the first true-coaxial 18-fold segmented n-type prototype detector for the GERDA project," arXiv:nucl-ex/0701004.

[119] User's manual, Digital Gamma Finder (DGF) PIXIE-4, XRay Instrumentation Associates, Version 1.20, August 2004.

[120] G. Heusser, M. Laubenstein, H. Neder, "Low-Level germanium gamma-ray spectrometry at the μBq/kg level and future developments towards higher sensitivity," Proc. of Intern. Conf. Isotop. Environm. Studies Aquatic Forum 2004, 25 - 29 October 2004, Monte-Carlo, Monaco.

[121] X. Liu and L. Pandola, private communication.